



**EPR AND ENDOR STUDIES OF POINT DEFECTS IN  
LITHIUM TETRABORATE CRYSTALS**

DISSERTATION

Douglas A. Buchanan, Major, USAF

AFIT-ENP-DS-12-D-01

DEPARTMENT OF THE AIR FORCE  
AIR UNIVERSITY

***AIR FORCE INSTITUTE OF TECHNOLOGY***

Wright-Patterson Air Force Base, Ohio

**DISTRIBUTION STATEMENT A.**  
APPROVED FOR PUBLIC RELEASE; DISTRIBUTION UNLIMITED.

The views expressed in this document are those of the author and do not reflect the official policy or position of the United States Air Force, The United States Department of Defense or the United States Government. The company, product, and service names used in this document are for identification purposes only. All trademarks and property of their respective owners. Use of these trademarks does not imply endorsement.

This material is declared a work of the U.S. Government and is not subject to copyright protection of the United States

AFIT-ENP-DS-12-D-01

EPR AND ENDOR STUDIES OF POINT DEFECTS IN  
LITHIUM TETRABORATE CRYSTALS

DISSERTATION

Presented to the Faculty  
Graduate School of Engineering and Management  
Air Force Institute of Technology  
Air University  
Air Education and Training Command  
in Partial Fulfillment of the Requirements for the  
Degree of Doctor of Philosophy

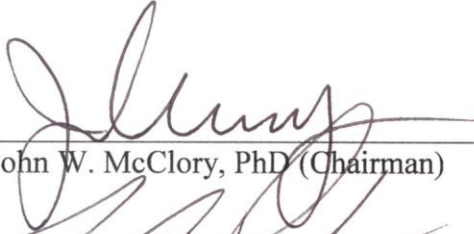
Douglas A. Buchanan, BS, MS  
Major, USAF

**DISTRIBUTION STATEMENT A.**  
APPROVED FOR PUBLIC RELEASE; DISTRIBUTION UNLIMITED.

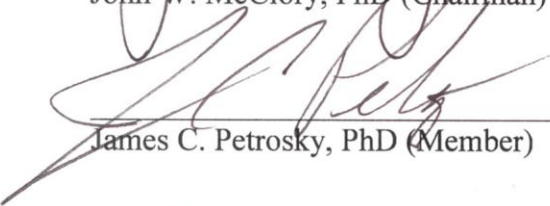
EPR AND ENDOR STUDIES OF POINT DEFECTS IN  
LITHIUM TETRABORATE CRYSTALS

Douglas A. Buchanan, MS  
Major, USAF

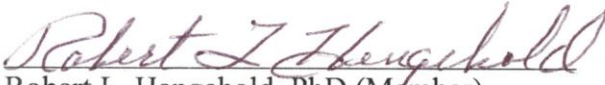
Approved

  
\_\_\_\_\_  
John W. McClory, PhD (Chairman)


15 Nov 12  
Date

  
\_\_\_\_\_  
James C. Petrosky, PhD (Member)

13 Nov 12  
Date

  
\_\_\_\_\_  
Robert L. Hengehold, PhD (Member)

13 Nov 12  
Date


  
\_\_\_\_\_  
Matthew C. Fickus, PhD (Member)

13 Nov 12  
Date

  
\_\_\_\_\_  
Larry E. Halliburton, PhD (Member)

13 Nov 12  
Date

Accepted:

  
\_\_\_\_\_  
M. U. THOMAS  
Dean, Graduate School of Engineering  
and Management

26 Nov 2012  
Date

## **Abstract**

Lithium tetraborate ( $\text{Li}_2\text{B}_4\text{O}_7$  or LTB) is a promising material for both radiation dosimetry and neutron detection applications. LTB crystals can be grown pure or doped with different impurities including transition-metal and rare-earth ions. Research in this dissertation focuses on undoped LTB crystals and LTB crystals doped with copper and silver. Electron paramagnetic resonance (EPR) and electron-nuclear double resonance (ENDOR) are used to characterize point defects in the lithium tetraborate crystals. Thermoluminescence (TL), photoluminescence (PL), photoluminescence excitation (PLE), and optical absorption (OA) are also used. An intrinsic hole trap associated with lithium vacancies is characterized with EPR and ENDOR and its thermal stability is determined using thermoluminescence. A “perturbed” hole trap due to  $\text{Ag}^{2+}$  ions is characterized in doped crystals using EPR data alone. This method is tested on a previously studied hole center where both EPR and ENDOR were used. New x-ray induced centers are identified in copper-doped crystals. These include two  $\text{Cu}^{2+}$  hole centers and two  $\text{Cu}^0$  electron centers. These centers are characterized with EPR and their thermal stability explains TL peaks in glow curves. Finally, a comprehensive study utilizing EPR, OA, PL, and PLE data provide convincing explanations for the absorption and emission features of silver-doped crystals.

*This dissertation is dedicated to my family.*  
*Thank you all for your love and support throughout!*

## **Acknowledgements**

I would like to thank Col. Rex R. Kiziah at the United States Air Force Academy for allowing me the chance to earn my PhD. I also wish to thank Dr John McClory for being my Research Committee Chairman and for being a mentor, educator, and advisor. I could not have succeeded without your assistance most of all. You kept me on track! I'd like to thank my committee members: Dr Hengehold, Dr Petrosky, Dr Fickus, and Dr Halliburton. I thank Dr Adam Brant and Dr Nancy Giles for their help in my research. I need to give a huge thanks to the lab technicians Greg Smith and Michael Ranft who are always there when you need something and keep things running. Lastly, I owe the folks at AFRL/RXLM (Dr Jay Tiley, Mr Allan Smith, and Mr Adam Shiveley) thanks for allowing me the use of the x-ray equipment in their labs. Without those x rays, a lot of research could not have been accomplished!

Douglas A. Buchanan

## Table of Contents

	Page
Abstract.....	iv
Acknowledgments.....	vi
List of Figures.....	ix
List of Tables.....	xii
I. Introduction.....	1
1.1. Motivation.....	1
II. Experimental Techniques.....	11
2.1. Electron Spin.....	11
2.2. Electron Paramagnetic Resonance.....	14
2.3. EPR Spectrometer.....	19
2.4. EPR Sensitivity .....	21
2.5. Electron-Nuclear Double Resonance.....	22
2.6. Spin Hamiltonian.....	25
2.7. EPR and ENDOR Instrumentation.....	31
2.8. Optical Absorption Spectroscopy.....	33
2.9. Fluorescence Spectroscopy.....	37
III. Characterization of the Intrinsic Hole Center in Lithium Tetraborate.....	40
3.1. Introduction.....	40
3.2. Thermoluminescence Results.....	41
3.3. Electron Paramagnetic Resonance Results.....	43
3.4. Electron-Nuclear Double Resonance Results.....	51
3.5. Spin Hamiltonian.....	53
3.6. Discussion.....	56



IV.	Perturbed and Unperturbed Hole Centers ( $\text{Ag}^{2+}$ Ions).....	65
4.1.	Background.....	65
4.2.	EPR Results.....	74
4.3.	Discussion.....	83
V.	Identification of Radiation-Induced Point Defects in Copper-Doped Lithium Tetraborate Crystals.....	86
5.1.	Introduction.....	86
5.2.	X-Ray-Induced Electron Centers in Copper-Doped LTB.....	87
5.3.	X-Ray-Induced Hole Centers in Copper-Doped LTB.....	97
5.4.	Thermal Stability of the Radiation-Induced Centers.....	102
5.5.	Discussion.....	105
VI.	Optical Properties of Silver-Doped Lithium Tetraborate Crystals.....	106
6.1.	Optical Experiment.....	106
6.2.	Discussion.....	112
VII.	Conclusions.....	113
7.1.	Summary of Findings.....	113
7.2.	Future Work.....	116
Appendix A	Experimental Data.....	118
Appendix B	Sample EPR and ENDOR Computer Routines.....	123
Bibliography	.....	139

## List of Figures

Figure	Page
1.1. Neutron capture cross-sections of various isotopes .....	3
1.2. Energy band structure illustrating scintillation .....	6
1.3. Basic structural component of the $\text{Li}_2\text{B}_4\text{O}_7$ crystal lattice .....	9
2.1. Illustration of Zeeman splitting for an electron in a magnetic field .....	13
2.2. An EPR absorption curve and its corresponding first derivative .....	16
2.3. Energy level splitting due to an $I = 1/2$ hyperfine interaction .....	18
2.4. EPR Spectrometer diagram .....	20
2.5. The two possible cases for an ENDOR spectrum where $S = 1/2$ and $I = 1/2$ ...	26
2.6. Configuration-coordinate energy diagram .....	34
2.7. Diagram of a spectrophotometer .....	36
2.8. Diagram of a fluorescence spectrometer .....	38
3.1. TL glow curve of an LTB crystal irradiated with x rays at 77 K .....	42
3.2. EPR spectrum of the intrinsic trapped hole center in an $\text{Li}_2\text{B}_4\text{O}_7$ crystal .....	44
3.3. Energy level diagram for an electron spin $S = 1/2$ interacting with two equivalent $^{11}\text{B}$ nuclei of spin $I = 3/2$ isotopes .....	45
3.4. Four $(\text{B}_4\text{O}_9)^{6-}$ units comprising the LTB crystal lattice .....	48
3.5. ENDOR spectra collected as the magnetic field was rotated from the $c$ axis to the $a$ axis in 20 degree increments .....	53
3.6. ENDOR angular dependence plot of intrinsic hole trap .....	56
3.7. Schematic representation of the basic $(\text{B}_4\text{O}_9)^{6-}$ structural building block in $\text{Li}_2\text{B}_4\text{O}_7$ crystals.....	59
3.8. Representative EPR spectrum from a trapped hole center in an LBO crystal ..	60
3.9. Basic structural unit of an $\text{LiB}_3\text{O}_5$ crystal .....	61

Figure	Page
4.1. Energy level diagram for the $\text{Ag}^{2+}$ hole centers .....	67
4.2. ENDOR spectra collected for the unperturbed and perturbed $\text{Ag}^{2+}$ hole centers .....	70
4.3. EPR spectra of perturbed (P) and unperturbed (U) $\text{Ag}^{2+}$ ions in LTB .....	72
4.4. Angular dependence data collected while the magnetic field was rotated between the $c$ and the $a$ axes of the crystal in LTB:Ag .....	75
4.5. Four independent sets of data where all of the EPR transitions for the $\text{Ag}^{2+}$ hole center can be identified .....	76
4.6. Angular dependence comparison plot .....	80
4.7. EPR angular dependence plot of LTB:Ag perturbed hole trap .....	81
5.1. EPR spectrum of x-ray irradiated copper-doped lithium tetraborate .....	88
5.2. Breit-Rabi energy level diagrams illustrating the interaction of an $S = 1/2$ electron spin interacting with an $I = 3/2$ nuclear spin .....	90
5.3. Diagram illustrating the spectral splittings of $\text{Cu}^0$ electron center #1 taking both isotopes into account and the superhyperfine splitting from a $^{11}\text{B}$ nucleus .....	92
5.4. Expanded view of the lowest “group” of lines for the two $\text{Cu}^0$ electron centers .....	93
5.5. EPR spectrum showing the $\text{Cu}^{2+}\text{-V}_{\text{Li}}$ characterized by Corradi et al.[71] and EPR spectrum showing both the $\text{Cu}^{2+}\text{-V}_{\text{Li}}$ center and the radiation induced $\text{Cu}^{2+}$ -active center after irradiation.....	98
5.6. EPR spectra of the $\text{Cu}^{2+}\text{-V}_{\text{Li}}$ and $\text{Cu}^{2+}$ -active centers .....	100
5.7. Thermal stabilities of the $\text{Cu}^{2+}$ -active hole center and the two $\text{Cu}^0$ electron centers, as determined from the magnitudes of their EPR spectra .....	104
6.1. EPR Spectrum illustrating the x-ray radiation induced electron and hole centers in LTB:Ag .....	107
6.2. Optical absorption of pre- and post-x-ray irradiated LTB:Ag crystals .....	108
6.3. Emission (PL) spectra of pre- and post- x-ray irradiated LTB:Ag crystals ....	110

Figure	Page
6.4. Excitation (PLE) spectra of pre- and post- x-ray irradiated LTB:Ag crystals .....	110
6.5. Absorption spectra combined with PLE spectra of LTB:Ag crystals .....	111
6.6. Absorption spectra taken during isochronal annealing experiment .....	111

## List of Tables

Table	Page
3.1. Principal values and principal angles of the g, A, and Q matrices for the hole center in LTB.....	55
3.2. Principal values obtained for trapped hole centers in LBO .....	63
4.1. Spin-Hamiltonian parameters calculated using EPR spectra alone for the unperturbed $\text{Ag}^{2+}$ hole center .....	78
4.2. Spin-Hamiltonian parameters calculated using EPR and ENDOR for the unperturbed $\text{Ag}^{2+}$ hole center .....	79
4.3. Spin-Hamiltonian parameters calculated using only EPR for the perturbed $\text{Ag}^{2+}$ hole center .....	80
5.1. Isotropic spin-Hamiltonian parameters for $\text{Cu}^0$ electron centers #1 and #2 ....	96

# **EPR AND ENDOR STUDIES OF POINT DEFECTS IN LITHIUM TETRABORATE**

## **I. Introduction**

### **1.1. Motivation**

Since the early 1990s, United States national defense strategy has shifted from the cold-war era threat of the Soviet Union to an asymmetric threat environment. One of these threats has been the rise in terrorism. Terrorist groups, namely al-Qaeda, have shown an ability to be clever and furtive in their plots to attack the US and its allies. Terrorist groups have shown interest in seeking and deploying weapons of mass destruction and mass disruption--weapons that might kill no one but would create widespread psychological trauma. In testimony before the Senate Foreign Relations Committee on March 6, 2011, some of the nation's top nuclear officials said "dirty bombs" could become the terrorist's weapon-of-choice. A dirty bomb, also called a radiological weapon, would use conventional explosives to spread radioactive materials. Likely radioactive elements for these devices would be cesium, cobalt, and iridium isotopes since they are widely used for industrial purposes and are easily acquired. These materials could also be used in a dirty bomb or, even worse, a nuclear bomb. In June 2011, conventional bombs disguised in computer ink cartridges were timed to blow up aboard commercial aircraft while flying over the US. The material in these devices could easily have been "laced" with radioactive material to magnify the effect. It is a national priority to detect clandestine radioactive materials before they can be transported and exploited by terrorists within the US. Border officials and other security forces must

possess the proper equipment to be able to detect these unauthorized radiological materials.

Radioactive decay is a process where an unstable nucleus loses energy by emitting particles and high energy photons. Typical decay processes involve the emission of alpha and beta particles and gamma rays. There are commercial instruments that are capable of detecting these decay products, but shielding reduces the effectiveness of these devices in detecting radioactive decays. On the other hand, neutron emission, which is also a product of radioactive decay and spontaneous fission can be used as an indicator of the presence of radioactive material. Thus, their detection can be an indication of the presence of nearby radioactive material. Because neutrons have no charge, detecting them needs to be done through a reactionary process.

Currently, neutron detectors are commercially available, but they are neither compact nor cost effective. He-3 detectors and BF<sub>3</sub> tubes are two examples. Some detectors operate by monitoring visible luminescence when neutron capture occurs [1]. They are most efficient in detecting neutrons with energy of 30 meV or less [2]. A typical fissile decay from radiological material emits neutrons of 1.5 MeV, so detectors use thick moderators to slow the neutrons. These moderators, however, reduce the flux of neutrons. Some current detectors also need large chambers and high-voltage power sources which make them bulky and less portable.

Solutions to the limitations of current neutron detectors are emerging. One possibility is to use a luminescent material that has a high neutron capture cross section. Several isotopes have been experimentally found to have high neutron capture cross sections: <sup>157</sup>Gd, <sup>10</sup>B, <sup>3</sup>He, and <sup>6</sup>Li. Their capture cross sections, specified in barns, are plotted as a

function of neutron energy in Fig. 1.1. The capture cross sections of these nuclei are orders of magnitude larger than most other nuclei at the meV (thermal neutron) range. The present dissertation focuses on single crystals of lithium tetraborate, a material that has concentrations of lithium and boron nuclei and thus is potentially useful for neutron detection.

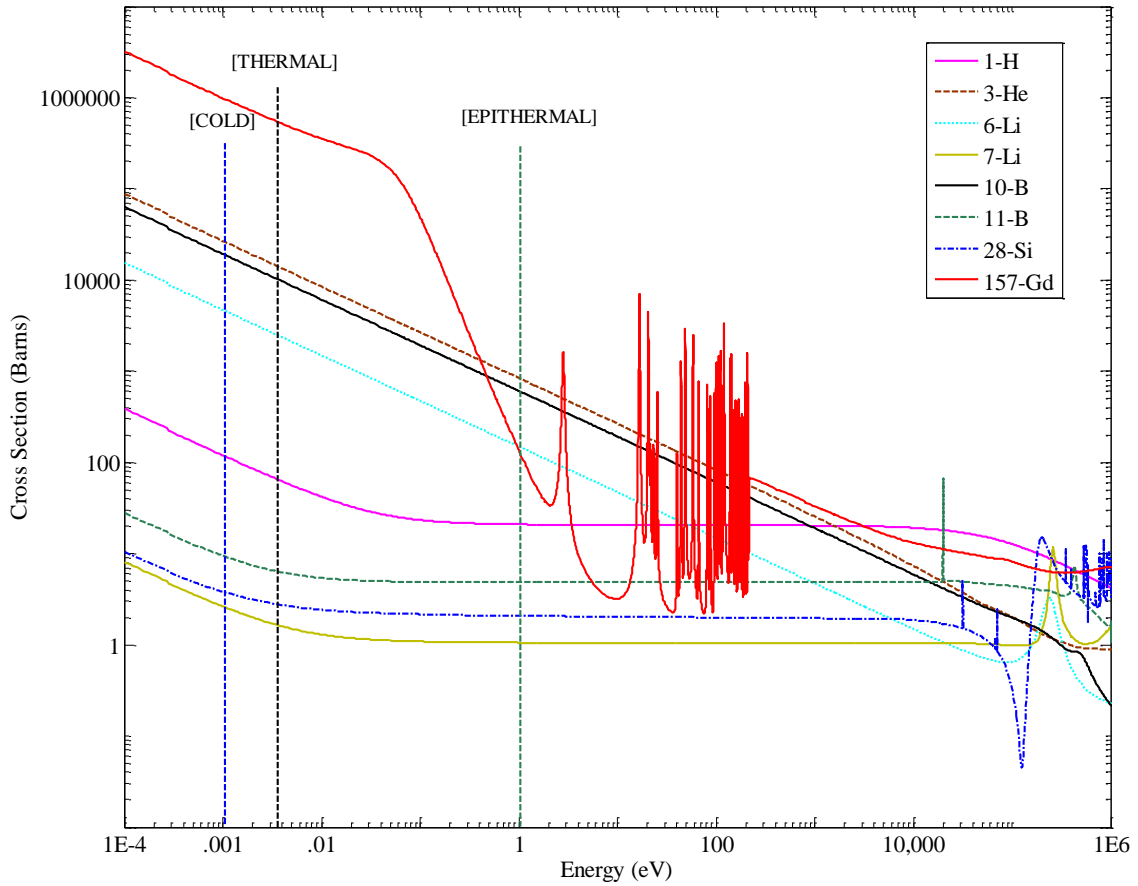


Figure 1.1. Neutron capture cross-sections of various isotopes [3].

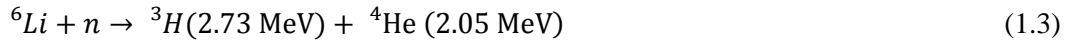
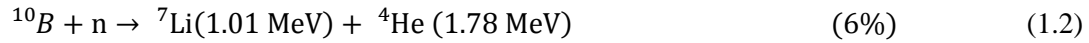
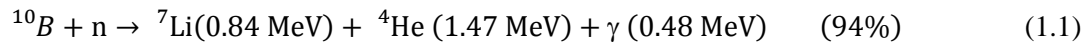
Lithium tetraborate ( $\text{Li}_2\text{B}_4\text{O}_7$ ), commonly referred to as LTB, is a versatile insulating crystal with potential use in neutron detection. LTB can be grown using enriched  $^6\text{Li}$  and  $^{10}\text{B}$  to increase its neutron opacity [4]. When doped with an appropriate optically active



element, LTB could be used as an effective scintillation material. Candidate elements are cerium or erbium because of their excellent luminescent properties in other crystals [5].

Lithium tetraborate, has been grown pure and doped with many different elements including transition metals, actinides, and rare earth elements. The research in this dissertation addresses undoped lithium tetraborate as well as LTB doped with copper and silver.

The following nuclear reactions for lithium and boron involve neutron capture.



In these reactions, both lithium and boron isotopes absorb neutrons and then decay by releasing alpha particles and lithium or tritium nuclei, along with energy. Since  $^{10}\text{B}$  only has a 20% natural abundance and  $^6\text{Li}$  has an even smaller 7% abundance, materials need to be enriched with  $^{10}\text{B}$  and  $^6\text{Li}$  to give them significantly higher neutron capture cross sections.

Consider an enriched LTB crystal. If a thermal neutron is captured by a lithium or boron atom in the crystal lattice, an energetic alpha particle would be released according to Eqs 1.1 - 1.3. Alpha particles will not travel far, on the order of microns in pure silicon for example [2]. During this time, the positive charge of the high speed alpha particle will attract electrons and cause them to leave their lattice bonds and move about the crystal lattice as conduction electrons. Many of these electrons will absorb energy from the alpha particles. The alpha particles will thus lose kinetic energy and eventually

combine with two electrons to form helium atoms. The conduction electrons formed may be detected indicating neutron capture.

As alpha particles travel in the crystal lattice, there are two features that could aid in neutron detection. First, electrons that absorb energy from the alpha particles become conducting electrons in the crystal. If the material were biased with a voltage, a change in the resulting current could be measured indicating neutron absorption. This principle is the basis of solid state detectors. Second, many scintillators emit photons when the crystal is excited by energy depositions. In scintillating materials, “excited” electrons recombine with “holes” in the crystal lattice and release electromagnetic radiation that can be detected using a photomultiplier tube. If a neutron absorbing material such as lithium tetraborate is attached to a photomultiplier tube and placed in the vicinity of radioactive materials, alpha particles would be created when neutrons react with boron and lithium atoms in the crystal. These alpha particles will, in turn, create electrons in the conduction band. These electrons could participate in radiative recombination processes in the lattice, i.e., scintillate, and produce a measureable signal in a photomultiplier tube.

To explain scintillation (shown in Fig. 1.2), first consider that semiconducting and insulating materials have a band gap, or forbidden energy region. The energy levels below this gap are called the valence band and represent those electrons that are bound to lattice sites or form bonds between ions. When an electron gains energy, perhaps from ionizing radiation (See step A in Fig. 1.2), it can be excited across this gap into the conduction band (See step B in Fig. 1.2). Electrons in the conduction band are no longer localized and have enough energy to move about the crystal lattice. The missing electron

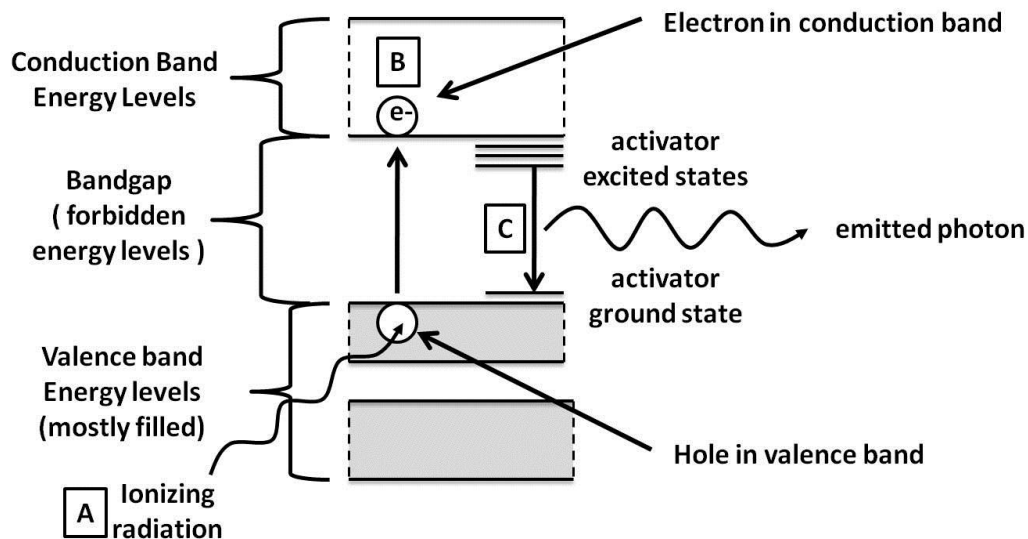


Figure 1.2. Energy band structure illustrating scintillation.

in the valence band is called a hole, where holes can conduct about the crystal lattice as well. Many materials contain impurities that are present either intentionally or unintentionally. Impurities may allow energy levels to exist in the band gap. These impurities are sometimes called activators. A conducting electron may fall into an activator site after first giving up some of its energy, i.e., through a phonon interaction. From the activator location, the electron then emits energy via a photon of energy that is less than the band gap of the material and returns to the valence band (See step C in Fig. 1.2). In other words, the electron recombines with a hole in the valence band and thus returns the crystal to its pre-irradiated equilibrium state.

Once an electron has returned to the valence band via an acceptor site, the emitted photon could be measured by converting it to an electron using the photoelectric effect. Photomultiplier tubes are designed to first convert incident photons into a current of electrons. These tubes then multiply the electrons produced millions of times by the

process of secondary emission. The efficiency of current production in a photomultiplier tube depends on the wavelength of incident photons. Photomultiplier tubes are most efficient in the visible spectrum. With this very high sensitivity, a photomultiplier tube could be combined with a properly doped lithium tetraborate crystal known to scintillate in the visible spectrum and become an inexpensive and compact solution in detecting neutron radiation.

Electrons can release energy through processes other than scintillation in order to return to the valence band. Various unintentional impurities and dislocations create energy levels within the band gap where nonradiative recombinations can occur. For this reason, unintentional contamination or poor crystal growth, i.e., crystals that do not grow uniformly, must be avoided or corrected with post growth techniques such as annealing. Materials are commonly “doped” with specific impurities that allow energy levels to exist inside the band gap and to increase the probability of scintillation.

In order to elaborate further on lithium tetraborate’s potential as a scintillating material, consider the alpha particles produced in the reactions described in Eqs. 1.1 - 1.3. These particles range in energy from 1.47 to 2.05 MeV. For a wide category of materials, energy on the order of three times the band gap energy is required to create one electron-hole pair [2]. If an alpha particle of 1.47 MeV gave up two thirds of its energy in LTB with an approximate 10 eV band gap, 32,700 electron-hole pairs would be produced. Various experimental determinations have shown that the absolute scintillation efficiency of thallium-activated sodium iodide is about 12%. If LTB were only 8% efficient, an alpha particle would provide 78,400 eV in total light energy, or 28,500 photons that have a 450 nm wavelength. At 8% efficiency, LTB would still have one emitted photon for

each electron hole pair created making it a good candidate as a scintillating material to be used in neutron detection. Also, a thin sample of LTB with its low  $Z$  would make it nearly gamma blind, i.e., gamma radiation would not likely produce additional electrons in the conduction band because the gammas would pass through the thin sample without interacting with the crystal nuclei.

LTB has other valued commercial uses. It has been applied to dosimetry and scintillation detectors [6-7] and also has potential uses in the fields of acousto-electronics, and optics [6, 8-10]. LTB exhibits piezoelectric coupling values that fall between those of lithium niobate and quartz, and possesses orientations for which the temperature coefficient of frequency and delay time is zero for bulk and surface acoustic waves [11]. Despite LTB's potential as either a primary or companion material in future electronic devices, there is still a lack of fundamental characterization, particularly regarding the defect-related properties.

The ideal lithium tetraborate crystal belongs to the space group  $I4_1cd$  (tetragonal  $I4cd$ , the point group is  $4mm$ ) and possesses 104 atoms per unit cell. LTB has lattice constants  $a = 9.475 \text{ \AA}$  and  $c = 10.283 \text{ \AA}$  at room temperature [12-16]. On the left side of Fig. 1.3, a basic  $(B_4O_9)^{6-}$  building block—one of eight as part of the conventional unit cell—is displayed along with a neighboring lithium ion. The  $c$  axis is oriented upward and toward the left (see the right side of Fig. 1.3). A tetragonal structure like LTB has two  $a$  axes ( $a = b$  in Fig. 1.3) due to its symmetry. The full unit cell, on the right hand portion of Fig. 1.3, is meant to illustrate the complexity of the crystal. The left portion of Fig. 1.3 shows the basic building block of an LTB crystal structure with the appropriate

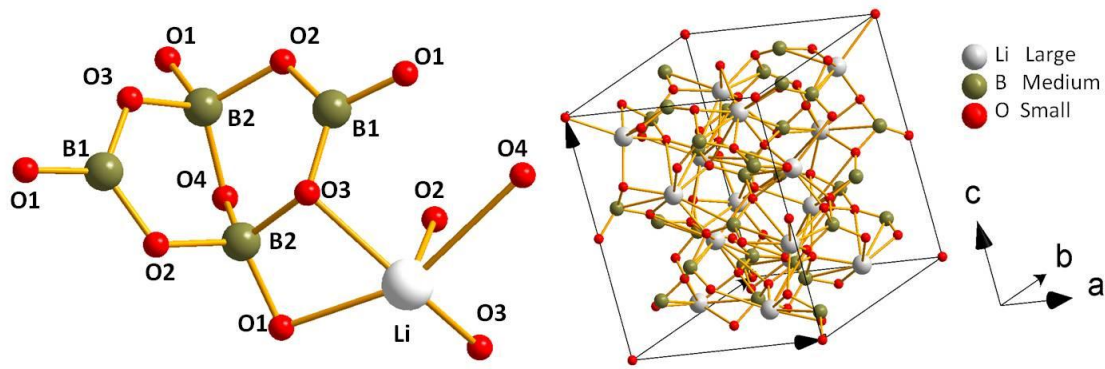


Figure 1.3: Basic structural component of the  $\text{Li}_2\text{B}_4\text{O}_7$  crystal lattice (left) and a unit cell of  $\text{Li}_2\text{B}_4\text{O}_7$  (right).

equivalent atoms labeled. The extra O2, O3, and O4 on the lithium are additional to the basic structure. They are shown to aid visualizing the other lithium atoms in the lattice.

All crystals have point defects that occur during growth. These defects often affect the bulk properties of solids such as sub-band-gap optical absorption or emission and affect the mechanical and electrical properties as well. For example, the F center in potassium chloride consists of an electron trapped in a chloride ion vacancy. These F centers cause the normally colorless potassium chloride crystals to appear dark blue.

Electron paramagnetic resonance (EPR) and electron-nuclear double resonance (ENDOR) are powerful techniques in determining defect structure [17]. Their restriction is, of course, that the defects must be paramagnetic. Fortunately, EPR has demonstrated that an x-ray irradiated sample of undoped LTB produces spectra due to oxygen and lithium vacancies. The lithium vacancies trap holes and are the subject of Chapter Three. Further, there are x-ray irradiated spectra produced in both silver and copper doped LTB crystals. EPR spectra are also present in copper doped LTB crystals without the need for

irradiation. Chapters Four and Five describe the EPR behavior of silver and copper in LTB. Chapter Six presents the optical properties of the silver defects characterized with EPR in Chapter Four.

The characterization of point defects in lithium tetraborate that are described in this dissertation will aid in developing devices utilizing this material. These studies may also help clarify crystal-growth properties and suggest improvements. For example, the large concentrations of lithium vacancies in LTB (discussed in Chapter Three) could possibly be reduced by heating crystals close to their melting point while immersed in a lithium-containing powder. This process, known as vapor phase equilibration, has been successfully used to eliminate lithium vacancies in lithium tantalate and lithium niobate crystals [18].

## II. Experimental Techniques

### 2.1. Electron Spin

O. Stern and W. Gerlach, in 1922, used a beam of silver atoms to demonstrate that the magnetic moment of an electron could only have discrete orientations in a magnetic field. In their experiment, silver atoms passed through a region of magnetic field and struck a target placed a short distance beyond the magnet. A continuous line along the horizontal axis of their target, due to the slit shape of the collimator, was predicted for the silver atoms since they do not possess orbital angular momentum, i.e.,  $L = 0$ , and thus were assumed to have zero magnetic moment. To Stern and Gerlach's surprise, the atoms struck the target in two specific regions above or below their predicted horizontal line. Later in 1925, G. Uhlenbeck and S. Goudsmit explained Stern and Gerlach's experiment by assuming that the electron possessed an intrinsic magnetic moment that was due to an intrinsic angular momentum, thus the creation of a quanta of spin [19]. Silver, with one unpaired electron, has a spin of  $S = 1/2$ . This intrinsic angular momentum is called the *spin* of an electron. In a magnetic field, the electron spin can only take on discrete values, whereas in the absence of a magnetic field, the energies of the different spin states are degenerate. The application of a magnetic field lifts this degeneracy and splits the energy levels. The split in the energy levels of an electron in the presence of a magnetic field is called the Zeeman splitting.

Single unpaired electrons have a spin value of  $S = 1/2$ , which can take on discrete values of  $m_S = \pm 1/2$ . In general, a spin system with a net spin  $S$  can take on the quantized values  $m_S = -S, -S+1, -S+2$  to  $+S$ . The Zeeman energy associated with the magnetic field splitting is given by,



$$E = -\vec{\mu} \cdot \vec{B} \quad (2.1)$$

where  $\mu$  is the magnetic moment. If the spin states were placed in a magnetic field chosen to be the  $z$  direction, the corresponding Zeeman energy levels would be given by

$$E = -\mu_z B_z \quad (2.2)$$

$$\text{where } \mu_z = -g_e \beta m_s \quad (2.3)$$

The  $z$  direction is chosen to be in the direction of the magnetic field in this chapter to avoid unnecessary complications arising from vector notation and dot products. The quantity  $\beta$  is the Bohr magneton,  $\frac{e\hbar}{2m_e}$  or  $9.274015 \times 10^{-24} \text{ Am}^2$ , and  $g_e$  is the electron spin  $g$ -factor (more often simply called the electron  $g$ -factor). The electron  $g$  factor has a value of 2.002319 for a free electron and is known to extremely high precision [20]. The energy given in Eq. 2.2 is directly proportional to the magnetic field. The Zeeman splitting of a single electron, with  $S = 1/2$ , is demonstrated in Fig. 2.1. In this figure, the separation between the two  $m_s$  energy levels increases linearly as the magnitude of the magnetic field increases. The transition energy,  $\Delta E$ , is the energy difference between the two spin states of the electron. A transition between these energy levels can be induced when an amount of energy,  $\Delta E = h\nu$ , is provided by an external electromagnetic wave oriented with its magnetic field perpendicular to the static applied magnetic field. This energy is absorbed by the electron and causes it to switch spin states, going from  $-1/2$  to  $+1/2$ . The electrons can then “relax” back by giving energy up, usually by emitting phonons. The basis of an EPR experiment involves inducing a change in the spin state of an unpaired electron and detecting the absorption of energy that takes place.

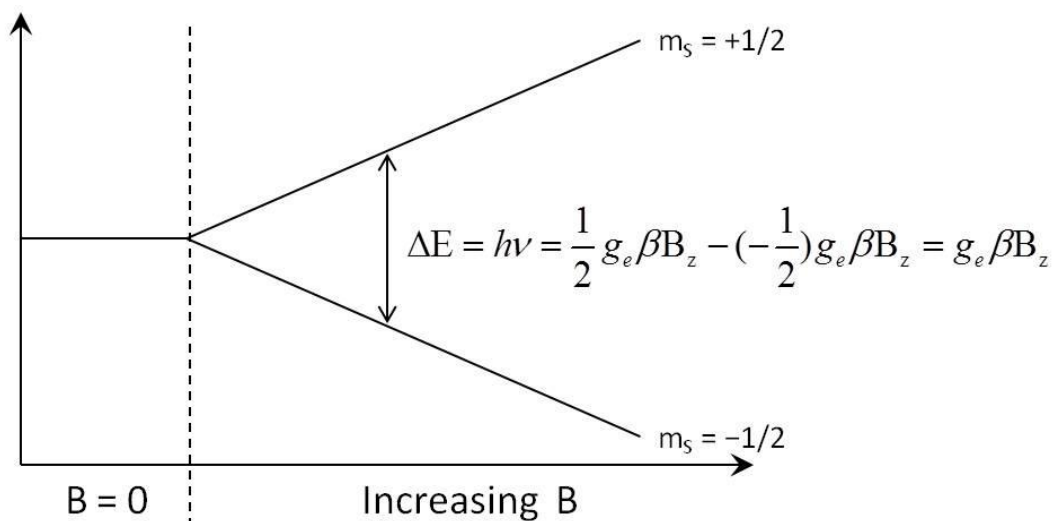


Figure 2.1. Illustration of Zeeman splitting for an electron in a magnetic field.

Unpaired electrons in crystals, free radicals, and many other paramagnetic entities have electron  $g$  factors that differ from the free-electron value. The difference in the  $g$  factor is due to the environment in the vicinity of the electron. This can cause shifts and splittings in the Zeeman energy levels. The reasons for these shifts and splittings in crystals will be discussed later in this chapter. A spin Hamiltonian is used to represent the spin-related energy of a paramagnetic system. The discrete energy levels associated with an electron spin can be measured using electron paramagnetic resonance (EPR) spectroscopy. These energies that an EPR experiment measures represents the diagonal elements of the modeled spin Hamiltonian. From these energies, the parameters describing the spin Hamiltonian can be determined using a least-squares fitting process. The spin Hamiltonian is often too complex to fit without the aid of a computer. These extracted spin Hamiltonian parameters provide information about the local spin environment and are useful in establishing defect models.

## 2.2. Electron Paramagnetic Resonance (EPR)

Electron paramagnetic resonance spectroscopy can be used to determine the local environment surrounding an unpaired electron. Electron paramagnetic resonance (EPR), or as it is sometimes called electron spin resonance (ESR), is a technique for studying point defects in inorganic crystals and amorphous solids, acceptors and donors in narrow-band-gap and wide-band-gap semiconductors, and chemical species that have one or more unpaired electrons such as organic and inorganic free radicals and spin labels. EPR was first observed at Kazan State University by Soviet physicist Yevgeny Zavoisky in 1944, and was developed independently following World War II by Brebis Bleaney at the University of Oxford [21].

In a simplified description, EPR works by: (1) placing a paramagnetic material in a static magnetic field, (2) applying a microwave frequency ( $\nu$ ) with the microwave magnetic field perpendicular to the static magnetic field such that the spin states will undergo a transition due to the absorption of energy,  $\Delta E = h\nu$ , and finally (3) detecting this absorption. The  $g$  factor can then be determined by solving the following resonance equation.

$$\Delta E = h\nu = g_z \beta B_z \quad (2.4)$$

Conceptually, the simplest way to conduct an EPR experiment would be to hold the static magnetic field fixed at some value and then sweep through a range of frequencies while monitoring for the absorption of energy. This is how many optical spectrometers operate. However, sweeping the frequency is not feasible in an EPR spectrometer because that would require changing the physical dimensions of the microwave cavity as the sweep progresses. (A microwave cavity only resonates at one frequency for a given

set of dimensions.) In practice, the static magnetic field is slowly swept in EPR spectrometers while the microwave frequency is held constant.

EPR spectrometers typically operate with magnetic fields up to 1.3 Tesla (13,000 gauss). For a static magnetic field value of 3,400 gauss and a  $g$  value of 2.0023, the necessary frequency would be 9.5284 GHz, which is in the X-band for microwaves and is the frequency where many EPR spectrometers operate. As the magnetic field is swept through a region of interest, the spin system will go through one or more resonances where microwave energy is absorbed. The output of an EPR spectrometer is absorption versus magnetic field. In actual experiments, the output of the spectrometer does not show absorption curves, but rather their first derivatives. This is because of an applied modulation, usually with a frequency of 100 kHz that produces an AC contribution to the static magnetic field. This modulation, when coupled with a phase-sensitive detector, dramatically increases the sensitivity of the EPR spectrometer. Descriptions of how this modulation process produces the first derivative can be found in literature [22]. The output of an EPR spectrometer is thus the first derivative of the absorption curve, as illustrated in Fig. 2.2.

EPR spectra are usually more complicated than just a single derivative spectrum.

Electrons interact with other magnetic moments or electric quadrupole moments that are part of the same atom or are nearby and this causes the spin related energy levels to split and possibly shift. When an electron interacts with a nearby nucleus that has a non-zero spin, the electron Zeeman levels will be split. This is called the hyperfine interaction.

Combining Eqs. 2.2 and 2.3, electrons have Zeeman energy levels described by

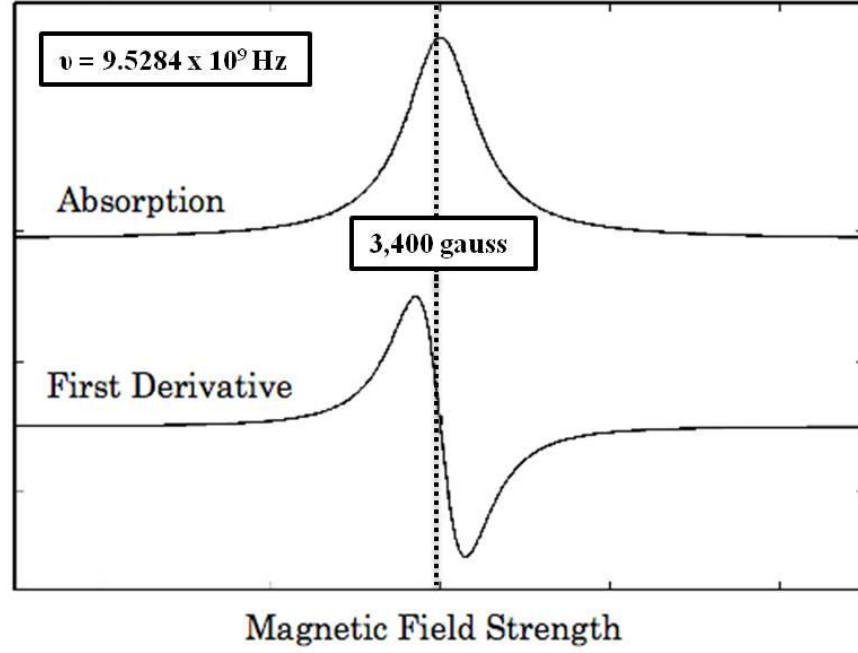


Figure 2.2. An EPR absorption curve (top) and its corresponding first derivative (bottom) [23].

$$E(m_S) = g \beta m_S B_z \quad (2.5)$$

where

$$E\left(+\frac{1}{2}\right) = \frac{1}{2} g \beta B_z$$

$$E\left(-\frac{1}{2}\right) = -\frac{1}{2} g \beta B_z$$

When an electron spin  $S = 1/2$  interacts with a nuclear spin  $I = 1/2$ , the energy is described by

$$E(m_S, m_I) = g \beta m_S B_z + h A m_S m_I \quad (2.6)$$

where the second term in Eq. 2.6 is called the hyperfine term or hyperfine interaction.

The four possible energy levels of this  $S = 1/2$ ,  $I = 1/2$  spin system are now described using  $E(m_S, m_I)$ .

$$E\left(+\frac{1}{2}, +\frac{1}{2}\right) = \frac{1}{2} g \beta B_z + \frac{1}{4} h A$$

$$E\left(+\frac{1}{2}, -\frac{1}{2}\right) = \frac{1}{2} g \beta B_z - \frac{1}{4} h A$$

$$E\left(-\frac{1}{2}, -\frac{1}{2}\right) = -\frac{1}{2} g \beta B_z + \frac{1}{4} h A$$

$$E\left(-\frac{1}{2}, +\frac{1}{2}\right) = -\frac{1}{2} g \beta B_z - \frac{1}{4} h A$$

EPR transitions occur when  $\Delta m_s = \pm 1$  and have the restriction that  $\Delta m_l = 0$ . Figure 2.3 describes these energy levels due to the hyperfine splitting with the possible EPR transitions shown using red arrows. The resulting spectrum corresponds to two EPR transitions centered about the electron's g-factor and separated by  $A$  (the hyperfine parameter). The two peaks shown in Fig. 2.3 occur when

$$\Delta E_1 = h\nu = E\left(\frac{1}{2}, \frac{1}{2}\right) - E\left(-\frac{1}{2}, \frac{1}{2}\right) = \frac{1}{2} g \beta B_{1z} + \frac{1}{2} h A$$

and

$$\Delta E_2 = h\nu = E\left(\frac{1}{2}, -\frac{1}{2}\right) - E\left(-\frac{1}{2}, -\frac{1}{2}\right) = \frac{1}{2} g \beta B_{2z} - \frac{1}{2} h A$$

If the hyperfine interaction is large and the EPR linewidths are narrow, a hyperfine parameter can be determined directly from an EPR spectrum. If, however, the hyperfine interaction is small and the EPR linewidths are large, the hyperfine splitting is not resolved in an EPR spectrum. In this latter case, electron-nuclear double resonance (ENDOR) may be used to determine the hyperfine parameter. ENDOR will be discussed later in this chapter. Figure 2.3 is the simplest case of a hyperfine interaction (an electron of spin 1/2 interacting with a nucleus of spin 1/2). An EPR spectrum becomes more complicated for systems that have larger electron and nuclear spin values. The number

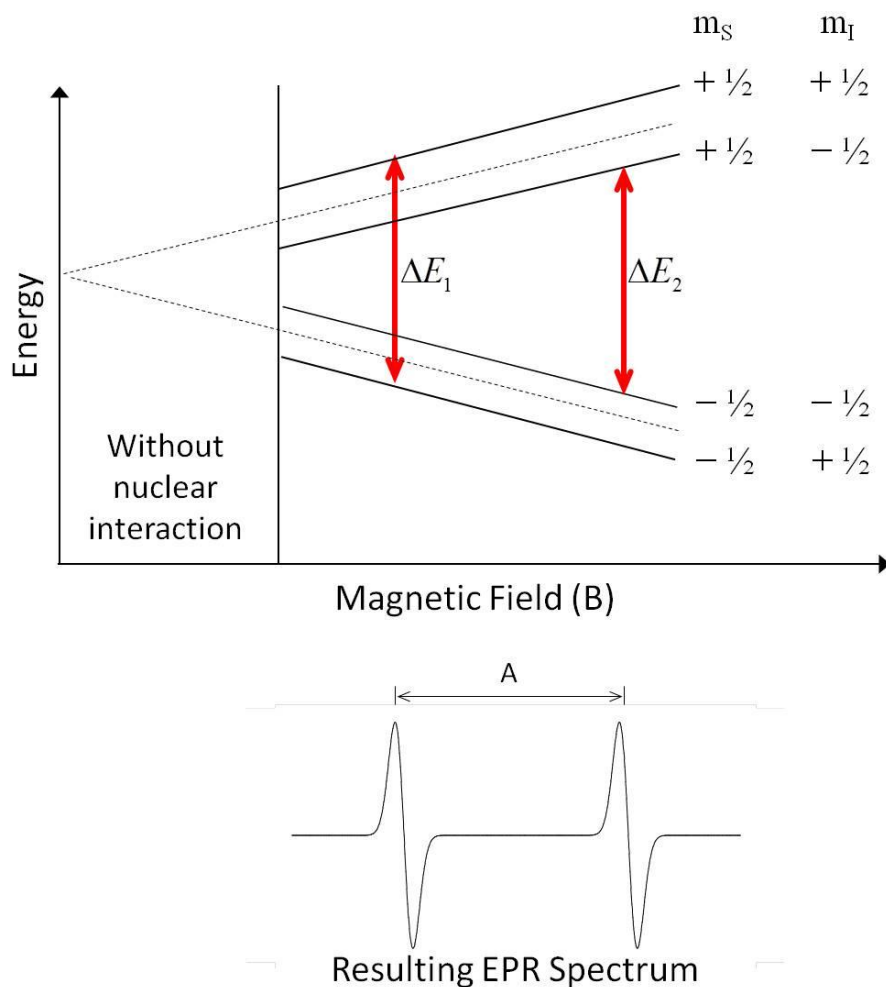


Figure 2.3. Energy level splitting due to an  $I = 1/2$  hyperfine interaction (upper). The resulting EPR spectrum (lower).

of spin-related energy levels is  $(2S + 1) \cdot (2I + 1)$  and the number of EPR transitions is  $(2S) \cdot (2I + 1)$ , where the selection rules  $\Delta m_S = \pm 1$  and  $\Delta m_I = 0$  have been invoked. For example, an  $^{57}\text{Fe}^{3+}$  ion has 5 unpaired electrons ( $S = 5/2$ ) and has an  $I = 1/2$  nuclear spin value. This would result in twelve level energy diagram with ten possible EPR transitions. So, rather than observing a large single EPR transition in the spectrum, there would be ten transitions (or lines) with the same total area under them as a large single transition. For this reason low concentration spin systems with large  $S$  and  $I$  values may

have EPR signals with low intensities that do not significantly rise above the background noise. There are other interactions that further complicate an EPR spectrum. This will be discussed in the section titled “Spin Hamiltonian.”

### **2.3. EPR Spectrometer**

An EPR spectrometer collects data by using a microwave “bridge,” schematically shown in Fig. 2.4. The role of each major component in the diagram will be discussed and related to the operation of the EPR spectrometer. To begin, the microwave source is located in the lower left portion of Fig. 2.4. Historically, klystrons produced the microwaves but present day instruments use solid state Gunn diodes as the microwave source. After leaving the Gunn diode, the waveguide branches into two arms. The signal arm contains the microwaves that continue down to the resonant cavity containing the sample to be studied. There is an attenuator in the signal arm, shown by a variable resistor symbol, that controls the amount of microwave energy reaching the sample cavity. The actual attenuator is a lossy dielectric material that is moved in and out of a section of the waveguide. In many EPR experiments it is important to be able to vary the microwave power level with the attenuator because the EPR signal may “saturate” at higher power levels. Saturation occurs when the microwaves are too intense upon the sample cause the population of the upper and lower energy states to become nearly equal; this results from a long spin-lattice relaxation time that prevents spins in the upper state from quickly relaxing to the lower state. The power level of the microwaves is a crucial element in collecting good EPR spectra and may need to be adjusted when looking at different defects in the same crystal or different orientations of the same defect.



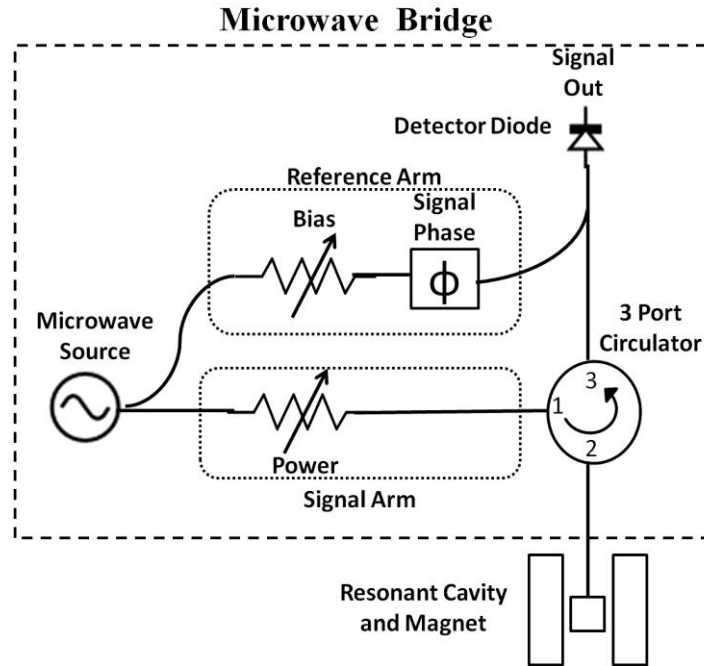


Figure 2.4. EPR Spectrometer diagram [23].

Next, the microwaves in the signal arm continue from the attenuator to the three-port circulator, a ferromagnetic device. Entering from port 1, the microwaves continue out port 2 and on to the resonant cavity containing the sample. The cavity is “tuned” such that the microwaves are all absorbed (in other words, the cavity perfectly terminates the waveguide). Effectively, the cavity is impedance matched to the waveguide. The microwave cavity is said to be “critically coupled” when there is no reflected microwave power. Absorption of microwaves, which occurs when the magnetic field satisfies the resonance condition, causes the microwave cavity to become slightly uncoupled and thus reflects microwave power back up the waveguide and into port 2 of the circulator. These reflected microwaves from the cavity then pass out of port 3 of the circulator and continue on to the detector diode. The detector diode is a semiconductor junction that

creates current proportional to the incident microwave power and produces the measured EPR signal.

Separately, there is the reference arm of the microwave bridge. This portion of the waveguide performs two functions. First, it provides microwave energy that serves to “bias” the detector diode. This “bias” energy incident on the detector diode does not come from the cavity containing the sample, but instead comes directly from the Gunn diode through the reference arm to the detector diode. The purpose of the detector bias is to increase the spectrometer’s detection sensitivity. In an EPR spectrometer, the detector is a Schottky barrier diode that can operate either in the square law region (where the electrical power is proportional to the square of voltage or current) or in the linear region. The square law region occurs at powers of less than a microwatt. At higher incident powers, the diode operates in the linear region. This is the region of greatest sensitivity. Thus, biasing the diode (via the Reference Arm) keeps the detector operating in the linear region. Second, there is a phase shifter in the reference arm that adjusts the phase of the propagating microwaves. The phase of the microwaves in the reference arm are adjusted to match the phase of the microwaves reflected from the cavity containing the sample. With proper bias, sample power, and phase, the EPR microwave bridge and sample cavity will yield optimal EPR spectra.

## **2.4. EPR Sensitivity**

An EPR spectrometer is able to detect very small concentrations of unpaired spins. Under optimal conditions it is easy to observe an EPR signal representing  $10^{11}$  spins [17]. Due to the size of the microwave cavity, samples are typically no more than  $0.03 \text{ cm}^3$  in

volume. Thus the  $10^{11}$  spins corresponds a concentration of approximately  $3 \times 10^{13} \text{ cm}^{-3}$ . Temperature is the most important experimental parameter in an EPR experiment (usually, lower temperature means larger EPR signals). Consider a collection of independent electrons with an upper energy state associated with the spin  $+1/2$  electrons and a lower energy state associated with the spin  $-1/2$  electrons. The populations of the two states follows the classical Boltzmann distribution of  $N_{upper} = N_{lower} e^{\frac{-\Delta E}{k_B T}}$ , where  $\Delta E$  is the energy difference between the two spin levels,  $k_B$  is the Boltzmann constant, and  $T$  is the temperature in Kelvin units. Greater population differences for the spin states (i.e.,  $N_{lower} - N_{upper}$ ) will occur at lower temperatures. For this reason, EPR is conducted at lower temperatures because the intensity of the EPR signal is proportional to the population difference between the spin levels. Many experiments are conducted at temperatures between 20 and 100 K. At extremely low temperatures, the spin-lattice relaxation time becomes longer and this may result in microwave power saturation of the EPR signal. Avoiding saturation is important in an EPR experiment, as it will limit the detection sensitivity. Each paramagnetic defect may have a different temperature dependence of its spin-lattice relaxation time. Therefore, each distinct EPR signal will have an optimal temperature that maximizes its intensity. Each optimal temperature must be determined experimentally.

## 2.5. Electron-Nuclear Double Resonance (ENDOR)

Another experiment that can be performed with an EPR spectrometer is electron-nuclear double resonance, referred to as ENDOR. ENDOR uses the sensitivity of the EPR spectrometer to perform nuclear magnetic resonance (NMR) spectroscopy. Many

nuclei have a non-zero magnetic moment, i.e., they have a nuclear spin. In general, their magnetic moments are three orders of magnitude smaller than those of electrons. While a frequency in the gigahertz range (microwaves) induces EPR transitions, a frequency in the megahertz range (radio waves) induces nuclear spin transitions. Nuclear transitions are described by the same principles previously discussed for electrons, except the selection rule is now  $\Delta m_S = 0$  and  $\Delta m_I = \pm 1$ . The energy splitting of the nucleus due to its intrinsic spin is called the nuclear Zeeman effect. In performing ENDOR with an EPR spectrometer, one “sits” at a specific magnetic field location where an EPR transition occurs. Microwaves are provided to the sample such that the EPR transition becomes saturated, i.e, the populations of the upper and lower spin states become nearly equal. While saturating the EPR transition, the magnetic field of the radio waves and the microwave magnetic field must both be perpendicular to the static magnetic field. The frequency of the radio waves is swept across a region of interest. Nuclear transitions will occur at specific frequencies of the radio waves when the difference between two nuclear Zeeman levels equals the energy of the radio wave photons. During these nuclear transitions, the saturated EPR signal will change in magnitude due to the slight variations in populations caused by the nuclear magnetic resonances. The changes in the intensity of the EPR signal as a function of the radio wave frequency is the ENDOR spectrum. Like EPR, ENDOR spectra also appear as the first derivative of an absorption spectrum. The first derivative shape results from modulating the frequency of the radio waves, usually with a modulation frequency of 20 kHz or less.

To illustrate ENDOR, consider the example of an electron with spin  $S = 1/2$  interacting with a nucleus of spin  $I = 1/2$ . The energy of this spin system was described

by Eq. 2.6. Because of the different selection rules for ENDOR, a nuclear Zeeman interaction term must be included in the spin Hamiltonian. The resulting energy equation becomes

$$E(m_s, m_I) = g \beta m_s B_z + h A m_s m_I - g_N \mu_N m_I B_z \quad (2.7)$$

which can be rewritten as

$$E(m_s, m_I) = g \beta m_s B_z + h A m_I m_s - h \nu_N m_I \quad (\text{where } \nu_N = g_N \beta_N B/h) \quad (2.8)$$

The four possible energy levels are now, using  $E(m_s, m_I)$

$$E\left(+\frac{1}{2}, +\frac{1}{2}\right) = \frac{1}{2} g \beta B_z + \frac{1}{4} h A - \frac{1}{2} h \nu_N$$

$$E\left(+\frac{1}{2}, -\frac{1}{2}\right) = \frac{1}{2} g \beta B_z - \frac{1}{4} h A + \frac{1}{2} h \nu_N$$

$$E\left(-\frac{1}{2}, -\frac{1}{2}\right) = -\frac{1}{2} g \beta B_z + \frac{1}{4} h A + \frac{1}{2} h \nu_N$$

$$E\left(-\frac{1}{2}, +\frac{1}{2}\right) = -\frac{1}{2} g \beta B_z - \frac{1}{4} h A - \frac{1}{2} h \nu_N$$

Using the ENDOR selection rule that  $\Delta m_s = 0$  and  $\Delta m_I = \pm 1$ , the following transitions occur.

$$\frac{\Delta E_3}{h} = \nu_1 = \frac{E}{h}\left(+\frac{1}{2}, +\frac{1}{2}\right) - \frac{E}{h}\left(+\frac{1}{2}, -\frac{1}{2}\right) = \left|\frac{1}{2} A - \nu_N\right|$$

$$\frac{\Delta E_4}{h} = \nu_2 = \frac{E}{h}\left(-\frac{1}{2}, -\frac{1}{2}\right) - \frac{E}{h}\left(-\frac{1}{2}, +\frac{1}{2}\right) = \left|\frac{1}{2} A + \nu_N\right|$$

The energies have been divided by  $h$ . The hyperfine parameter  $A$  and  $\nu_N$  have units of frequency, typically MHz. Depending on the values of  $A/2$  and  $\nu_N$ , there are two possible forms that the ENDOR spectra may take.

Consider first the case where  $A/2 > \nu_N$ . ENDOR transitions occur at the following frequencies given by Eq 2.9.

$$\nu_1 = \frac{A}{2} - \nu_N \quad \text{and} \quad \nu_2 = \frac{A}{2} + \nu_N \quad (2.9)$$

This gives a pair of ENDOR lines centered on  $A/2$  and separated by  $2 \nu_N$ . By measuring the separation of the two ENDOR lines,  $\nu_N$  can be directly determined. The two ENDOR lines will be centered on  $A/2$ .

The second case, for  $\nu_N > A/2$ , gives ENDOR transitions at

$$\nu_1 = \nu_N - \frac{A}{2} \quad \text{and} \quad \nu_2 = \nu_N + \frac{A}{2} \quad (2.10)$$

This results in a pair of lines centered on  $\nu_N$  and separated by  $A$ . These two possible cases are shown in Fig. 2.5. ENDOR can measure hyperfine parameters that are not resolved in EPR experiments. Each element in the periodic table, with a non-zero nuclear spin, has its own unique value of  $\nu_N$ . Therefore, the ENDOR technique can be used to determine the identity of the nucleus responsible for a hyperfine interaction.

A major drawback to ENDOR, however, is the fact that not all EPR signals can be easily microwave power saturated. When attempting to obtain an ENDOR spectrum, the temperature and microwave power must be optimized if success is to be achieved. In some cases, ENDOR spectra are easily observed, while, in other cases no amount of searching will reveal an ENDOR spectrum. The intensity of an ENDOR spectrum is usually one to two percent of the intensity of the corresponding EPR spectrum.

## 2.6. Spin Hamiltonian

An isolated electron would produce a single peak in an EPR spectrum. In crystals,

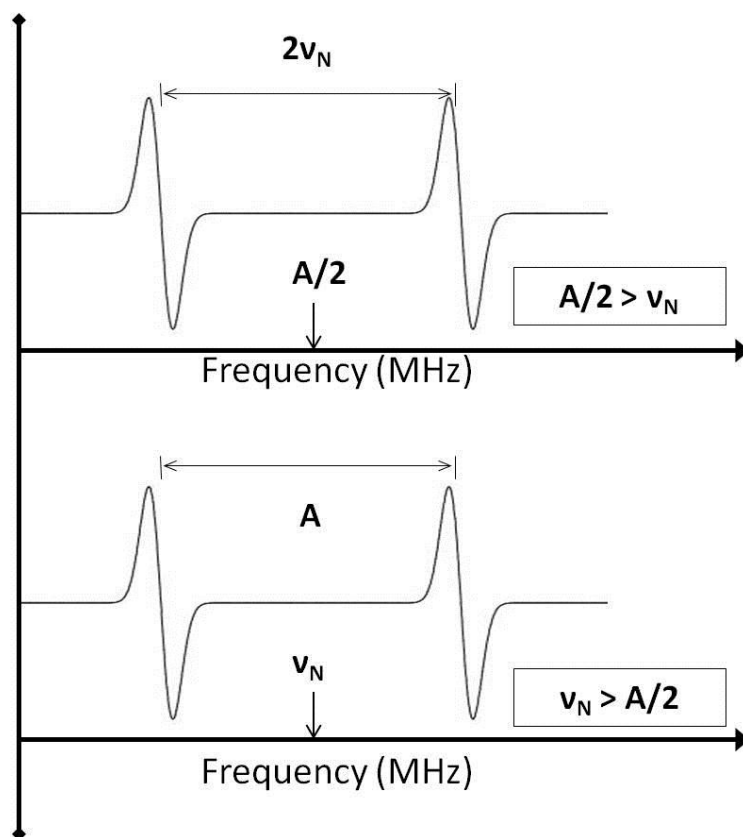


Figure 2.5. The two possible cases for an ENDOR spectrum where  $S = 1/2$  and  $I = 1/2$ .

however, unpaired electrons are influenced by their environment which leads to their having a host of possible energies, and thus more complex EPR spectra. Some of these influences on spin have already been discussed. It is difficult to establish a Hamiltonian that describes all of the influences on an electron, then solve Schrodinger's equation using this Hamiltonian, and finally relate the resulting wave function to the experimental EPR data. Therefore, simplifications are introduced which lead to the concept of a spin Hamiltonian. The spin Hamiltonian includes only the spin-dependent terms in the Hamiltonian. It is used to derive the discrete spin energy levels and determine the

possible transitions between these levels. The energy levels are the eigenvalues of the spin Hamiltonian matrix representing the total energy of the spin system.

Point defects, which are typical of unpaired spin systems in crystals, often exhibit anisotropic behavior. Defect anisotropy requires that the spin Hamiltonian be written in matrix form using the appropriate set of spin vectors as a basis set. The spin Hamiltonian must be expressed in a specific coordinate system. Usually, a coordinate system is chosen with  $z$  being the direction of the static magnetic field (referred to as the magnetic-field coordinate system). The  $g$  and  $A$  matrices, containing the spin-Hamiltonian parameters, are diagonal in their principal-axes coordinate systems. When constructing the spin-Hamiltonian matrix, the  $g$  and  $A$  matrices must be rotated into the magnetic-field coordinate system. For most spin systems, a computer must be used to diagonalize the spin-Hamiltonian matrix.

Each term appearing in a general spin Hamiltonian will now be discussed. There are several excellent books available that provide in depth discussions of a spin Hamiltonian [17, 24,25]. Thus far in this dissertation, the electron Zeeman term containing the  $g$  matrix, the hyperfine term containing the  $A$  matrix, and the isotropic nuclear Zeeman term have been introduced. The equations describing the energies associated with these terms (Eqs. 2.5-2.8) could be written as spin Hamiltonians, by replacing the  $E$  with an  $H$  and including vector notation.

The goal of an EPR experiment performed on a crystal is to characterize a defect (with one or more unpaired spins) by proposing a spin Hamiltonian and determining its parameters. One begins by noting the number of lines in an EPR spectrum and the relative spacing of these lines. This suggests the appropriate  $S$  value and the  $I$  values



representing resolved hyperfine interactions, and thus determines the general form of the spin Hamiltonian for that defect. Next, an angular dependence study of the spectrum is conducted and the results are used as input data for a fitting program that determines the final values of the spin Hamiltonian parameters. After the spin Hamiltonian parameters are determined, a model for the defect is established that is consistent with the crystal structure and these parameters. This will lead to a better understanding of the defect chemistry of the material.

The complete spin Hamiltonian for an EPR experiment can be written as

$$\hat{H} = \hat{H}_{EZ} + \hat{H}_{HF} + \hat{H}_{FS} + \hat{H}_{NZ} + \hat{H}_Q \quad (2.11)$$

where

$$\hat{H}_{EZ} = \mu_B \vec{S} \cdot \vec{g} \cdot \vec{B} \quad \text{electron Zeeman interaction} \quad (2.12)$$

$$\hat{H}_{HF} = \vec{I} \cdot \vec{A} \cdot \vec{S} \quad \text{hyperfine (nuclear-electron spin) interaction} \quad (2.13)$$

$$\hat{H}_{FS} = \vec{S} \cdot \vec{D} \cdot \vec{S} \quad \text{fine structure (electron-electron spin) interaction} \quad (2.14)$$

$$\hat{H}_{NZ} = g_N \mu_N \vec{I} \cdot \vec{B} \quad \text{nuclear Zeeman interaction} \quad (2.15)$$

$$\hat{H}_Q = \vec{I} \cdot \vec{Q} \cdot \vec{I} \quad \text{nuclear electric quadrupole interaction} \quad (2.16)$$

In the above expressions,  $\vec{g}$ ,  $\vec{A}$ , and  $\vec{D}$  are three-dimensional symmetric matrices. Each matrix is described by six parameters, i.e., three principal values and three Euler angles defining the principal axes directions.  $\vec{Q}$  is a traceless three-dimensional symmetric matrix and is described by five parameters.

$H_{EZ}$ , the electron Zeeman term, describes the interaction between the electron spin and the applied magnetic field. This is typically the dominant (largest value) term in a spin Hamiltonian. The electron Zeeman Hamiltonian term can be rewritten as:

$$\hat{H}_{EZ} = \mu_B \vec{S} \cdot \vec{g} \cdot \vec{B} = \beta \vec{B} \cdot (\hat{L} + g_e \hat{S}) + \lambda \hat{L} \cdot \hat{S} \quad (2.17)$$

There are two terms on the right side of Eq. 2.17. The first term represents the energy associated with the separate coupling of the orbital angular momentum  $\hat{L}$  and the spin angular momentum  $\hat{S}$  with the magnetic field, while the second term represents the spin-orbit energy associated with the coupling of  $\hat{L}$  and  $\hat{S}$ . The constant  $\lambda$  is the spin orbit coupling constant. With some mathematical manipulation of Eq. 2.17, the  $\vec{g}$  matrix can be rewritten as

$$\vec{g} = g_e \vec{I} + 2\lambda \vec{\Lambda} \quad (2.18)$$

where  $\vec{I}$  is the identity matrix. If the angular momentum of a system is due solely to spin angular momentum,  $\vec{g}$  should be isotropic with the value  $g_e$ . Any anisotropy in  $\vec{g}$  is due to the presence of orbital angular momentum which couples higher excited states to the ground state. This anisotropy is represented by the  $\vec{\Lambda}$  matrix [25].

$H_{HF}$  is the hyperfine term. It represents the interaction between the electron spin and the nuclear spin. This  $\vec{A}$  matrix can be decomposed into isotropic and anisotropic parts, described by  $\vec{A} = (a\vec{I} + \vec{B})$  where  $a$  is the scalar Fermi contact term and represents the isotropic part of  $\vec{A}$ . The Fermi contact term is the magnetic interaction between the electron and the atomic nucleus when the electron is inside that nucleus. It is proportional to  $|\psi^2|$  evaluated at the nucleus (only  $s$  orbitals contribute to the Fermi contact term). The anisotropic portion of the  $\vec{A}$  matrix corresponds to a dipole-dipole interaction between the electron and nuclear magnetic moments. It is represented by the traceless matrix  $\vec{B}$  and has two hyperfine interaction constants ( $b$  and  $b'$ ). In its principal axis system,  $\vec{B}$  is written as

$$\vec{B} = \begin{pmatrix} -b + b' & 0 & 0 \\ 0 & -b - b' & 0 \\ 0 & 0 & 2b \end{pmatrix}$$

It follows that

$$b = \frac{1}{2}B_{zz} \quad \text{and} \quad b' = \frac{1}{2}(B_{xx} - B_{yy})$$

where  $b'$  describes the deviation from axial symmetry.

The fine structure term,  $H_{FS}$ , in the spin Hamiltonian accounts for interaction between electrons and is present when  $S > 1/2$ . Examples where this term is important include crystal field effects on transition-metal ions, spin triplets, and biradicals. The  $\vec{D}$  matrix is traceless and, in its principal axis system, can be represented by an axially symmetric parameter  $D$  and an asymmetry parameter  $E$ . It can be written as  $H_{FS} = D_{xx}S_x^2 + D_{yy}S_y^2 + D_{zz}S_z^2$  and expressed in matrix form as

$$\vec{D} = \begin{pmatrix} D_{xx} & 0 & 0 \\ 0 & D_{yy} & 0 \\ 0 & 0 & D_{zz} \end{pmatrix} = \begin{pmatrix} -\frac{1}{3}D + E & 0 & 0 \\ 0 & -\frac{1}{3}D - E & 0 \\ 0 & 0 & \frac{2}{3}D \end{pmatrix}$$

This dissertation does not describe an experiment where a fine-structure matrix was needed in the spin Hamiltonian.

The nuclear Zeeman term,  $H_{NZ}$ , occurs for nuclei with  $I \neq 0$ . This term is the same as the electron Zeeman term, except that now it is the nuclear spin interacting with a magnetic field. This energy, even though it is small, needs to be accounted for in the spin Hamiltonian. It is especially important in ENDOR experiments.

The nuclear electric quadrupole interaction,  $H_Q$ , is the interaction of a nucleus with the electric field gradient at the nucleus. When a nucleus with  $I > 1/2$  interacts with an

electric field gradient, the nuclear spin levels are no longer equally spaced in energy. This unequal spacing of the energy levels is clearly seen in ENDOR spectra. The nuclear electric quadrupole term is represented by the coupling matrix  $\vec{Q}$  (which is traceless) and contains the product of the nuclear electric quadrupole moment and the gradient of the electric field at the nucleus due to the surrounding electrons. For a symmetric charge distribution such as in a cubic crystal, the electric field gradient is zero at the “regular” lattice sites. However, if either the overall symmetry of the lattice or the local symmetry of the point defect is lower, then the electric field gradient may be nonzero. The quadrupole coupling parameters are then a measure of the relative distribution of the surrounding electric charge [24]. The nuclear electric quadrupole term can have a significant impact in ENDOR spectra. The effect of the quadrupole term will be demonstrated in Chapter 3 where boron nuclei interact with an  $S = 1/2$  trapped hole center.

## **2.7. EPR and ENDOR Instrumentation**

The EPR and ENDOR spectra presented in this dissertation were taken with an X-band EMX Bruker spectrometer and a Bruker ESP 300 spectrometer (used primarily for ENDOR). Bruker, a German company, is the primary manufacturer of versatile and sensitive EPR and ENDOR spectrometers in the world. Both systems are EPR units with a single computer control interface. For low temperatures, an Oxford Instruments helium-gas flow system was used to maintain the samples at selected temperatures in the 4 – 200 K range.

Three types of resonant cavities were used with the EPR spectrometers. The EMX spectrometer uses either a standard rectangular TE<sub>102</sub> cavity or a high sensitivity TE<sub>011</sub> cylindrical cavity while the Bruker ESP 300 uses a cylindrical TE<sub>011</sub> ENDOR cavity. The sharpness of response of any resonant system is commonly described by a factor of merit, universally represented by the symbol Q. Q is defined as

$$Q = \frac{2\pi (\text{maximum microwave energy stored in the resonator})}{\text{energy dissipated per microwave cycle}} \quad (2.19)$$

A more practical “working” definition of the Q factor is given by

$$Q = \frac{\nu}{\Delta\nu} \quad (2.20)$$

where  $\nu$  is the resonant frequency of the cavity and  $\Delta\nu$  is the full width at half maximum of the resonant peak. The standard rectangular cavity for the EPR system and the ENDOR cavity both have Q values between 2000 and 5000. The high sensitivity cavity has a Q value greater than 12,500. A higher Q value corresponds to a better signal-to-noise ratio. Metal and water, including water vapor, are some examples of materials that will drastically reduce the Q of the cavity. For this reason, nitrogen gas continually flows through the cavity during low temperature operation to prevent moisture buildup on the surface of the glassware within the cavity. The cylindrical ENDOR cavity is less sensitive because it contains the metal coil that produces the radio waves needed to induce the ENDOR transitions. This metal coil is attached to the cold temperature glassware within the cavity. The cavities are also designed such that the microwave magnetic field is a maximum and the microwave electric field is a minimum at the sample position.

## 2.8. Optical Absorption Spectroscopy

Optical absorption is another spectroscopic technique used to characterize point defects in crystals. Photons with energy  $E = h\nu = \frac{hc}{\lambda}$  are absorbed by the point defects, i.e., transitions occur from the ground state to one or more excited states. The electronic structure of the defect (and the crystal) determines the possible absorption transitions. Because the electronic energy levels in matter are quantized and there is a forbidden energy band in semiconductors and insulators, only specific photon energies are absorbed. When energy is absorbed by an atomic scale defect, it is excited to a higher electronic state. The defect emits its absorbed energy and returns to the ground state. There are two types of emission processes, radiative and non-radiative. Radiative emissions occur when the defect emits a photon and nonradiative occurs when the defect emits one or more phonons to the surrounding lattice. These photons and phonons have discrete values of energy that are controlled by the electronic structure of the defect and the surrounding lattice. The principles of absorption and emission are best described by the Franck-Condon principle with the help of a configuration-coordinate energy diagram, illustrated in Fig. 2.6.

For a given electronic state of a point defect, the surrounding ions have an equilibrium configuration, i.e., this is the positions of the ions that corresponds to a minimum energy for the defect. There will be one equilibrium configuration when the defect is in its electronic ground state and a different equilibrium configuration when it is in an excited electronic state. For this reason, the horizontal axis of Fig. 2.6 is labeled “nuclear configuration” and is often referred to as the configuration coordinate  $Q$ . The parabolic curves represent the potential wells of the electronic ground state ( $S_0$ ) and the

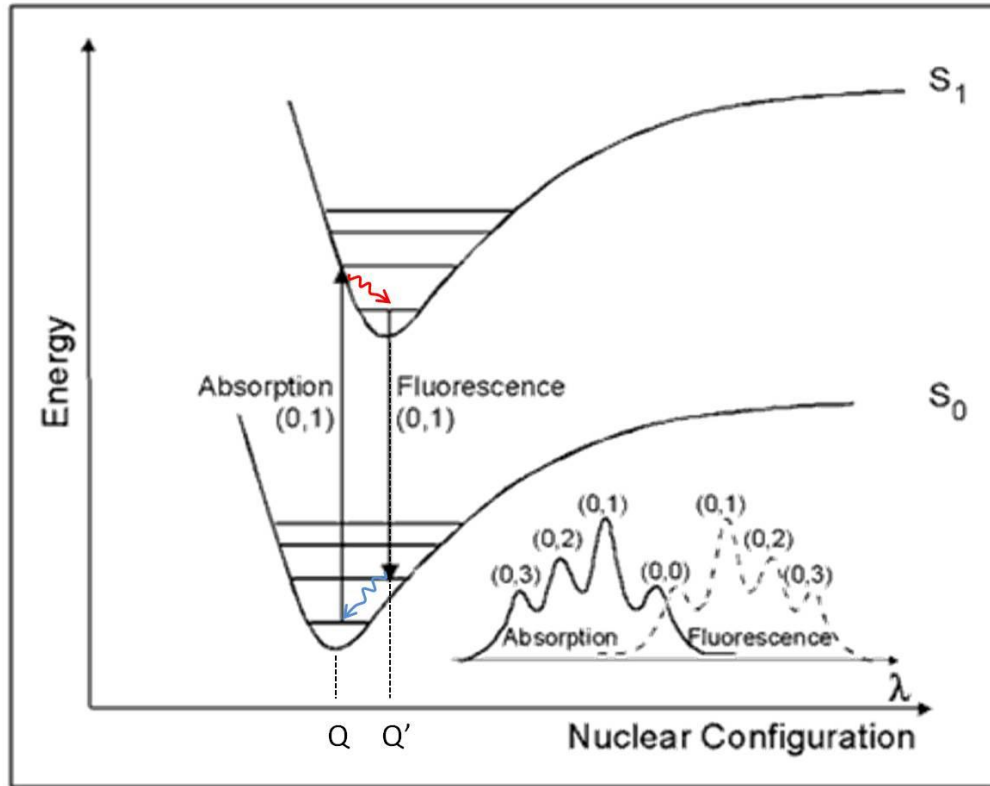


Figure 2.6. Configuration-coordinate energy diagram.

first excited state ( $S_1$ ) while the horizontal lines in the wells represent the discrete vibrational modes of the structure. The Franck-Condon principle states that the change in the electronic structure of the defect occurs very quickly, before the surrounding ions have a chance to adjust to their new equilibrium positions. This is shown by the vertical arrow in Fig. 2.6 labeled Absorption (0,1). The (0,1) label on the vertical arrow indicates that the electron goes from the lowest vibrational mode ( $n = 0$ ) in the ground state to the second vibrational mode ( $n = 1$ ) in the excited state. After this upward electronic transition (absorption), the defect will release its added energy in three steps. First, the surrounding ions shift to their new equilibrium configuration and lower the energy of the defect by emitting a phonon (shown with a red arrow in Fig. 2.6). Then, following the

Franck-Condon principle, the defect emits a photon (fluorescence) as it returns to the ground state. As it reaches the ground state, the surrounding ionic configuration still corresponds to the excited state equilibrium configuration. Finally, the ionic configuration returns to the original ground state equilibrium configuration by emitting a phonon (shown with a blue arrow in Fig. 2.6).

Absorption measurements provide useful information about the electronic structure of the defect and often can be correlated with EPR measurements, as will be seen later in this dissertation for LTB samples doped with silver. A Varian-Cary spectrophotometer was used to measure room temperature optical absorption in both undoped and doped LTB crystals. Absorption measurements were also conducted on pre- and post-x-ray irradiated LTB crystals. The optical absorption data presented in this dissertation was obtained by passing electromagnetic radiation, with wavelengths from the near ultraviolet to the near infrared region, through the crystal and thus exciting transitions between electronic states.

A diagram that is similar to the spectrophotometer used for the present study is shown in Fig. 2.7. The spectrometer contains two light sources, one for wavelengths between 190 and 350 nm and one for wavelengths between 350 nm and 3.2  $\mu\text{m}$ . Light passes through a monochromator that selects the wavelength range for which absorption is to be measured. The monochromator contains a diffraction grating that disperses the light into individual wavelengths. The grating allows only a narrow range of wavelengths to pass through a slit and into the sample chamber. A chopper causes the beam to alternately pass through the sample and reference areas. Both beams are then incident on the detector. Two detectors are used, a photomultiplier tube for wavelengths



from 190 to 850 nm and a semiconducting PbS cell for wavelengths from 850 nm to 3.2  $\mu\text{m}$ . The detector is used to compare the intensities of the alternating beams and produces an output signal proportional to their difference. This signal, obtained as a function of wavelength, represents the absorbed light. The output can be displayed as either a transmission curve or an absorption curve.

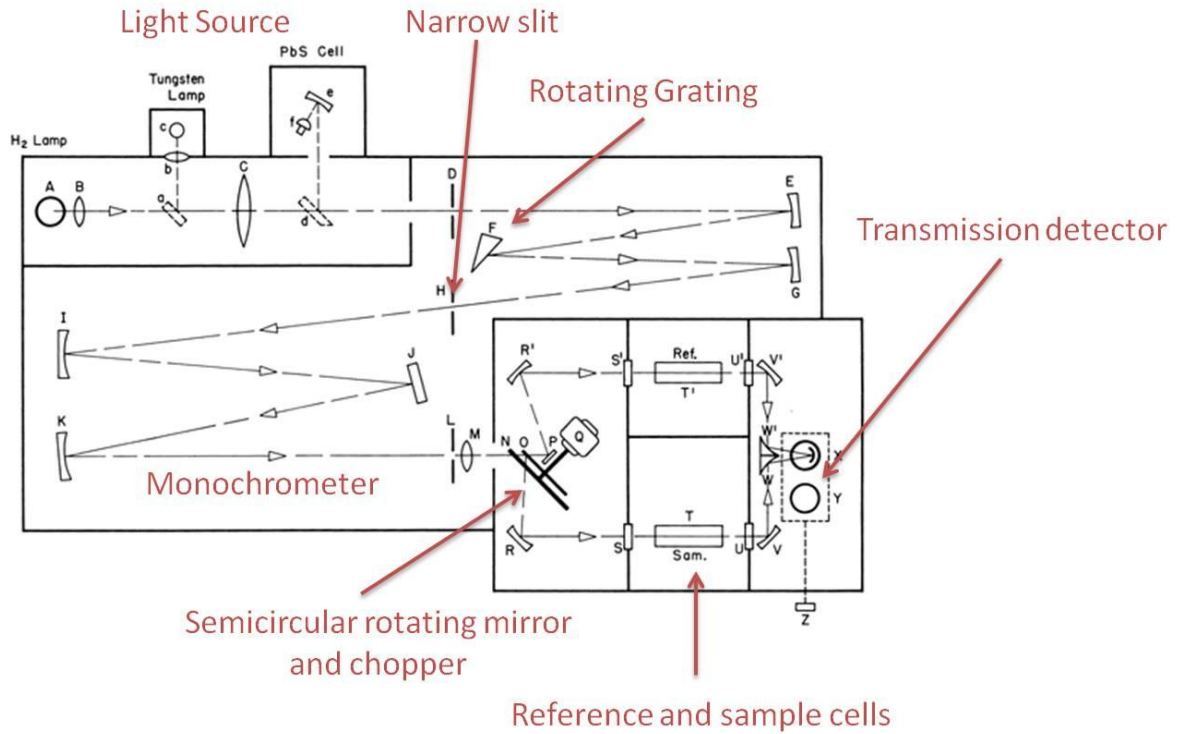


Figure 2.7. Diagram of a spectrophotometer.

Optical absorption spectra are often plotted as optical density (or absorbance) versus wavelength. Optical density (OD) is defined as

$$\text{OD} = -\log_{10} \left( \frac{I}{I_0} \right) \quad (2.21)$$

where  $I_0$  is the incident light intensity and  $I$  is the transmitted light intensity. The Lambert-Beer law (Eq. 2.22) relates  $I$  and  $I_0$  to the absorption coefficient  $\alpha$  and the optical path length  $x$  in the sample.

$$I = I_0 e^{-\alpha x} \quad (2.22)$$

Combining Eqs. 2.21 and 2.22 gives the following expression for the absorption coefficient, shown in Eq. 2.23.

$$\alpha = \frac{OD}{x \log(e)} \quad (2.23)$$

Absorption, fluorescence spectroscopy, and EPR are combined to show that  $\text{Ag}^{2+}$  ions are responsible for an optical absorption peak found in x-ray irradiated LTB crystals.

## 2.9. Fluorescence Spectroscopy

Fluorescence spectroscopy is a similar technique to that of absorption described in Section 2.8 with the exception that a fluorescent spectrometer, or fluorospectrometer, can measure and monitor specific absorptions and emissions. This is accomplished using two different optical monochromators, one specifically for each function of emission or excitation. The instrument, illustrated in Fig. 2.8, produces output that is given as intensity (photomultiplier tube counts) versus wavelength. The spectrometer used in this dissertation is a Fluorolog -3 fluorospectrometer manufactured by the Horiba Scientific Corporation.

The Fluorolog-3 uses a xenon high voltage lamp as the light source. The light then passes through a narrow slit into the excitation monochromator. In the excitation monochromator, the light is separated into individual wavelengths using two sets of mirrors and two diffraction gratings to provide a narrow band of wavelengths to the

sample. There are two slits in the excitation monochromator that can be used to adjust the resolution of the exciting light, from 1 to 14 nm. After passing through the final slit of the excitation monochromator, light is incident on the sample. The sample holder used in this dissertation

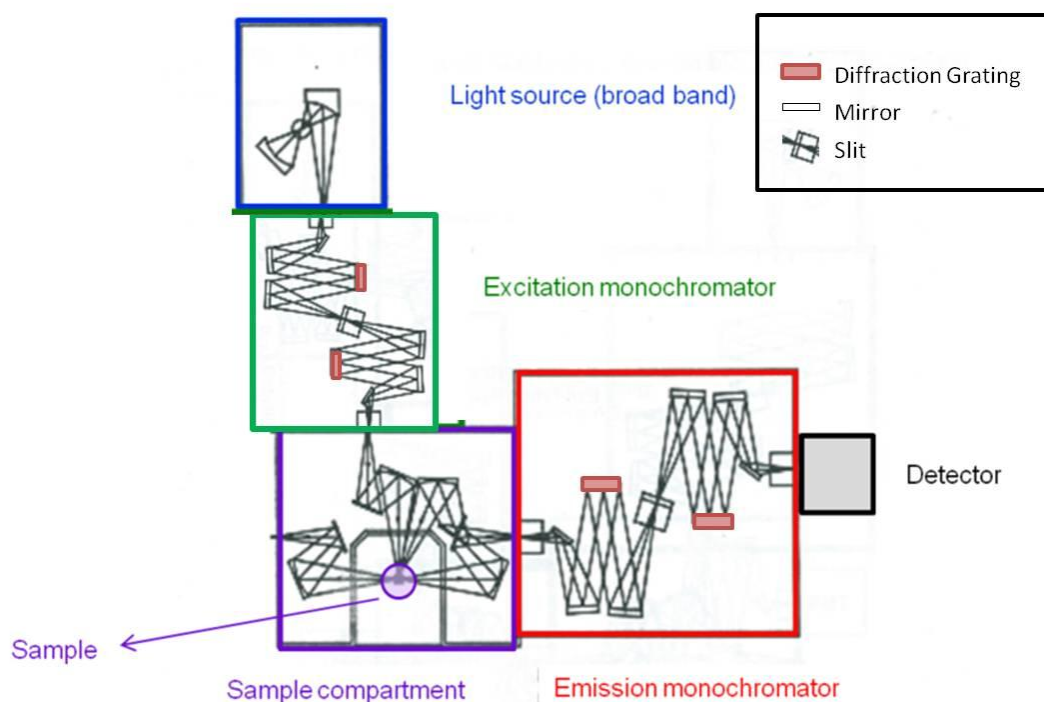


Figure 2.8. Diagram of a fluorescence spectrometer (also referred to as a fluorolog).

was attached to an movable stage such that the beam could be focused to a small spot size on the sample. Once light reaches the sample, a portion will be reflected and a portion will be absorbed and then emitted as fluorescent light. The emitted light, and any scattered light, passes through the emission monochromator and is collected at the detector, i.e., a photomultiplier tube in the case of the Fluorolog-3 instrument. The emission monochromator also has two diffraction gratings and two controlled slits.

A computer is used to control the wavelength settings for both monochromators as well as the slit resolutions. The Fluorolog can be set up to run either an excitation or emission experiment. In excitation, the emission monochromator can be set to monitor a specific wavelength. Conversely, in emission, the excitation monochromator is set to provide a specific wavelength. Normally, a series of intensity vs emission spectra are taken at different excitation wavelengths in order to find the optimum excitation wavelength for a particular emission peak. Excitation spectra tend to be slightly narrower bands while emission curves tend to be broader due to phonon interaction. The broadening of the emission and excitation bands can be described by the Huang-Rhys factor [26], but is not discussed in this dissertation.

While an absorption spectrometer provides data that does not need correction, there are several corrections that must be made in data taken with a fluorospectrometer. First, the intensity of the light provided by the xenon lamp varies with wavelength. The data collected at the photomultiplier tube must be adjusted for a constant photon flux. Second, the photomultiplier tube has a nonconstant response to wavelength as well. Both of these adjustments may cause shifts in peak positions and intensities of the acquired spectra.

### **III. Characterization of the Intrinsic Hole Center in Lithium Tetraborate**

#### **3.1. Introduction**

Point defects have been widely studied in various oxide materials [27-30]. Depending on their effective charge relative to the lattice, these defects may either trap electrons or holes when a crystal is exposed to ionizing radiation. Examples of common point defects in oxides are anion vacancies, cation vacancies, and substitutional transition-metal impurities. Optical spectroscopy, electron paramagnetic resonance (EPR), and electron-nuclear double resonance (ENDOR) are often used to study these point defects.

Previous research at the Air Force Institute of Technology investigated intrinsic point defects in nominally undoped single crystals of lithium tetraborate (LTB) [31]. EPR was used to identify oxygen and lithium vacancies as the primary point defects in the as-grown LTB crystals. To be observed in EPR experiments, the defects need to be in a paramagnetic charge state. In the case of LTB, this is accomplished by placing the crystal in liquid nitrogen, thus cooling the crystal to 77 K, and then while in liquid nitrogen, irradiating the crystal with x rays (60 kV and 30 mA) produced by a high-flux x-ray tube. Energy provided by the x rays moves electrons from the valence band to the conduction band and results in the creation of electron-hole pairs. Many of these electrons and holes recombine immediately, while others move separately through the lattice and become “trapped” at defects. Defects that trap electrons are referred to as electron centers and defects that trap holes are referred to as hole centers. Trapped electron centers have gained electrons from the lattice and trapped hole centers have thus

lost electrons. The concentration of these two types of defects must balance to maintain charge neutrality. These electron and hole centers form at different locations in the crystal. In LTB, the electrons are trapped at oxygen vacancies and the holes are trapped near lithium vacancies. Following an irradiation at 77 K, these trapped electron and hole centers are stable as long as the sample remains below ~90 K. Above ~90 K, the electrons and holes recombine and the crystal returns to its non-paramagnetic charge state. The present chapter describes an in-depth EPR and ENDOR study of the intrinsic trapped hole center in undoped LTB crystals.

### **3.2. Thermoluminescence Results**

A thermoluminescence (TL) experiment was performed to establish the thermal stability of the intrinsic trapped hole center in LTB. Though there is considerable literature describing thermoluminescence from lithium tetraborate crystals containing various dopants [32-34], thermoluminescence from undoped lithium tetraborate at low temperatures has not been reported. Figure 3.1 is a TL glow curve obtained from an undoped LTB crystal. These data were acquired from a 77 K irradiated crystal that was quickly removed from liquid nitrogen and placed at the end of an optical fiber. As the crystal rapidly warmed to room temperature, light was collected through the optical fiber and passed into an optical spectrometer. Temperatures were determined by assuming a linear heating rate. The sample was at 77 K immediately upon placement at the end of the fiber, then a timer was started, and the elapsed time was noted when the crystal reached 273 K (the moment when frost converted to moisture on the crystal surface). The horizontal axis of Fig. 3.1 reflects this time-to-temperature conversion. The strong

peak just above 100 K agrees with the 90 K EPR results reported by Swinney et al. [31]. The heating rate used in the TL experiment was much faster (13 K/s) than the heating rate ( $< 1$  K/s) used in the EPR experiment, thus explaining why the TL peak occurs at a slightly higher temperature. The glow from the crystal was intense enough to be observed with the naked eye. The emission at 100 K in the TL curve is assigned to electron-hole recombination, where the participating hole is the subject of the present chapter.

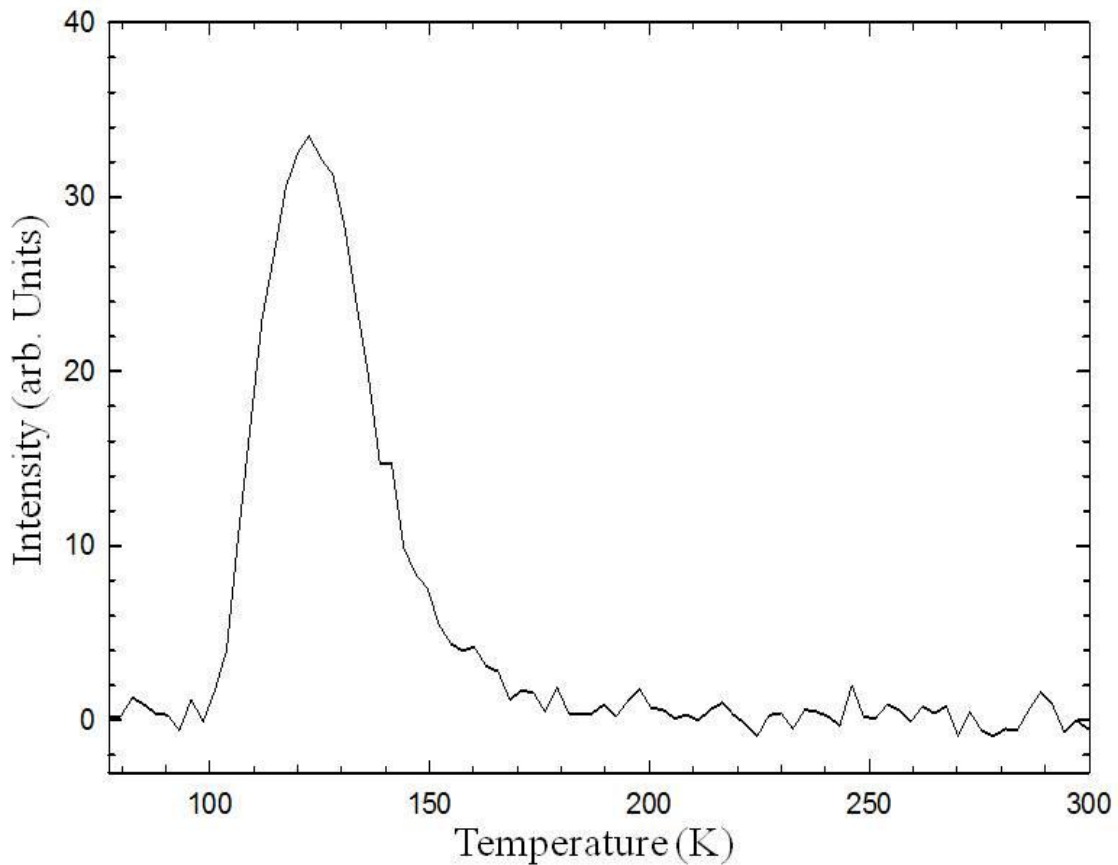


Fig. 3.1. TL glow curve of an LTB crystal irradiated with x rays at 77 K.

### 3.3. Electron Paramagnetic Resonance Results

In the earlier study by Swinney et al. [31], the intrinsic paramagnetic electron and hole centers were shown to have  $g$  values near 2.0, hence the EPR spectra of the x-ray induced defects overlap. The  $g$  shifts associated with these two defects are relatively small and all directions of magnetic field have overlapping electron and hole center spectra. With the magnetic field parallel to the  $c$  axis of the crystal, or [001] direction, the electron center has a spectrum that extends over 400 Gauss and is centered at  $g = 2.0049$  while the hole center extends over 45 Gauss and is centered at  $g = 2.0116$ . By acquiring the hole center spectrum at 40 K, instead of the typical 25 K used for the electron center, microwave power saturation effects are reduced and the well-resolved structures that are associated with the hole center can be clearly seen. In practice, the hole center spectrum obscures a portion of the electron center spectrum. Figure 3.2 shows the EPR spectrum of the intrinsic hole center in LTB. The three traces in Fig. 3.2 were taken with the magnetic field parallel to the [001], [100], and [110] directions, respectively, in the crystal.

The seven line spectrum observed in Fig. 3.2(a) is representative of an  $S = 1/2$  spin interacting with two  $^{11}\text{B}$  nuclei where each has a nuclear spin of  $I = 3/2$ . The energy level diagram in Fig. 3.3 explains the EPR spectrum (shown in Fig. 3.2(a)) taken when the  $c$  axis of the crystal is aligned parallel to the magnetic field. The hole has a spin of  $S = 1/2$ . In a magnetic field, this spin degeneracy is lifted and creates  $m_s = +1/2$  and  $m_s = -1/2$  energy levels. One boron atom with a nuclear spin of  $I = 3/2$  causes each of these levels to split into four. These levels are labeled  $m_I(1)$  in Fig. 3.2. Next, each  $m_I(1)$  level is split into four by a second boron atom, again with  $I = 3/2$ . This results in 16 levels



associated with  $m_s = +1/2$  and 16 levels associated with  $m_s = -1/2$ . These 32 levels are labeled as  $m_l(2)$ . The 16 total energy levels possible for each  $m_s$  are displayed in Fig. 3.3 in the section describing the second boron interaction. As an aid to understanding Fig. 3.3, the reader can follow across the  $m_s = +1/2$  portion of the diagram. On the left side, find  $m_l(1) = 3/2$  underlined in blue and then look at the four blue lines just to the

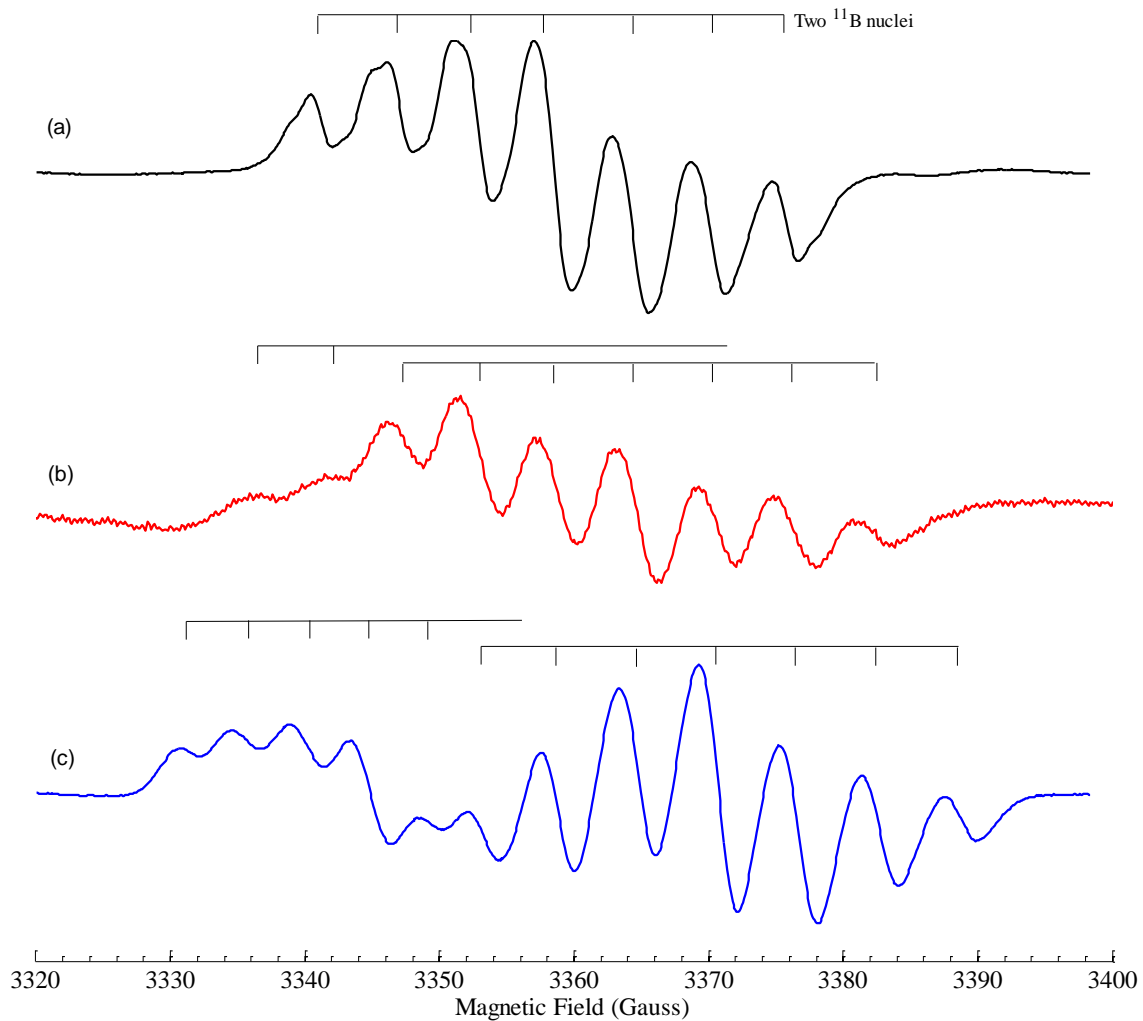


Figure 3.2. EPR spectrum of the intrinsic trapped hole center in an  $\text{Li}_2\text{B}_4\text{O}_7$  crystal. Stick diagrams show the  $^{11}\text{B}$  hyperfine lines. (a) Magnetic field along the [001] direction. (b) Magnetic field along the [100] direction. (c) Magnetic field along the [110] direction.

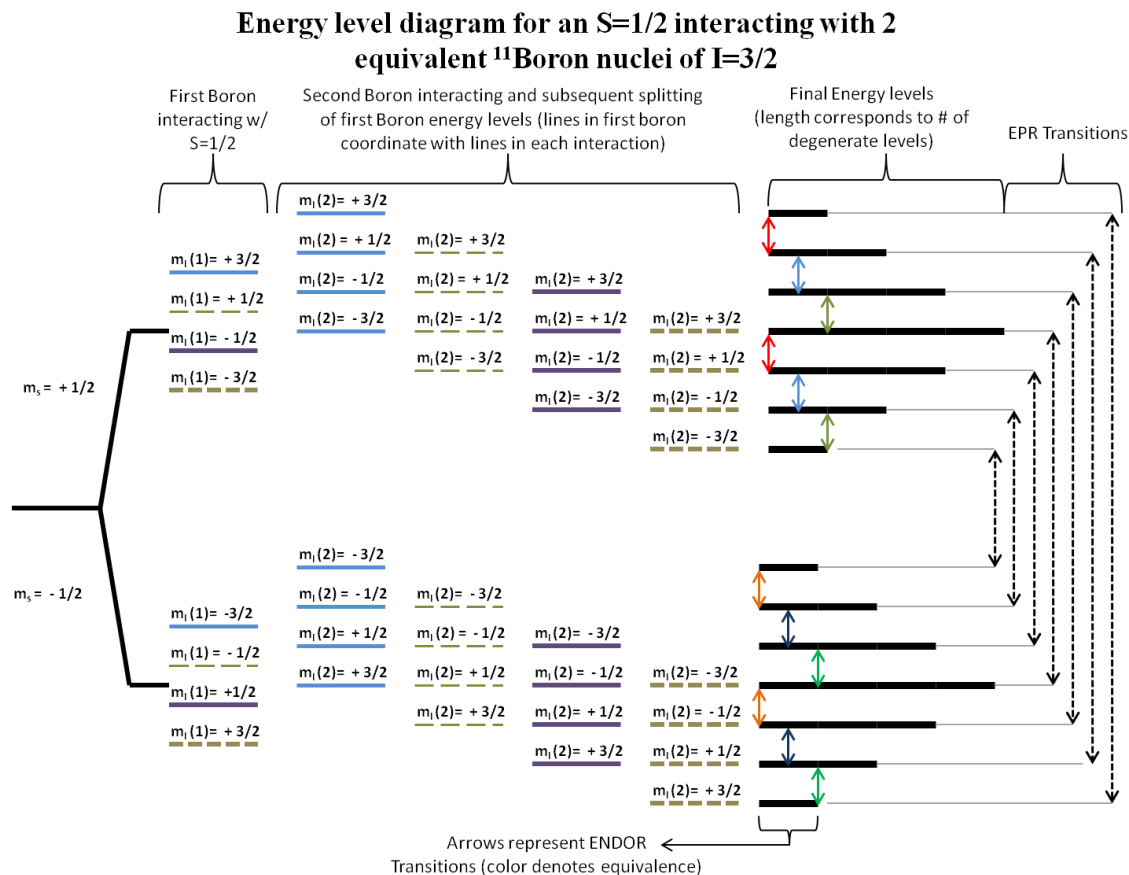


Figure 3.3. Energy level diagram for an electron spin  $S = 1/2$  interacting with two equivalent  $^{11}\text{B}$  nuclei of spin  $I = 3/2$ .

right in the “Second boron interacting...” portion. These four levels represent the only energies that are possible when  $m_s = +1/2$  and  $m_I(1) = +3/2$ . These levels are labeled using the scheme  $E(m_s, m_I(1), m_I(2))$ .

$$E(+1/2, +3/2, +3/2)$$

$$E(+1/2, +3/2, +1/2)$$

$$E(+1/2, +3/2, -1/2)$$

$$E(+1/2, +3/2, -3/2)$$

Notice that many of the levels in Fig. 3.3 are degenerate with each other. For example,  $E(+1/2, +3/2, -1/2)$ ,  $E(+1/2, +1/2, +1/2)$ , and  $E(+1/2, -1/2, +3/2)$  have the same energy,

while  $E(+1/2, +3/2, +3/2)$  is not degenerate with any other levels. Following across to the right side of Fig. 3.3, the final energy levels are drawn using line lengths that correspond to the degree of degeneracy for each level. Looking down on the “Final Energy Levels” portion corresponding to  $m_s = +1/2$ , the bar length pattern of 1, 2, 3, 4, 3, 2, 1 in terms of degeneracy can be seen. This is the vertical intensity pattern observed in Fig. 3.2(a). Recalling that the selection rules for EPR transitions are  $\Delta m_s = \pm 1$  and  $\Delta m_I = 0$ , the dashed arrows on the right side of Fig. 3.3 correspond to the possible EPR transitions, of which there are seven. The small arrows between the final energy levels correspond to ENDOR transitions where  $\Delta m_s = 0$  and  $\Delta m_I = \pm 1$ .

Although it is not shown, the final energy levels on the right side of Fig. 3.3 are not equally separated in energy. The  $^{11}\text{B}$  nucleus has a nuclear electric quadrupole moment and this causes small but measurable changes in the separations of the energy levels within the  $m_s = +1/2$  and  $m_s = -1/2$  sets. The arrows in this figure are color coded to show which transitions have the same energy differences. Consider the  $m_s = +1/2$  energy level portion of the figure. There are six energy levels, but there are only three distinct energy differences between levels, i.e., the red, blue, and green arrows. Because of this nuclear electric quadrupole interaction, an ENDOR spectrum would show three transitions associated with  $m_s = +1/2$ . The sets of three ENDOR lines are shown in the ENDOR spectra discussed later in this chapter. These sets of three ENDOR lines also emerge from the analysis of the complete spin Hamiltonian. Equivalent hyperfine and quadrupole matrices for the two boron nuclei interacting with the unpaired electron, i.e., the hole, cause the sets of three lines. If the two boron nuclei did not have equivalent matrices, there would be six different energy separations, and thus six discrete ENDOR

transitions. This behavior is very useful in determining a defect model. In a practical sense, it is useful when aligning the magnetic field to be in particular crystal planes so that useful EPR and ENDOR data could be collected and interpreted.

In order to understand the spectra presented in Fig. 3.2, the crystal structure of lithium tetraborate must be discussed. The basic building block in LTB is a  $(\text{B}_4\text{O}_9)^{6-}$  unit. Each of these units is surrounded by 6  $\text{Li}^+$  ions, thus maintaining charge neutrality. These  $(\text{B}_4\text{O}_9)^{6-}$  units are stacked and rotated by  $90^\circ$  about the  $c$  axis of the crystal to give four crystallographically equivalent orientations of the basic unit. The units do not sit directly above and below each other because they rotate along a screw axis. A screw axis is a rotation followed by a translation along the direction of the axis. The four  $(\text{B}_4\text{O}_9)^{6-}$  units can be seen in Fig. 3.4(a) where the lithium atoms have been removed for better viewing. Notice that the four  $(\text{B}_4\text{O}_9)^{6-}$  units are identical other than rotation. The change in size demonstrates the relative depths of the  $(\text{B}_4\text{O}_9)^{6-}$  units. All other  $(\text{B}_4\text{O}_9)^{6-}$  units in the crystal will be crystallographically equivalent to one of these four or will be mirror images of these four (this makes a total of eight distinguishable units). A defect can be located in any of these crystallographically equivalent units. A defect, therefore, has eight possible orientations of the principal axes directions associated with its  $g$  matrix and hyperfine matrices. These eight orientations, or “sites,” can often be resolved in an EPR experiment. For the remainder of this dissertation, “sites” will be used to refer to crystallographically equivalent orientations of a defect, thus there are eight sites in LTB for any given defect.

When the magnetic field is parallel to the  $c$  axis of an LTB crystal, all eight of the crystallographically equivalent sites of a defect are magnetically equivalent. The EPR

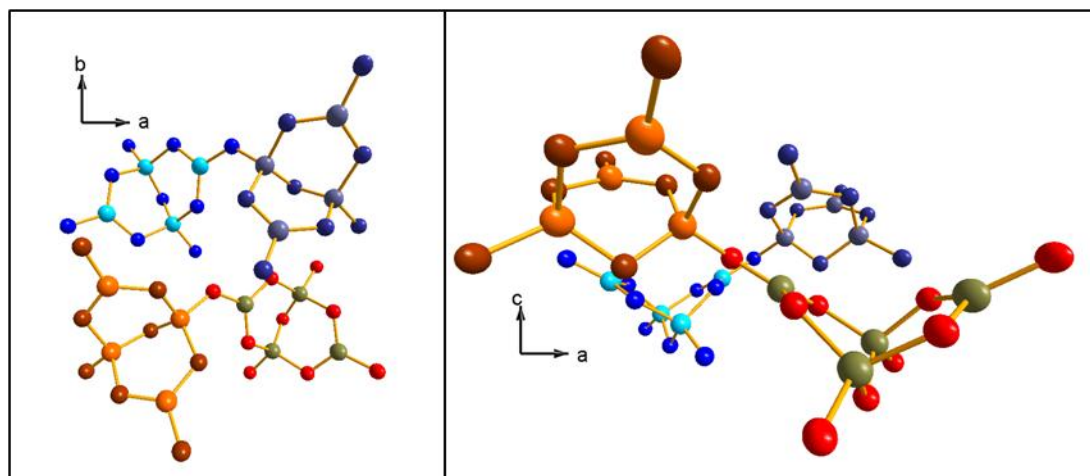


Figure 3.4. Four  $(\text{B}_4\text{O}_9)^{6-}$  units comprising the LTB crystal lattice. (a) when viewed along the  $c$  axis and (b) when viewed looking along the  $a$  axis.

spectrum in Fig. 3.2(a) represents this case where the intrinsic trapped hole center has the simplest spectrum, consisting of seven lines, because all of the sites are magnetically equivalent. In contrast, when the magnetic field is parallel to the  $a$  axis of the crystal, the eight crystallographically equivalent sites divide into two distinct groups of magnetically equivalent sites. Figure 3.4(b), viewed along the  $a$  axis, shows four  $(\text{B}_4\text{O}_9)^{6-}$  units. Each of these four also has a mirror to make a total of eight. The upper two sites in Fig 3.4(b) are magnetically equivalent, as are the lower two sites. The equivalent sites are mirror images of each other. When EPR is performed with the magnetic field parallel to the crystal  $a$  axis, there will be two sets of EPR lines in the spectrum. This behavior is illustrated in Fig. 3.2(b). A full seven peak set of lines similar to Fig. 3.2(a) can be seen on the right side of Fig. 3.2(b), extending from 3348 to 3384 G. A second set of seven lines underlay the larger initial set of seven lines and has two components that extend to lower magnetic field, at 3336 and 3342 G. This is shown in the stick diagram above the spectrum in Fig. 3.2(b). Thus, when the magnetic field is along the  $a$  axis, the two sets of

lines representing the two magnetically inequivalent sites are very similar, yet distinguishable, in the EPR spectrum.

The farthest apart that the sets of lines ever move from each other is shown in Fig. 3.2(c) and was taken with the magnetic field parallel to the [110] crystal direction. The fully visible spectrum on the right has a  $g$  value of 2.005 and the mostly visible spectrum on the left has a  $g$  value very close to 2.020. The  $g$  value for the left set of lines is an estimate of where the center of the spectrum occurs, since the complete seven-line spectrum is not observed. The average  $g$  value of the two sets of lines is 2.0125, and this is also the value of  $g$  along the  $c$  axis and the average of the two spectra observed when the field is parallel to the  $a$  axis. The EPR spectra of the intrinsic trapped hole center never shift far from this 2.0125  $g$  value. This lack of angular dependence means that the  $g$  matrix for this defect is nearly isotropic.

During the characterization of the intrinsic trapped hole center, it was impossible to observe more than one complete seven line set with EPR. This meant that an exact  $g$  matrix could not be determined from the experimental data. In the spin Hamiltonian, the  $g$  matrix is described by three principal values,  $g_x$ ,  $g_y$ ,  $g_z$ , and three Euler angles that specify the directions of the principal axes relative to the crystal axes. Each observed seven-line set can be used as a single data point in fitting the  $g$  matrix. Thus, six independent seven line sets are required to determine the complete  $g$  matrix. Only four independent seven-line sets could be obtained for the intrinsic trapped hole center, when the magnetic field was parallel to the [001], [100], [110], and [101] crystal directions. Data taken with the field parallel to the [010] crystal direction does not help since it is equivalent to data taken when the field is parallel to the [100] crystal direction in this

tetragonal crystal. Additional independent sets of lines from other orientations of the magnetic field would have provided the extra data points needed for a complete determination of the  $g$  matrix.

Although an experimental  $g$  matrix could not be precisely determined, it is still possible to identify the EPR spectrum as “holelike”. The individual  $g$  values that were obtained from the data in Fig. 3.2 ranged from 2.0050 to 2.0125. In a simple ionic picture (which ignores the high degree of covalency within the borate units in  $\text{Li}_2\text{B}_4\text{O}_7$ ), the  $\text{O}^-$  ion that contains the hole would have a  $2p^5$  electron configuration ( $2p_x^2, 2p_y^2, 2p_z^1$ ) with  $L=1, S=1/2$ . The threefold orbital degeneracy of this  $^2P$  state of the  $\text{O}^-$  ion is then removed by the crystalline electric field. In ascending order, the three energy levels would be  $E_1, E_2$ , and  $E_3$ . Shifts of the principal values from the free-spin value ( $g_e = 2.0023$ ) are caused by spin-orbit interactions that admix excited states to the ground state. This very simple analysis (based on the ionic picture) predicts the following  $g$  values.

$$g_1 = g_e \quad (3.1)$$

$$g_2 = g_e - \frac{2\lambda}{E_3 - E_1} \quad (3.2)$$

$$g_3 = g_e - \frac{2\lambda}{E_2 - E_1} \quad (3.3)$$

The spin orbit coupling constant,  $\lambda$ , for the  $\text{O}^-$  ion is approximately  $-135 \text{ cm}^{-1}$ . Equations 3.2 and 3.3 predict positive shifts in  $g$  from the free-spin value for the  $\text{O}^-$  ion. In general, a hole trapped on an oxygen ion has  $g$  values that vary from 2.003 to 2.050 [35-38].

These theoretical predictions are consistent with the estimated range of experimental  $g$  values (2.0050 to 2.0125), thus verifying that the EPR spectra in Fig. 3.2 are representative of a trapped hole.

### 3.4. Electron-Nuclear Double Resonance Results

This investigation of the intrinsic trapped hole center in LTB will proceed with the assumption of an isotropic  $g$  matrix (in other words, the small differences predicted in Eqs. 3.1, 3.2, and 3.3 will be disregarded and an averaged value will be used). This is not a severe limitation in the analysis of the ground state electronic structure of the trapped hole center. The hyperfine and nuclear electric quadrupole splittings that are observed in ENDOR spectra do not depend on the  $g$  matrix. With this qualification, focus is now shifted to determining values for the hyperfine and quadrupole parameters.

In order to solve the spin Hamiltonian for the hyperfine ( $A$ ) and nuclear electric quadrupole ( $Q$ ) matrices, ENDOR data had to be acquired. To completely specify the  $A$  and  $Q$  matrices, a minimum of six independent data sets are needed. Independent sets of data were collected on different days. Included were sets of data taken with the magnetic field parallel to several high-symmetry directions of the crystal:  $[001]$ ,  $[100]$ ,  $[110]$ , and  $[101]$ . These data sets alone yielded enough spectra for a least squares fitting routine to be used to determine the  $A$  and  $Q$  matrices in the spin Hamiltonian. Additional data were taken at angles within two of the crystal planes to increase the accuracy of the least squares fit and verify the results of the fitting.

In the ENDOR experiment, each orientation of the defect in the crystal will produce a spectrum that consists of six peaks. These six peaks are divided into two sets of three, or triplets. One set, shown in Fig. 3.5, consists of triplets located at higher frequencies. The second set appears at lower frequencies near 4-8 MHz. The lower frequency set is not shown nor was it used to fit the spin Hamiltonian. The lower frequency ENDOR spectra overlap other spectra that appear at lower frequencies. These



overlapping spectra include lines due to the nuclear free spins of lithium and boron. Since each defect site produces a triplet, one would expect to see all four sites line up when the magnetic field is parallel to the  $c$  axis of the crystal and there to be two sets of triplets when the magnetic field is aligned parallel to the  $a$  axis. This is shown by the top and bottom spectra in Fig. 3.5. The top spectrum has two sets of triplets and, though the sets labeled sites 1 and 4 have small intensities, their positions could be clearly identified. The remaining spectra in Fig. 3.5 demonstrate the angular dependence of the site positions in the crystal as the direction of the magnetic field is varied. The site assignments are not made at the time of data collection but occur during the fitting process.

The spacing within the triplets is the result of nuclear electric quadrupole splitting. Looking at one of these triplets, the two outer peaks are separated from the center peak by twice the effective quadrupole coupling parameter for that angle. This will be further discussed later in this chapter. In Fig. 3.5, there are instances where the three quadrupole components are not resolved, i.e., a single line is observed instead of a triplet. For example, site 1 in the spectrum labeled “ $c$  axis + 80 deg toward  $a$  axis” has one line instead of three lines. A single peak will occur when the effective quadrupole moment is zero. At values close to zero, the triplet will appear as a single broad peak. This occurs when the linewidths are larger than the separation between lines. This can be seen when following Site 2 in Fig. 3.5 from 20 to 60 degrees from the  $c$  axis toward the  $a$  axis. During the initial collection of data, this single large peak was puzzling as it was not yet understood that it was actually three peaks on top of each other.

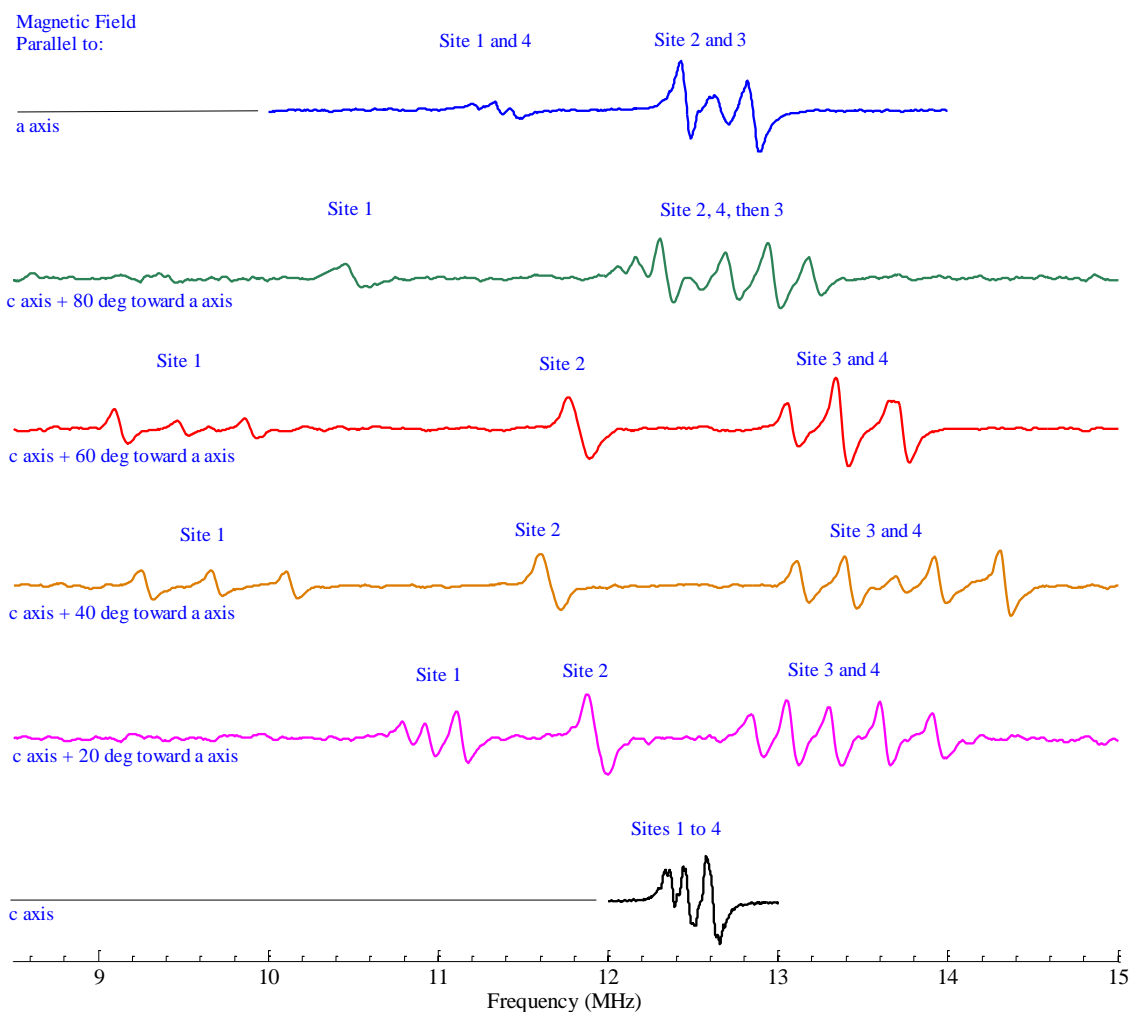


Figure 3.5. ENDOR spectra collected as the magnetic field was rotated from the *c* axis to the *a* axis in 20 degree increments. These spectra are best viewed starting from the bottom where all four crystal sites are equivalent and yield a single spectrum.

### 3.5. Spin Hamiltonian

Swinney et al. [31] suggested that the low temperature trapped hole center in LTB consisted of a hole with spin  $S = 1/2$  on an oxygen ion and has “slightly” inequivalent hyperfine interactions with two neighboring boron nuclei. The following spin Hamiltonian describes this situation.

$$\begin{aligned}
H = & \beta \mathbf{S} \cdot \mathbf{g} \cdot \mathbf{B} + \mathbf{I}_1 \cdot \mathbf{A} \cdot \mathbf{S} + \mathbf{I}_2 \cdot \mathbf{A} \cdot \mathbf{S} + \mathbf{I}_1 \cdot \mathbf{Q} \cdot \mathbf{I}_1 + \mathbf{I}_2 \cdot \mathbf{Q} \cdot \mathbf{I}_2 \\
& - g_N \beta_N \mathbf{I}_1 \cdot \mathbf{B} - g_N \beta_N \mathbf{I}_2 \cdot \mathbf{B}
\end{aligned} \tag{3.4}$$

In this spin Hamiltonian, each boron nucleus interacting has its own hyperfine, nuclear electric quadrupole, and nuclear Zeeman term.

During the present investigation, it became clear that the slight inequivalence reported for the interactions with the two boron nuclei was due to the difficulty of aligning the magnetic field along the crystal axes. Instead, the present investigation shows that the interactions with the two boron nuclei are equivalent, within experimental error. After determining that the two boron nuclei are equivalent, the spin Hamiltonian used to describe the ENDOR spectra only needs to be written for one nucleus.

$$H = \beta \mathbf{S} \cdot \mathbf{g} \cdot \mathbf{B} + \mathbf{I} \cdot \mathbf{A} \cdot \mathbf{S} + \mathbf{I} \cdot \mathbf{Q} \cdot \mathbf{I} - g_N \beta_N \mathbf{I} \cdot \mathbf{B} \tag{3.5}$$

With an isotropic  $g$  value and experimental ENDOR data, Eq. 3.5 was used to determine the spin Hamiltonian parameters describing the hyperfine and nuclear electric quadrupole matrices for the low temperature trapped hole center in LTB.

The spin Hamiltonian is “solved” using a least-squares fitting routine. The fitting routine diagonalizes the spin Hamiltonian matrix and iterates through each parameter that needs to be determined. The parameters are incrementally stepped until the sum of the squares is minimized. The quantity being minimized is the sum of the differences (squared) between the measured and calculated ENDOR frequencies. The fitting routine determined the set of parameters that gave a “best fit” to the ENDOR data collected when the magnetic field was aligned parallel to the [001], [101], [100], and [110] crystal directions. These results are listed in Table 3.1. Keep in mind that there are three principal values and three independent Euler angles. The Euler angles describe the

rotations needed to transform the given parameter from the lab frame (of which the fitting parameter is solved) to the parameter's principal directions where its representative matrix is diagonalized with the principal values given.

Table 3.1. Principal values and principal angles of the g, A, and Q matrices for the hole center in LTB. Values for g are assumed isotropic. There are no principal angles listed for the g matrix since it is assumed isotropic.

Parameter	Principal Value	Principal (Euler) Angle
g		
$g_x$	2.0125	--
$g_y$	2.0125	--
$g_z$	2.0125	--
Hyperfine		
$A_1$	9.516	23.6°
$A_2$	14.549	-14.6°
$A_3$	20.094	27.7°
Quadrupole		
$Q_1$	-0.069	46.5°
$Q_2$	-0.119	71.8°
$Q_3$	0.188	0.1°

Figure 3.6 shows the graphical results of the ENDOR fitting routine. The solid lines represent a plot of the spin Hamiltonian results using the g, A, and Q matrix parameters determined by the fitting routine. The blue circles represent the experimental data. Four of the eight crystallographically equivalent sites are also labeled and color coded for continuity. A consistent set of site assignments were determined during the

fitting process. Incorrect assignments result in large values for the sum of the squares calculated by the fitting routine.

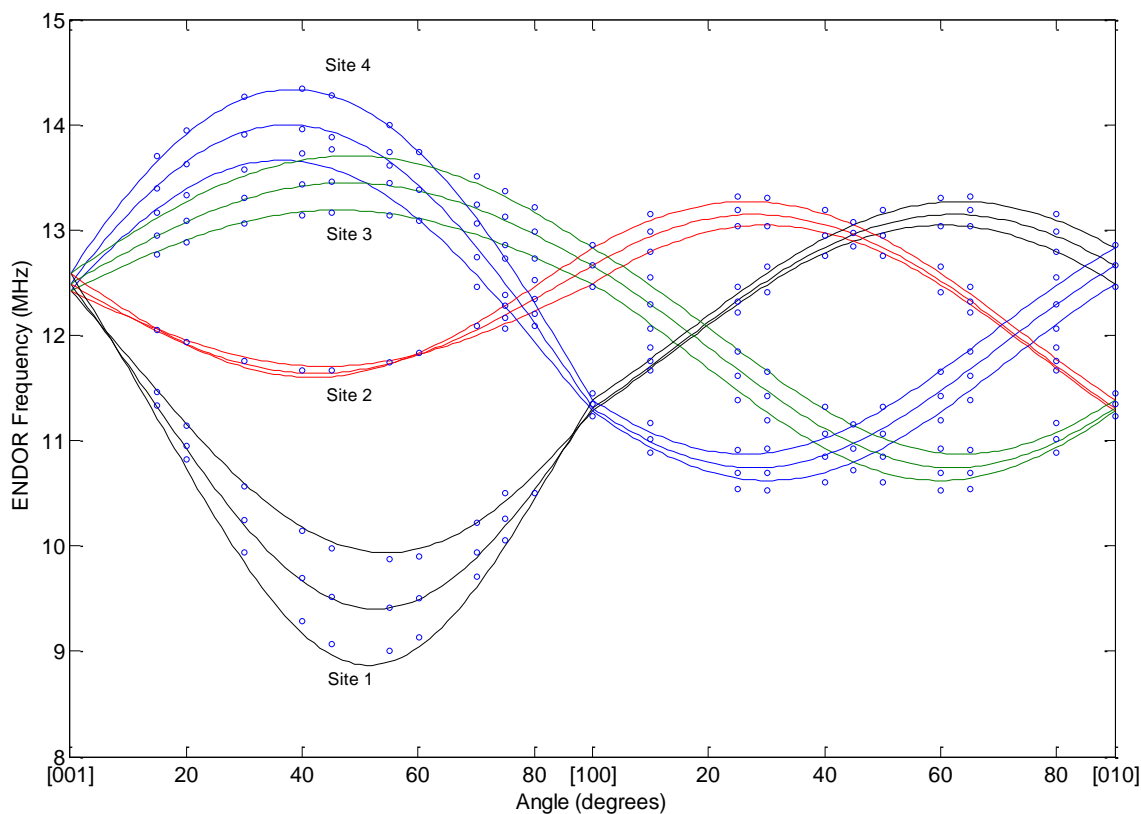


Figure 3.6. ENDOR angular dependence plot. Solid lines are calculated using the best-fit parameter values and open circles represent experimental data.

### 3.6. Discussion

This investigation provided several interesting results. First, an explanation has been provided for the single peak corresponding to Site 2 that is present in the ENDOR spectra as the magnetic field is rotated from the  $c$  axis to the  $a$  axis. The quadrupole splitting has a value of zero for two different orientations of the magnetic field in the  $c$  to  $a$  plane. This causes the ENDOR triplet to collapse into a single peak at these points. In

between these zero points, the lines comprising the triplet are close together and remain unresolved. Thus, in this  $c$  to  $a$  plane, Site 2 appears as a single broad line for 60 degrees of magnetic field rotation.

Second, the two boron nuclei adjacent to the trapped hole have nearly identical hyperfine matrices. This observation was initially surprising, as there is no fundamental reason why the two interactions should be the same. The evidence that these two hyperfine matrices are nearly identical is quite clear when the EPR and ENDOR spectra are both taken into consideration. The EPR spectrum, shown in Fig. 3.2(a), contains seven equally spaced lines and thus demonstrates that two boron nuclei are involved. On the other hand, the  $c$ -axis ENDOR spectrum, shown in Fig. 3.6, does not contain resolved sets of lines from two different boron nuclei. Thus, the ENDOR lines from the two nuclei must coincide for this orientation of magnetic field. Furthermore, the angular study shows that the ENDOR lines of the two nuclei overlap for all angles. This proves that the hyperfine matrices for the two boron nuclei are equivalent (i.e., the sets of ENDOR lines for the two separate nuclei cannot be experimentally resolved).

The nearly equivalent nature of the two boron hyperfine interactions means that the principal axes associated with the anisotropic portion of each matrix must have the same directions, i.e., they are collinear. In terms of a model, recall that the unpaired spin resides primarily on an oxygen ion and interacts with the two adjacent boron ions. Equivalent boron interactions would be easily explained if these three ions were to lie collinear in the crystal. However, in the LTB lattice, there is no location where these three ions line up. This suggests that lattice relaxations may be important in determining the equilibrium ground state structure of the trapped hole center. A typical lattice

relaxation can be between 5 and 10 percent of a lattice spacing and this movement might be sufficient to bring an oxygen ion more in line with its two boron neighbors.

The next step is to suggest a specific model for the defect. Originally, Swinney et al. [31] proposed that a likely model had the hole localized on an O(4) atom (see the basic LTB structure in Fig. 3.7(a)). This site was suggested because the O(4) atom is the only oxygen that has two equivalent boron neighbors, both being B(2) ions. Though this model could be correct, there are several concerns. One question deals with the boron-oxygen-boron angle which is 108 degrees for the O(4) site versus the approximately 180 degree angle suggested by the experimental data. A second questions deals with the separation distance between the adjacent stabilizing lithium vacancy and the O(4) oxygen ion trapping the hole. In the unrelaxed lattice, the separation distance between the O(4) ion and the lithium vacancy is the greatest of all lithium-oxygen separations.

There are other possible oxygen ions where the hole may be trapped. It could be trapped on an O(1) ion near the lithium vacancy. This possible hole location is illustrated in Fig. 3.7(b). There are two  $(\text{B}_4\text{O}_9)^{6-}$  units shown in this figure along with an adjacent lithium ion. The figure is rotated to show the best view. This O(1) location is very close to a lithium vacancy. This is the second closest location among the five oxygen ions near each lithium vacancy. Furthermore, this location of the hole has, at 126 degrees, the largest angle between an oxygen ion and its two neighboring boron ions. Although this angle is still much less than 180 degrees in the unrelaxed lattice, it does not necessarily eliminate this oxygen ion as being the site of the trapped hole. The unique principal axes of the hyperfine matrices may not coincide with the boron-oxygen bond directions. The

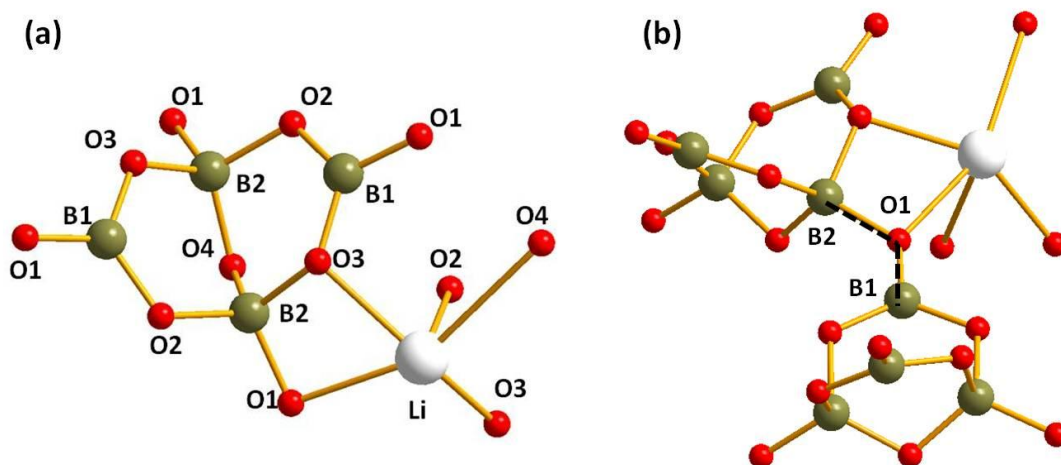


Figure 3.7. (a) Schematic representation of the basic  $(B_4O_9)^{6-}$  structural building block in  $Li_2B_4O_7$  crystals. This is an arbitrary projection. (b) Possible hole trap location that is different from the model suggested by Swinney et al. [31].

spatial distribution of the  $p$ -like wave function of the hole governs the principal axes directions of the hyperfine matrices. Without a full *ab initio* quantum chemistry calculation, the orientation of the  $p$  orbital containing the hole is not known. The structure of LTB makes it difficult to be certain of the trapped hole location.

Similar EPR and ENDOR experiments were performed in 2002 at West Virginia University on lithium triborate ( $LiB_3O_5$ ) crystals. These crystals are referred to as LBO crystals. The investigation was part of the PhD dissertation of Wei Hong [39]. This study Wei Hong identified and characterized two low temperature hole centers in the LBO crystals. The two trapped hole centers had similar  $g$ , hyperfine, and nuclear electric quadrupole parameters. The thermal stabilities of the trapped hole centers in the two materials are similar. However, the trapped hole centers in the two materials had one major difference in their properties. In LBO, only one boron ion interacted strongly with



the trapped hole on an oxygen ion, whereas in LTB, two boron ions interact strongly with the trapped hole on an oxygen ion, as shown in this dissertation. A representative spectrum from the Wei Hong dissertation is provided in Fig. 3.8. It shows the four EPR transitions resulting from an electron spin  $S = 1/2$  hole interacting with a  $^{11}\text{B}$  nucleus of nuclear spin  $I = 3/2$ . The lithium triborate crystal, with orthorhombic symmetry, has four crystallographically equivalent defect orientations compared to eight orientations found in the tetragonal lithium tetraborate crystal. In LBO, all of the sites are equivalent when the magnetic field is parallel to any one of the three crystal axes. In LTB, site equivalence only occurs when the magnetic field is parallel to the crystal's  $c$  axis.

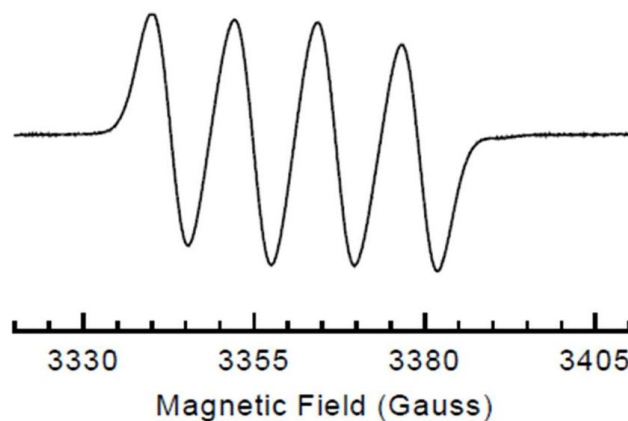


Figure 3.8. Representative EPR spectrum from a trapped hole center in an LBO crystal.

This spectrum was taken with the magnetic field parallel to the  $c$  axis of the crystal.

(Taken from the PhD Dissertation of Wei Hong.) [39]

Similarities between the LBO and LTB crystals are found in their structural units. The lithium ions are crystallographically equivalent in their respective lattices. In other words, there is only one lithium site in each lattice. The  $\text{BO}_4$  and  $\text{BO}_3$  structural units are

present in both LBO and LTB. In an LTB crystal, the basic building block is a  $(B_4O_9)^{6-}$  group consisting of two  $BO_4$  units and two  $BO_3$  units. In contrast, the basic building block in an LBO crystal is a  $(B_3O_7)^{5-}$  group, consisting of one  $BO_4$  unit and two  $BO_3$  units. The LTB structure is shown in Fig. 3.7(a) and the LBO structure is shown in Fig. 3.9 (a). Both structures have oxygen ions that have two boron neighbors with similar oxygen-boron bond lengths, between 1.35 Å and 1.50 Å.

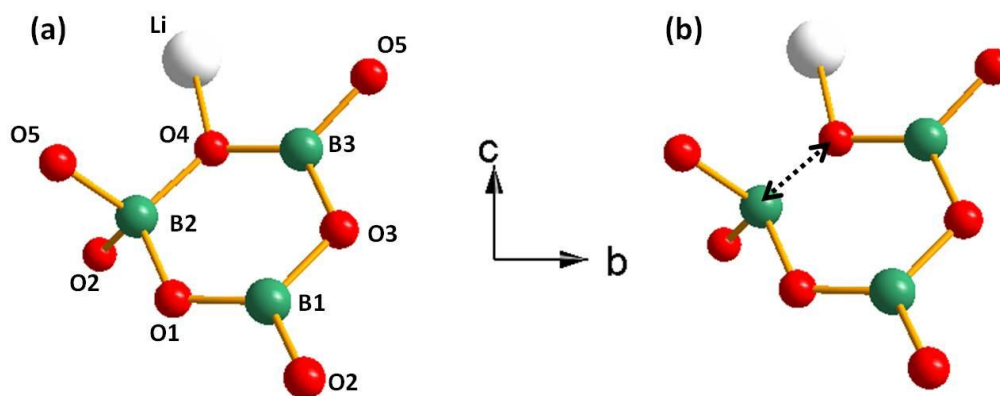


Figure 3.9. (a) Basic structural unit of an  $LiB_3O_5$  crystal. Labels identify inequivalent ion sites. (b) Proposed model for the hole trap in LBO (from the Wei Hong dissertation).

In the LBO crystal, the oxygen atom at the O(4) site was determined to be the location of the trapped hole. The sites are labeled in Fig. 3.9(a). After trapping the hole, the neighboring B(2) ion relaxes significantly toward the three remaining oxygen atoms that comprise the  $BO_4$  unit. Figure 3.9(b) shows the hole location with one bond removed and the ions at their relaxed positions. Gaussian 98 *ab initio* calculations were also performed and confirmed the EPR experimental data [40]. Gaussian is an *ab initio* molecular orbital computer program that uses the unrestricted Hartree-Fock method. When using this program, one simulates a defect by constructing a large molecule that

represents a subset of ions within the crystal and has the defect near the center. This simulated molecule contains one or more of the basic building blocks of the crystal. An appropriate basis set is chosen and the program then calculates the electronic energy of the ground state. A geometry optimization provides the final relaxed positions of the ions around the defect.

Table 3.2 shows the  $g$ ,  $A$ , and  $Q$  principal values obtained from the trapped hole centers in LBO. These were obtained from angular dependent EPR data that were fit with a least squares routine. There are two items to note in the principal values for the LBO hole traps. First, the  $g$  values in LTB are similar to those in LBO and thus support the assignment in LTB to a trapped hole center. Second, the hyperfine parameters in LTB are approximately half of those determined for LBO.

The results from LBO can be used to develop a plausible model for LTB. The borate structures are expected to behave in a similar manner in the two materials. In LBO, the oxygen ion traps a hole and causes the neighboring boron ion to relax away from the hole and toward the remaining three oxygen ions. Applying this scenario to LTB suggests that the O(1) ion (see Fig. 3.7(b)) may be a good candidate for the hole location. If the O(1) ion contains a hole, it would be reasonable to have the neighboring boron ions, B(1) and B(2), relax away from the hole and toward their remaining oxygen ions. This may allow the O(1) ion and its two neighboring boron ions to form a linear chain. This would explain the experimental observation that LTB has equivalent hyperfine interactions with two boron ions. A quantum chemistry molecular orbital calculation could help prove or disprove this suggested model.

Table 3.2. Principal values obtained for trapped hole centers in LBO. Principal axes directions are specified by polar and azimuthal angles  $\theta$  and  $\varphi$ . (taken from the dissertation of Wei Hong) [39]

Parameter	Principal Value	Principal Axis Directions	
g matrix		$\theta$	$\varphi$
$g_x$	2.0021	50.5°	259.1°
$g_y$	2.0101	62.4°	143.6°
$g_z$	2.0456	51.9°	29.4°
Hyperfine matrix			
$A_1$	-34.49	56.8°	266.2°
$A_2$	-38.53	53.4°	147.2°
$A_3$	-19.84	54.0°	24.6°
Quadrupole matrix			
$Q_1$	-0.138	40°	350°
$Q_2$	-0.288	82°	250°
$Q_3$	0.426	51°	153°

This research project has provided some insight to the use of lithium tetraborate as a possible neutron detection material. Experiment has shown that there are large numbers of lithium and compensating oxygen vacancies in the as-grown crystals [31]. These vacancies are responsible for trapping electrons and holes. The trapped hole center investigated in this chapter has a very low thermal stability, less than 90 K, and is populated during exposure to ionizing radiation. These trapped holes recombine with trapped electrons and release visible light when the crystal is heated above 90 K. The hole trapping centers could have both a positive and negative effect on the performance of LTB as a scintillating material. With respect to a positive aspect, the oxygen and lithium vacancies may aid in scintillation detection. A nuclear event, i.e., neutron

capture, in LTB is accompanied by ionizing radiation. This ionizing radiation produces electrons and holes that will then “migrate” through the crystal lattice. These electrons and holes may possibly recombine at the hole trapping site investigated in this chapter and produce visible light that could be collected in a photomultiplier tube. In terms of a negative effect, ionizing radiation unrelated to neutron capture may produce electron hole pairs that then lead to a “false” count in a neutron detector from the same principles.

Additional work is needed to determine the feasibility of using LTB as a neutron detection material. EPR has provided insight into the electron and hole centers involving lithium and oxygen vacancies. Future research may determine if a post-growth annealing process could be utilized to reduce the lithium and oxygen vacancy concentrations. Such a process has been developed for lithium niobate [41]. This process is referred to as vapor phase equilibration and consists of heating the crystal in a lithium-containing vapor. Lithium ions enter the crystal as interstitials, eliminate the lithium vacancies, and restore the crystal to its stoichiometric form. If a post-growth annealing process proved successful in LTB, crystals having different concentrations of vacancies could then be exposed to a neutron source and the resulting detector performance evaluated.

This work, characterizing the point defects in lithium tetraborate, has applications that could extend beyond neutron detection. Lithium tetraborate has an appreciable pyroelectric coefficient and thus could be used as a thermal sensor [42-43]. LTB also has moderately large piezoelectric constants that make these crystals suitable for signal processing and frequency control devices [44-46]. Acoustic loss peaks associated with point defects degrade device performance.

## **IV. Perturbed and Unperturbed Hole Centers ( $\text{Ag}^{2+}$ Ions) in Silver-Doped Lithium Tetraborate Crystals**

### **4.1. Background**

The introduction to this dissertation presents the idea that lithium tetraborate doped with an appropriate impurity could be utilized in radiation detection applications involving scintillation. Lithium tetraborate crystals doped with Ag are excellent candidates for radiation-detection applications involving light emission because the silver nuclei trap electrons and holes that recombine above room temperature and radiate efficiently [47-50]. Collaborative research conducted by the Air Force Institute of Technology and West Virginia University identified two distinct hole centers and an electron center in lithium tetraborate crystals doped with silver ions [51]. These centers were identified using electron paramagnetic resonance, after the crystals had been exposed to x-ray radiation. In this investigation, thermoluminescence showed that the electrons and holes trapped at these centers recombine above room temperature, emitting visible light that was collected using a photomultiplier tube. This initial work was published [51] and demonstrates the potential for using silver-doped lithium tetraborate for radiation dosimetry [52-54] and neutron detection involving light emission. However, the centers participating in the electron-hole recombination mechanisms need to be more completely characterized in order to fully develop lithium tetraborate for these optical applications. It is important to investigate all of the point defects, both intrinsic and extrinsic (unintentional or intentional impurities), that will affect the performance of LTB as a radiation detector.

The research of Brant et al. [51] included the identification of two  $\text{Ag}^{2+}$  hole centers that were labeled as perturbed and unperturbed. The unperturbed hole center was characterized using both EPR and ENDOR to determine the  $g$  and hyperfine matrix parameters. This center was determined to be a  $\text{Ag}^{2+}$  ion occupying a lithium site in the lattice and having no nearby defects. It was suggested that the perturbed center was a  $\text{Ag}^{2+}$  ion sitting at a lithium site, except that it has a perturbing ion in the local environment. For example, a neighboring sodium or silver monovalent ion sitting on an adjacent lithium site would cause the slight shifts in  $g$  and hyperfine parameters compared to that of the unperturbed center. On the other hand, the electron center was identified as an interstitial silver atom ( $\text{Ag}^0$ ) residing near a boron ion at a regular lattice position [51]. The unperturbed  $\text{Ag}^{2+}$  hole center and the electron center were characterized in the initial investigation. The third center, the perturbed  $\text{Ag}^{2+}$  ion, was not characterized at that time because its EPR spectrum was not easily resolved.

Both of the hole centers observed in silver-doped LTB are the result of a hole trapped on a silver ion, i.e., a  $\text{Ag}^{2+}$  ion is formed. Before irradiation, a portion of the silver ions are present as nonparamagnetic  $\text{Ag}^+$  ions ( $4d^{10}$ ) replacing  $\text{Li}^+$  ions. After irradiation, these centers trap a hole and convert to  $\text{Ag}^{2+}$  ions ( $4d^9$ ) with a spin of  $S = 1/2$ . Silver has two stable isotopes,  $^{107}\text{Ag}$  and  $^{109}\text{Ag}$ . Both isotopes are approximately 50% abundant ( $^{107}\text{Ag} = 51.83\%$  and  $^{109}\text{Ag} = 48.17\%$ ) and have a nuclear spin of  $I = 1/2$ . They also have similar nuclear magnetic moments,  $-0.1135$  ( $^{107}\text{Ag}$ ) and  $-0.1305$  ( $^{109}\text{Ag}$ ). The magnetic moments here are expressed in “units” of nuclear magnetons, i.e., they are the ratio  $\left(\frac{\mu}{\mu_n}\right)$  of their moments to that of the nuclear magneton. For each silver isotope, the interaction of an electron of spin  $1/2$  with a nucleus of spin  $I = 1/2$  produces an EPR

spectrum consisting of two lines. Thus, for one  $\text{Ag}^{2+}$  ion, there will be two doublets, one associated with each silver isotope, with slightly different separations as a result of their different magnetic moments. However, the nearly equal natural abundances and the nearly equal magnetic moments of these two isotopes cause the EPR hole-center spectrum associated with  $^{107}\text{Ag}$  and  $^{109}\text{Ag}$  to appear as a single broadened doublet. In other words, the individual doublets due to the  $^{107}\text{Ag}$  and  $^{109}\text{Ag}$  nuclei are not resolved in

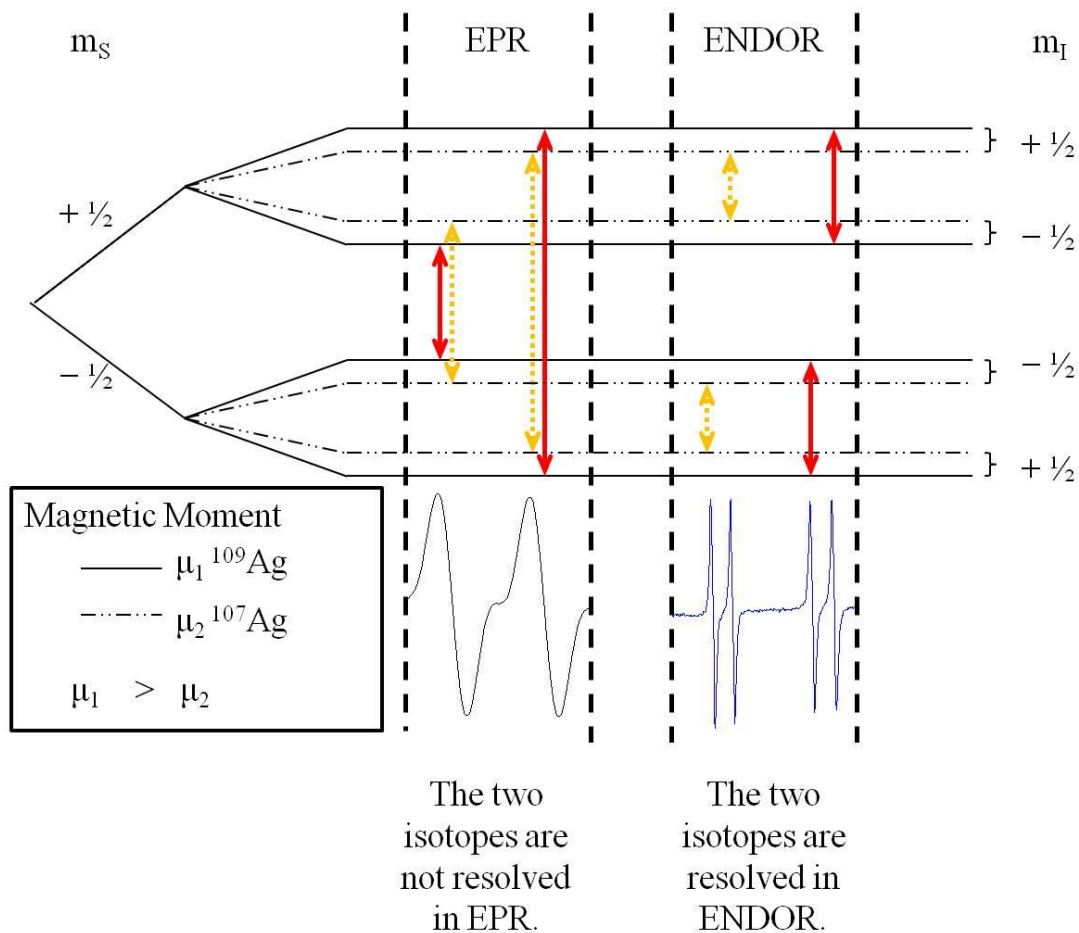


Fig. 4.1. Energy level diagram for the  $\text{Ag}^{2+}$  hole centers. The energy levels associated with the two isotopes are illustrated and the allowed EPR and ENDOR transitions are shown where the solid red lines correspond to  $^{109}\text{Ag}$  and the dotted orange lines correspond to  $^{107}\text{Ag}$ .



EPR. The energy level diagram shown in Fig. 4.1 illustrates the lack of resolution in the EPR experiment and the increased resolution in the ENDOR experiment. The increased resolution is demonstrated in Fig. 4.1 under the ENDOR portion.

As shown in the right portion of Fig. 4.1, electron-nuclear double resonance (ENDOR) can resolve the hyperfine lines. Because  $A/2$  is larger than  $\nu_N$  for the  $\text{Ag}^{2+}$  ions, each silver isotope produces an ENDOR spectrum consisting of two peaks centered on  $A/2$  and separated by  $2\nu_N$ . Each Ag isotope has a different value of  $\nu_N$  (.606 Mhz for  $^{107}\text{Ag}$  and .698 MHz for  $^{109}\text{Ag}$ ); this leads to a different separation between the ENDOR doublets and aids in identification of silver as the responsible nuclei. In Fig. 4.2, the upper blue spectrum consists of two doublets. The doublet between 32 and 34 MHz has a separation close to 1.4 MHz and can be assigned to  $^{109}\text{Ag}$ , while the doublet between 28 and 30 MHz has a separation close to 1.2 MHz and can be assigned to  $^{107}\text{Ag}$ . A second aid in identifying silver as the responsible nuclei resides in the mid-points, or  $A/2$  values, of the two doublets observed in the ENDOR spectrum. Both  $\nu_N$  and  $A$  are proportional to the magnetic moment. The ratio obtained by dividing the  $A/2$  measured for the  $^{109}\text{Ag}$  by the  $A/2$  measured for the  $^{107}\text{Ag}$  nucleus should match the ratio of their magnetic moments, or 1.152. The ENDOR spectrum from the perturbed  $\text{Ag}^{2+}$  hole center, presented in the lower portion of Fig. 4.2, shows two transitions at 21.34 and 20.23 MHz for  $^{109}\text{Ag}$  and two transitions at 18.47 and 17.48 MHz for  $^{107}\text{Ag}$ . The mid-points are thus 20.785 and 17.975 MHz, respectively, and have a ratio of 1.156. This ratio is in close agreement with the ratio of the Ag magnetic moments.

The earlier study performed by Brant et al. [51] characterized the unperturbed  $\text{Ag}^{2+}$  hole center. Angular dependence EPR data was collected to determine the  $g$  matrix

and ENDOR data was collected to determine the hyperfine matrix for each isotope. In this study, a similar approach was attempted for the perturbed  $\text{Ag}^{2+}$  hole center. However, there were several complications that made characterizing the perturbed  $\text{Ag}^{2+}$  hole center more difficult. First, the intensity of the perturbed center in EPR spectra is less than half of the intensity of the unperturbed center. This is due to the lower concentration of the perturbed defect compared to that of the unperturbed. Also, the lower intensity of the EPR signal correlates with a lower intensity of ENDOR signals. An even greater problem arises because the spin-lattice relaxation times associated with the perturbed  $\text{Ag}^{2+}$  center are not conducive to strong ENDOR transitions. Another complication encountered while characterizing the perturbed  $\text{Ag}^{2+}$  hole center is a lack of clearly observable EPR lines at a variety of orientations of the magnetic field, i.e., the perturbed center EPR lines are often under the more prominent EPR signals from the unperturbed center. There are eight independent sites in the crystal and thus eight orientations of a given defect. When the magnetic field is rotated in a high symmetry plane of the crystal, the tetragonal structure of LTB reduces the number of sites observed in an EPR spectrum to four or less. The lines of the perturbed  $\text{Ag}^{2+}$  sites, are often times under the unperturbed  $\text{Ag}^{2+}$  lines. Thus, it is difficult to observe a large number of transitions of the perturbed  $\text{Ag}^{2+}$  hole center when the magnetic field is parallel to many of the directions in the crystal.

Attempts were repeatedly made in the current study to obtain a complete set of ENDOR data for the perturbed  $\text{Ag}^{2+}$  center. Success was not achieved. Much of this effort involved trying to determine the optimum ENDOR spectrometer settings. These included temperature, modulation frequency, modulation amplitude, RF power, and

microwave power. The ENDOR spectrum from the perturbed  $\text{Ag}^{2+}$  ions was always much lower in intensity than that from the unperturbed  $\text{Ag}^{2+}$  ions. The difference in intensities of the ENDOR spectra from the unperturbed and perturbed  $\text{Ag}^{2+}$  hole center is shown in Fig. 4.2. The lower frequency signals of the upper spectra are from the

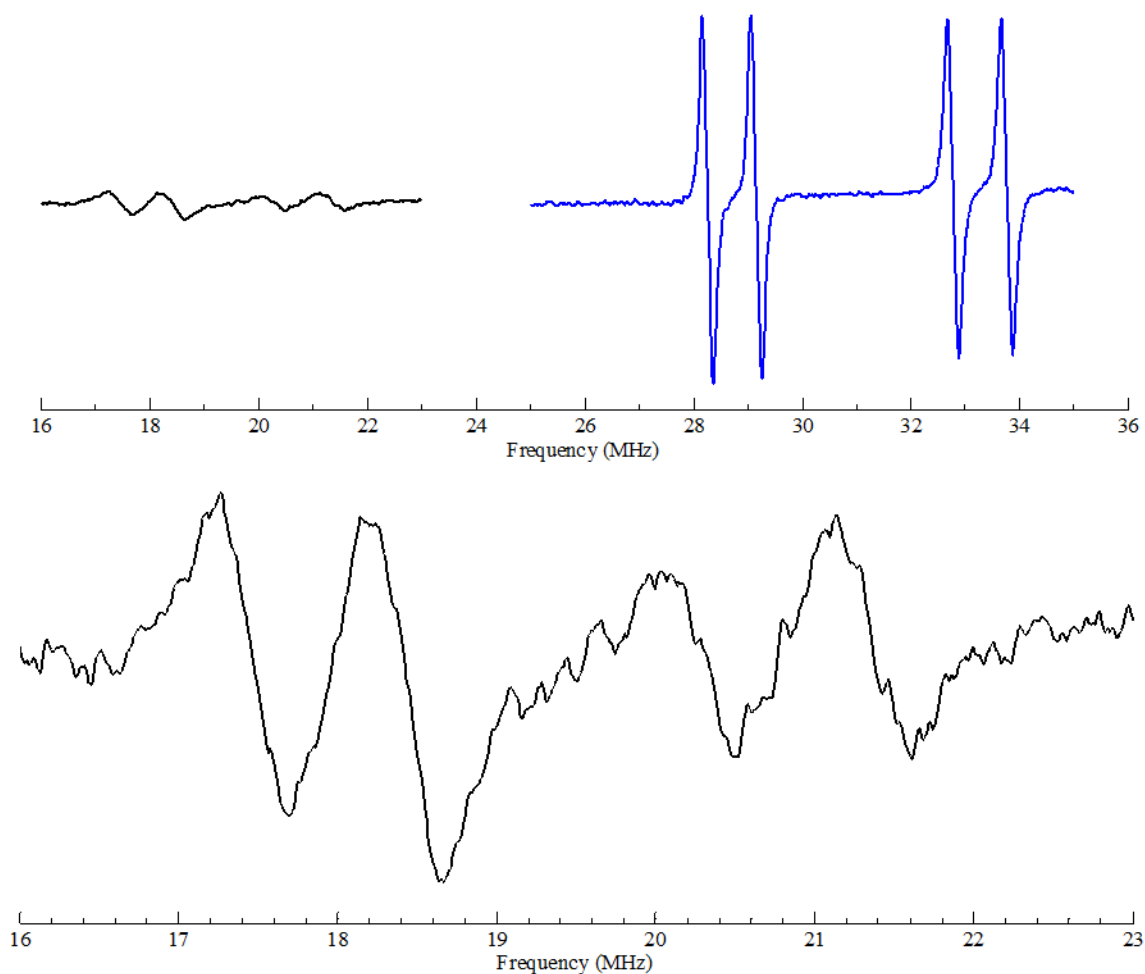


Fig. 4.2. ENDOR spectra collected for the unperturbed (blue and upper right) and perturbed (black and upper left)  $\text{Ag}^{2+}$  hole centers. These spectra were collected during the same experiment, but while the magnetic field was “parked” on each respective EPR transition, i.e., two separate data collections. The lower trace shows the magnified spectrum of the perturbed  $\text{Ag}^{2+}$  hole center.

perturbed  $\text{Ag}^{2+}$  center and the higher frequency signals in this spectrum (shown in blue) are from the unperturbed  $\text{Ag}^{2+}$  center. In this figure, the ENDOR spectrum for the unperturbed  $\text{Ag}^{2+}$  hole center is eight times greater in magnitude compared to the perturbed  $\text{Ag}^{2+}$  hole center. The lower portion of Fig. 4.2 shows an expanded and magnified view of the ENDOR spectrum of the perturbed  $\text{Ag}^{2+}$  center. Here, all four ENDOR transitions associated with the two silver isotopes are easily identified. During this investigation, most of the ENDOR peaks could be seen above the noise when the magnetic field was rotated between the  $c$  axis and the  $a$  axis of the crystal. However, several attempts failed to find ENDOR lines above the noise when the magnetic field was rotated in the basal plane from an  $a$  axis to an  $a$  axis of the crystal. Most likely, this is a result of the dependence of the spin-lattice relaxation time on the direction of the external static magnetic field in the crystal. After several attempts, it became clear that the collection of ENDOR spectra in the basal plane of the crystal would not be possible using the crystals that were available. If a full set of ENDOR were collected, it would have been possible to determine the hyperfine parameters for each silver isotope just as it was for the unperturbed  $\text{Ag}^{2+}$  hole center.

An angular dependence study using only the EPR spectra collected in the high symmetry crystal planes is sufficient to determine the  $g$  and hyperfine parameters. The hyperfine parameters determined from the EPR spectra will be an average of the parameters for the separate silver isotopes. By using only EPR spectra for data collection, it is still possible to get a full set of data and calculate all of the parameters of

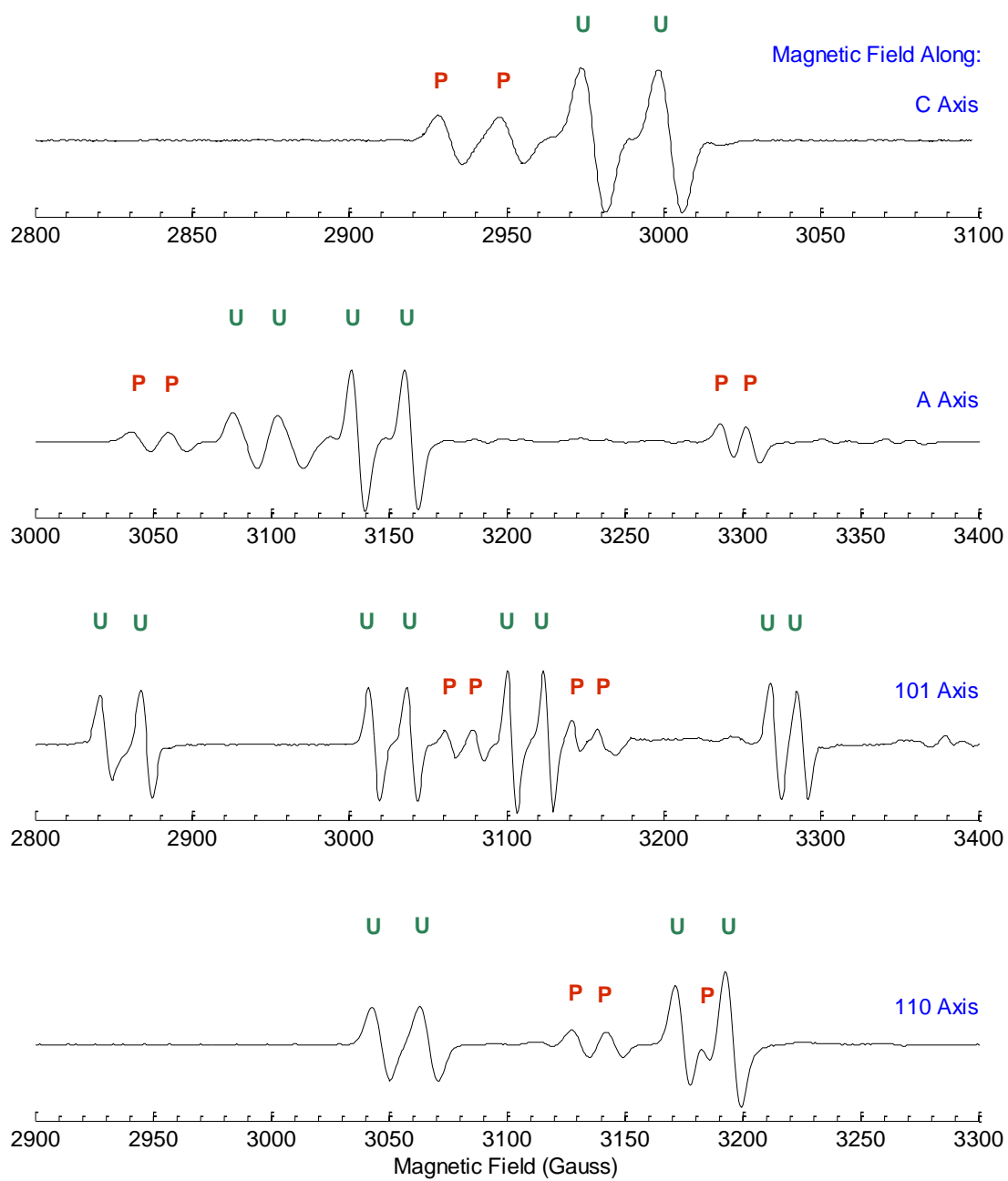


Fig. 4.3. EPR spectra of perturbed (P) and unperturbed (U)  $\text{Ag}^{2+}$  ions in LTB.

the spin Hamiltonian. Some accuracy may be lost due to the higher resolution of the ENDOR experiment.

Another complication encountered in characterizing the perturbed  $\text{Ag}^{2+}$  hole center was having enough independent data points for a fit of the spin Hamiltonian. Figure 4.3 shows EPR spectra collected when the magnetic field is parallel to high symmetry directions of the crystal, as well as the [101] crystal direction. In each spectrum, transitions are labeled with a U if the transition corresponds to an unperturbed  $\text{Ag}^{2+}$  hole center transition or a P if the transition corresponds to a perturbed  $\text{Ag}^{2+}$  hole center transition. The  $g$  and “average” hyperfine parameters can be found for the unperturbed  $\text{Ag}^{2+}$  hole center using the four spectra shown in Fig. 4.3. However, the  $g$  and hyperfine parameters cannot be precisely determined using the same spectra for the perturbed  $\text{Ag}^{2+}$  hole center. When the magnetic field is parallel to the crystal [101] direction, several of the perturbed  $\text{Ag}^{2+}$  hole center peaks are obscured by the unperturbed  $\text{Ag}^{2+}$  hole center peaks. For example, in Fig. 4.3 (magnetic field along [101] direction), there is a doublet centered on 2850 Gauss that corresponds to unperturbed  $\text{Ag}^{2+}$  hole center transitions. Upon close observation this doublet is distorted compared to the unperturbed double centered at 3150 Gauss. This distortion of the low-field doublet is due to an underlying doublet associated with the perturbed  $\text{Ag}^{2+}$  hole center. Because the spectra of Fig. 4.3 do not provide enough independent data for a fitting of the spin Hamiltonian of the perturbed  $\text{Ag}^{2+}$  hole center, a full angular study was conducted. and provided sufficient independent data to allow a good fit of the spin Hamiltonian describing the perturbed  $\text{Ag}^{2+}$  hole center.

## 4.2. EPR Results

Since ENDOR was unable to provide the hyperfine parameters for the perturbed center, it was decided to first use EPR spectra alone to re-determine the parameters of the spin Hamiltonian describing the unperturbed  $\text{Ag}^{2+}$  hole center. Then, if the parameters obtained using EPR spectra alone for the unperturbed  $\text{Ag}^{2+}$  hole center are in good agreement with the previous parameters obtained using both EPR and ENDOR [51], there is confidence that the perturbed  $\text{Ag}^{2+}$  hole center parameters obtained from the EPR spectra will be accurate. Data were taken every 10 degrees as the magnetic field was rotated from the  $c$  to the  $a$  axis of the crystal. Also, data were taken in this plane for the [101] direction. Representative spectra taken in the  $c$  to  $a$  plane are shown in Fig. 4.4. The larger peaks in this figure correspond to the unperturbed  $\text{Ag}^{2+}$  hole center and can be clearly seen. The smaller peaks, corresponding to the perturbed hole center, are present yet harder to identify and are marked with arrows. In some cases, the spectra from the two centers overlap thus making identification difficult. For example, the spectrum labeled “ $c$  axis + 10 deg twd  $a$  axis” in Fig. 4.4 contains closely spaced and overlapping lines. In order to obtain a complete set of spin Hamiltonian parameters for the perturbed  $\text{Ag}^{2+}$  hole center, there needs to be enough independent data to allow a fitting that solves for the six parameters that describe each term in the spin Hamiltonian.

After taking EPR spectra in more than 20 independent directions, four sets of spectra were identified where a full set of transitions related to the perturbed  $\text{Ag}^{2+}$  hole center could be identified. These directions are shown in Fig. 4.5. When the magnetic field is parallel to the  $c$  axis of the crystal, the eight orientations of the defect that exist in the unit cell of the crystal are all crystallographically equivalent and a single pair of EPR

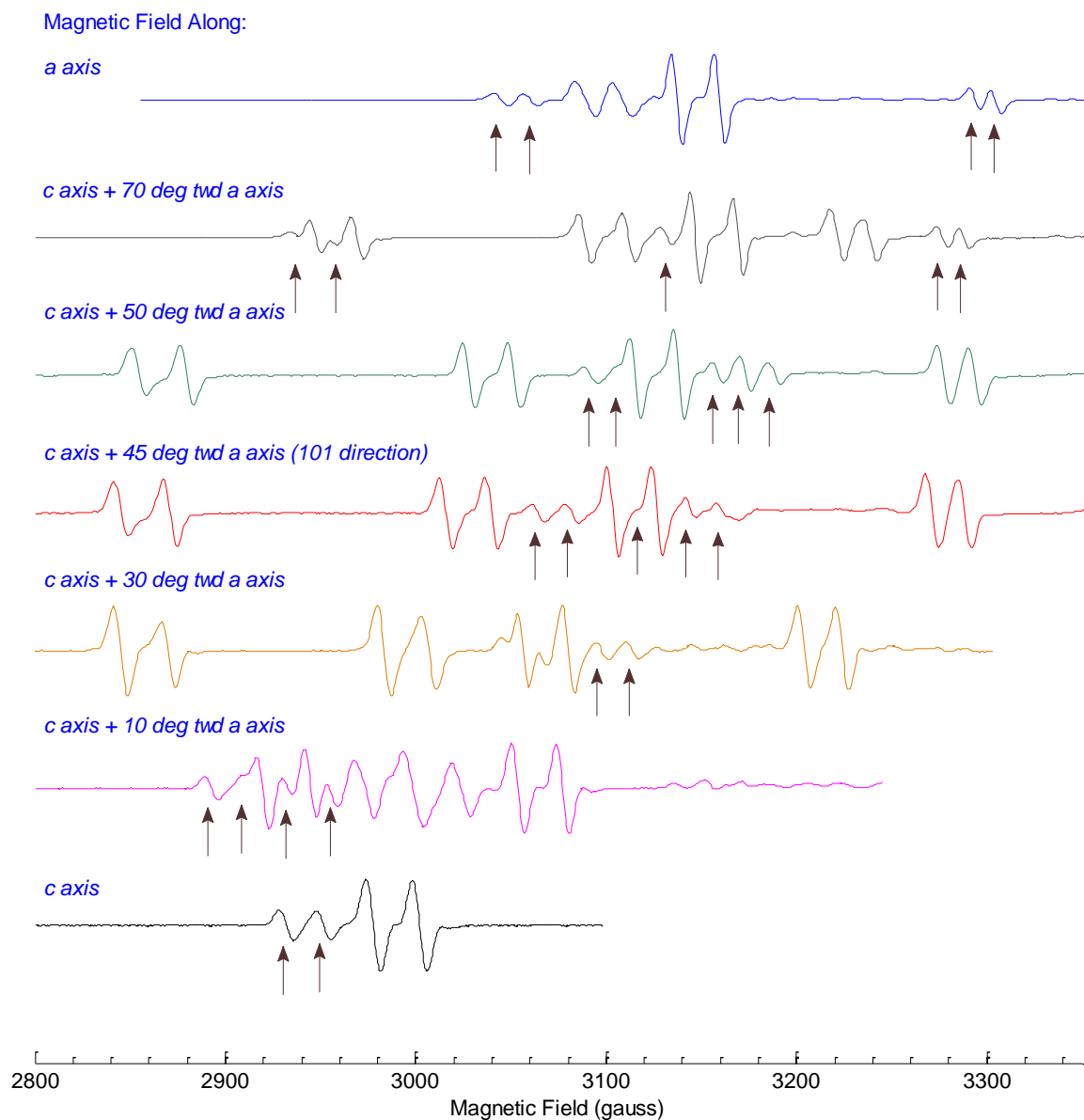


Fig. 4.4. Angular dependence data collected while the magnetic field was rotated between the *c* and the *a* axes of the crystal. Transitions for the perturbed  $\text{Ag}^{2+}$  hole center are identified with arrows.



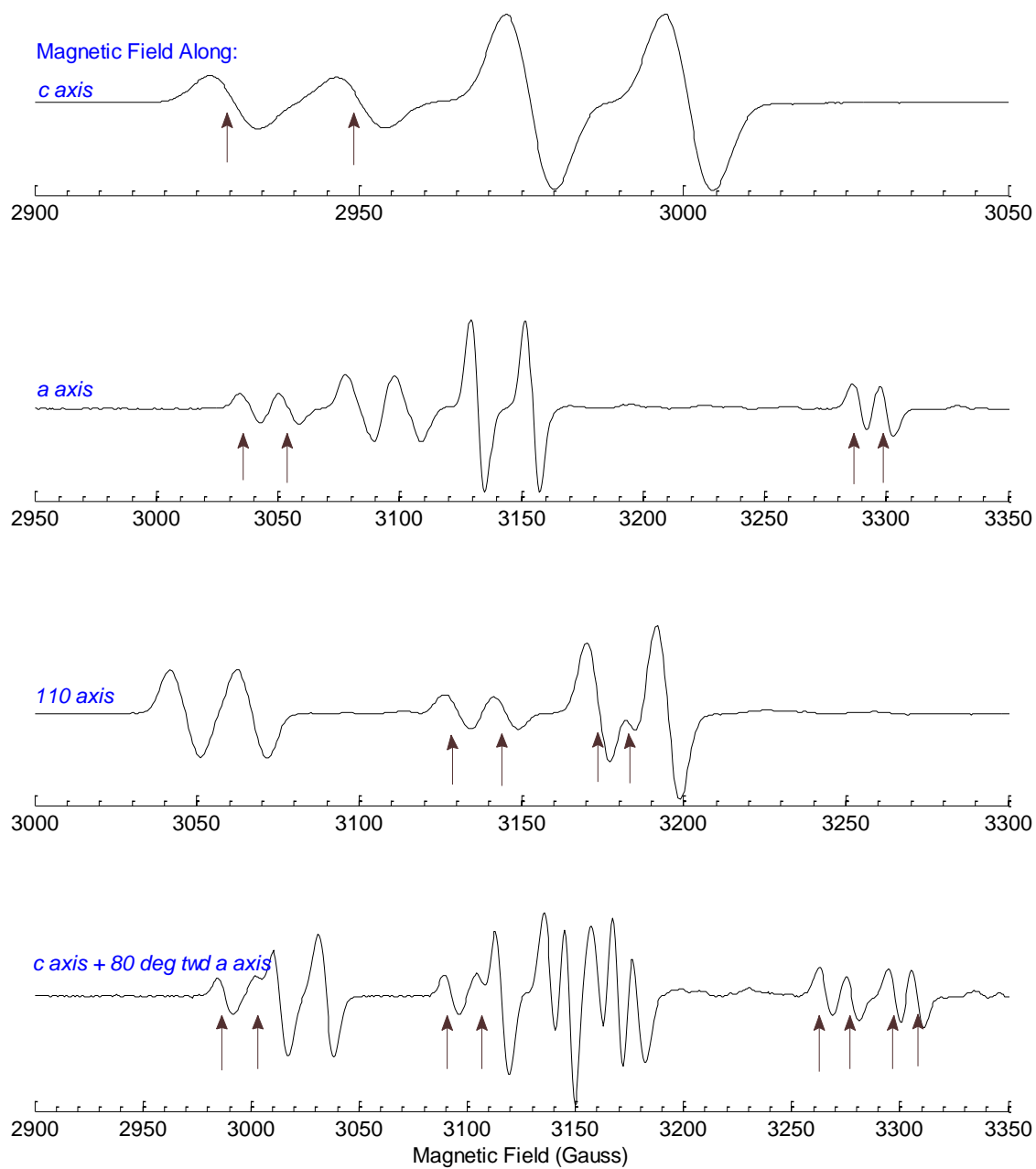


Fig. 4.5. Four independent sets of data where all of the EPR transitions for the  $\text{Ag}^{2+}$  hole center can be identified. Transitions for the perturbed  $\text{Ag}^{2+}$  hole center are identified with arrows.

transitions is observed. When the magnetic field is along the  $a$  axis and  $[110]$  directions of the crystal, the eight orientations have two equivalences thus producing four EPR transitions. Finally, when the magnetic field is in  $a$ - $c$  plane of the crystal 80 degrees from  $c$  axis toward the  $a$  axis, there were four equivalences and eight identifiable EPR transitions. Arrows are drawn in Fig. 4.5 to show the identified transitions. When the magnetic field was along the  $[110]$  direction there is a transition that is both a perturbed and unperturbed  $\text{Ag}^{2+}$  hole center transition at 3175 G. The data sets of Fig. 4.5 can be used to fit the spin Hamiltonian. To increase the accuracy of the fit, 106 transitions that could be identified for each angle of magnetic field were used compared to the 18 that could have been used.

With enough data to solve for both the perturbed and unperturbed  $\text{Ag}^{2+}$  hole center, the unperturbed center was solved first in order to compare to the published results. The parameters determined from the EPR spectra collected for this dissertation are shown in Table 4.1. These parameters were determined using a least-squares fitting routine to find the best “fit” to the spin Hamiltonian that models the unperturbed  $\text{Ag}^{2+}$  hole center. The published results of Brant et al. [51] are provided in Table 4.2. The published data was solved using the same least squares fitting routine with the exception that the hyperfine parameters for each isotope were calculated individually; in other words, the fitting routine was run separately to solve for  $^{107}\text{Ag}$  and  $^{109}\text{Ag}$ . In the current study, an average hyperfine was determined due to the lack of ENDOR data. The hyperfine principal values are the only data that are different and since the two isotopes are 52% and 48% abundant, respectively, an average of the values is provided for reference to Table 4.1. The angular dependence associated with the two sets of

parameters are plotted in Fig. 4.6. The blue circles indicate data points taken from EPR spectra acquired in the current study. The blue dashed line represents a plot of the spin Hamiltonian using the parameters that were calculated from the EPR alone (i.e., the Table 4.1 parameters). The solid red line represents a plot of the spin Hamiltonian using the parameters determined by Brant et al. from EPR and ENDOR (i.e., the Table 4.2 parameters). The averaged values of the hyperfine parameters were used when generating these solid red lines. Both sets of parameters follow the data closely and the largest difference between the two was found to be six Gauss. The widths of the individual lines in the EPR spectra for the unperturbed center were at least that value and tended to be closer to 8.5 Gauss. It can be concluded that the two sets of data are accurate within a line width of an EPR trace, which is excellent. As further illustration of experimental accuracy, an error of one degree of angular rotation of the magnetic field causes a shift of six to eight Gauss when conducting the EPR experiment for silver-doped LTB.

Table 4.1. Spin-Hamiltonian parameters calculated using EPR spectra alone for the unperturbed  $\text{Ag}^{2+}$  hole center.

Parameter	Principal Value	Principal (Euler) Angles
<b>g</b>		
$g_x$	2.0427	40.0°
$g_y$	2.1263	18.7°
$g_z$	2.3677	65.0°
<b>Hyperfine</b>		
$A_1$	45.05 MHz	29.1°
$A_2$	65.89 MHz	13.4°
$A_3$	82.88 MHz	84.1°

Table 4.2. Spin-Hamiltonian parameters calculated using EPR and ENDOR for the unperturbed  $\text{Ag}^{2+}$  hole center. (from Brant et al.) [51]

Parameter		Principal Value $^{107}\text{Ag}$	Principal Value $^{109}\text{Ag}$	Principal (Euler) Angles
<b>g</b>				
$g_x$			2.0439	40.2
$g_y$			2.1294	19.0
$g_z$			2.3708	64.4
<b>Hyperfine</b>	<b>(AVERAGE)</b>			
$A_1$	45.75 MHz	42.30	49.19	31.0
$A_2$	67.13 MHz	62.20	72.07	15.6
$A_3$	83.09 MHz	77.05	89.12	76.1

As a result of the agreement between the two methods (EPR alone versus combined EPR and ENDOR) for determining the parameters of the unperturbed  $\text{Ag}^{2+}$  hole center, the perturbed  $\text{Ag}^{2+}$  hole center was fit using data collected from the same EPR spectra. EPR transitions (or peaks) taken from the full angular dependence data were used as the experimental points in the spin-Hamiltonian fitting routine. The “best-fit” parameters of the spin Hamiltonian are presented in Table 4.3. The perturbed  $\text{Ag}^{2+}$  hole center angular dependence is shown graphically in Fig. 4.7. The solid lines are calculated using the best-fit parameter values and the open circles represent the experimental data. The lower pair of lines, between the [001] and [100] direction, has comparatively fewer data points than the other three pairs of lines. Transitions due to these orientations of the defect could not be determined due to an overlapping set of

Table 4.3. Spin-Hamiltonian parameters calculated using only EPR for the perturbed  $\text{Ag}^{2+}$  hole center.

Parameter	Principal Value	Principal (Euler) Angles
<b>g</b>		
$g_x$	2.0319	$35.5^\circ$
$g_y$	2.1212	$9.7^\circ$
$g_z$	2.3604	$-9.6^\circ$
<b>Hyperfine</b>		
$A_1$	28.18 MHz	$35.2^\circ$
$A_2$	35.81 MHz	$25.9^\circ$
$A_3$	65.12 MHz	$-38.7^\circ$

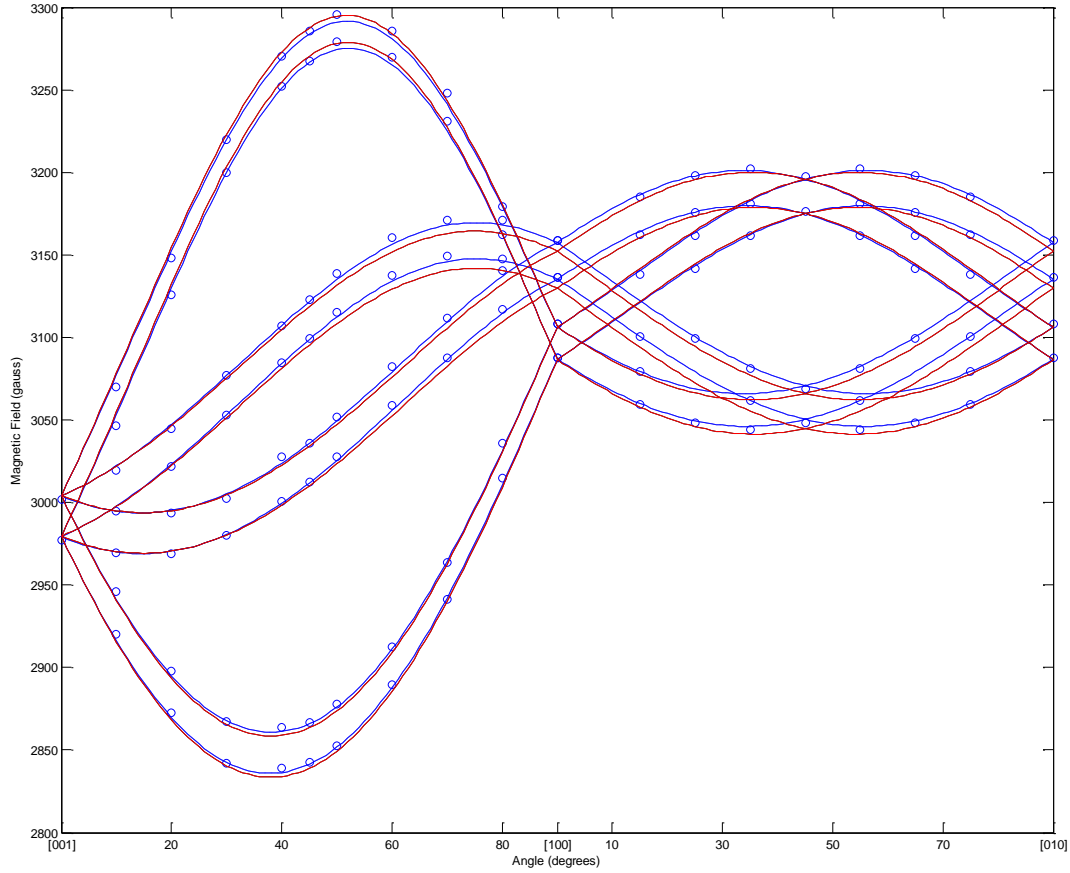


Fig. 4.6. Angular dependence comparison of the unperturbed  $\text{Ag}^{2+}$  hole center where the dashed blue lines represent fit parameters determined from EPR spectra alone are plotted along with solid red lines that represent parameters determined using EPR and ENDOR.

Blue dots represent experimental data points.

peaks from the unperturbed  $\text{Ag}^{2+}$  hole center. Squares are used in Fig. 4.7 to represent the unperturbed peak positions that covered the perturbed  $\text{Ag}^{2+}$  hole center transitions.

There is one last important item discovered during the research for this chapter. In order to fit the spin Hamiltonian using the least-squares fitting routine, site assignments need to be made relative to the data. This takes place when the data is entered into the fitting routine. In the first plane of the fitting routine, or for the [001] to the [100] direction, site assignments can be randomly assigned. Each color in Fig. 4.7 corresponds to an individual site assignment, hence eight different colors. The sites can

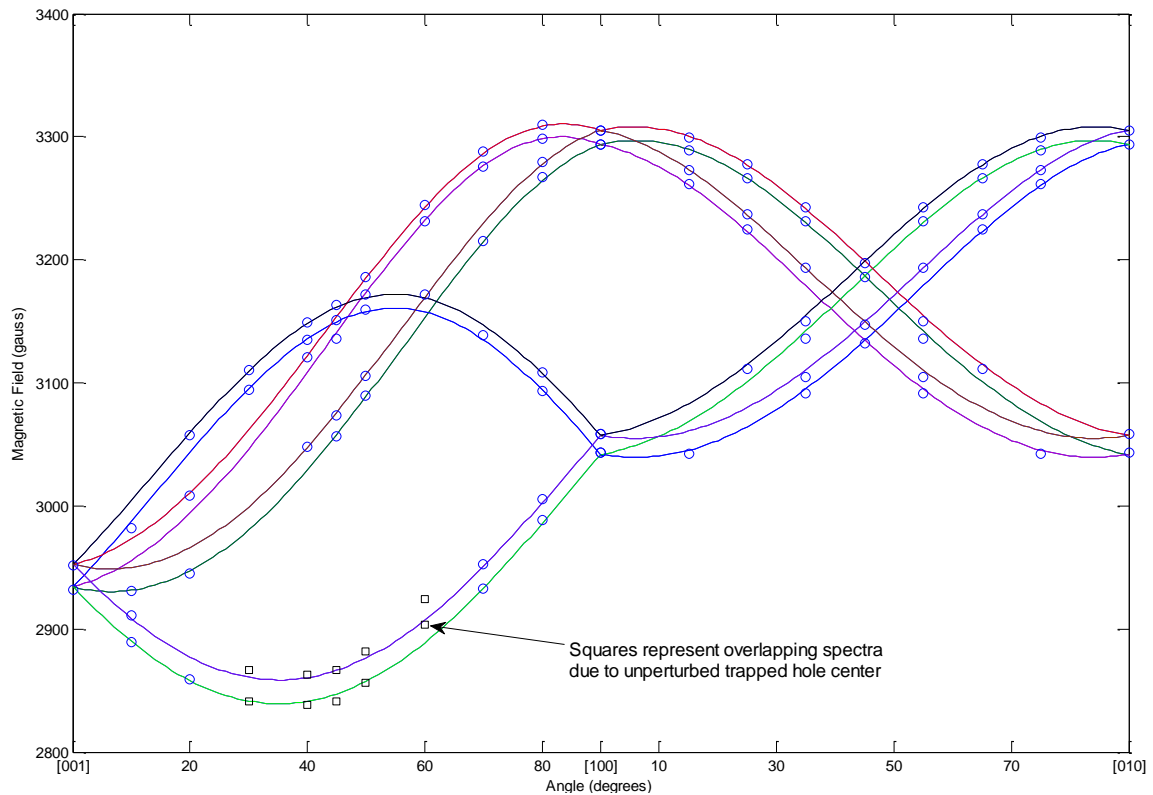


Fig. 4.7. EPR angular dependence plot. Solid lines are calculated using the best-fit parameter values and open circles represent experimental data. Each color corresponds to a specific site assignment, one through eight.

then only take on certain values between the [100] and [010] directions. For example the red line in Fig. 4.7 may correspond to site 1 in the crystal. The red line goes from the [001] plane to the upper set of transitions along the [100] direction. From the [100] direction the red line can only follow one of the four “paths” leading away from the upper set. While some choices reduced the fitting accuracy greatly, there was a second set of site assignments that gave results close to those that gave the lowest sum in the least-squares fit. There were thus two sets of parameters that closely fit the two planes of data being used in the least-squares fitting routine. For some crystal symmetries, it is impossible to create site assignments that, in turn, allow for two sets of parameters to fit the data for two planes of the crystal. In this study, it was mistakenly believed to be the case for tetragonal symmetry.

When the two different sets of parameters were plotted, the lines overlapped each other for the two planes in Fig. 4.7. However, when a third plane was plotted the two sets of data diverged and showed EPR transitions at different magnetic fields. It was therefore decided that data must be taken in this third plane to confirm that the correct site assignments were being made. Data were then taken by rotating the magnetic field between the [110] direction to the [001] direction and confirmed, in this case, that the lowest sum in the least-squares fit yielded the correct parameters. The fact that two sets of parameters can yield the same fitting for two planes has shown that a third set of data must be taken for future cases involving crystals with tetragonal symmetry when an angular dependence study is going to be performed. The third plane of data is not

presented in this dissertation as it does not improve the accuracy of the spin-Hamiltonian parameters, but does confirm correct site assignments.

### 4.3. Discussion

In order for lithium tetraborate to become a viable candidate for dosimetry and nuclear detection applications [55-56], it is important to characterize all of the defects in the material. The  $g$  and hyperfine values for the perturbed  $\text{Ag}^{2+}$  hole center have not been previously reported. This chapter has shown that it is possible to find a good set of  $g$  and hyperfine parameters using EPR alone for a defect that contains two isotopes of similar nuclear magnetic moments that could not otherwise have been characterized.

The  $g$  matrix principal values determined in this research are in good agreement with results reported in earlier studies of  $\text{Ag}^{2+}$  ions in other crystals [57-59]. The values of the  $g$  and hyperfine matrices do not, however, provide enough information for an improved model that clearly establishes the difference between the perturbed and unperturbed  $\text{Ag}^{2+}$  hole center. The values do support the assignment of “perturbed” and “unperturbed” labels. The unperturbed center is posited to be a substitutional ion, i.e., a silver ion that sits at a lithium site in the crystal. Since silver is a dopant and similar to lithium in that it has a single unpaired electron in its outer shell, it would appear statistically favorable to be a substitutional ion with no neighboring defect. This is explained by the higher signal intensity of the unperturbed center relative to the perturbed center in the EPR spectra. The perturbed center, with its lower signal intensity and population, would then be likely to have a neighboring defect. This perspective is reinforced with the hyperfine parameters determined for the perturbed  $\text{Ag}^{2+}$  hole center,



since they are lower than the hyperfine parameters of the unperturbed  $\text{Ag}^{2+}$  hole center. If a hole is trapped on a silver ion with a neighboring monovalent silver ion, smaller hyperfine values appear appropriate. It has also been suggested [51] that this perturbation is due to  $\text{Na}^+$  ions occupying adjacent substitutional lithium sites. This suggestion is based upon neutron activation results that showed concentrations of sodium present in LTB crystals (those used in the present study) with intentionally large concentrations of silver [31]. Sodium ions could cause a slight perturbation to the  $g$  and hyperfine values, perhaps with no other effect on the spectra, i.e., further splitting due to nuclear spin interactions from sodium. Also, although unlikely, this nearest silver could be an interstitial monovalent silver ion that is responsible for the  $\text{Ag}^0$  electron center seen in the EPR spectra of x-ray irradiated crystals.

Future research can help determine the impact of these defects, and techniques can be developed to reduce or magnify the defect density dependent upon its usefulness in a given application. Currently, copper appears in the literature as the preferred dopant candidate in lithium tetraborate but the work done by Brant et al. [51] and this latest research effort has shown silver-doped lithium tetraborate to be a strong candidate for dosimetry. The perturbed and unperturbed  $\text{Ag}^{2+}$  hole centers appear to recombine with electrons from the electron center that was previously identified. This recombination explains the strong thermoluminescent peak that is produced when x-ray irradiated silver-doped lithium tetraborate is heated above room temperature. This research provides the explanation for the thermoluminescent curve. The advantage silver appears to have as a dopant versus copper in lithium tetraborate is that silver-doped lithium tetraborate has only one thermoluminescent peak, whereas copper-doped lithium tetraborate has two

peaks. This chapter has been the final set of characterization needed to explain the defect sites responsible for electron-hole recombination in lithium tetraborate doped with silver.

## **V. Identification of Radiation-Induced Point Defects in Copper-Doped Lithium Tetraborate Crystals**

### **5.1. Introduction**

Transition metals ions have been doped into lithium tetraborate crystals for their light emitting properties [60-62]. Specifically, copper, manganese, and silver have been the subject of numerous studies [63-70]. These controlled dopants have been shown to be highly efficient with respect to their radiative emissions. Copper-doped LTB has been the subject of an EPR investigation in the literature. Corradi et al. [71] fully characterized a  $\text{Cu}^{2+}$  trapped hole center by performing a complete angular dependence study from which the parameters for the  $g$  and hyperfine matrices were determined. This hole center was modeled as an  $S = 1/2$  hole trapped on a copper ion substituting for a lithium ion and stabilized by a neighboring lithium vacancy, thus creating a  $\text{Cu}^{2+}$  hole center. This center investigated by Corradi et al. will be referred to as the  $\text{Cu}^{2+}\text{-V}_{\text{Li}}$  hole center.

Unlike silver-doped crystals where there are no  $\text{Ag}^{2+}$  centers prior to x-ray irradiation, copper-doped LTB has the  $\text{Cu}^{2+}\text{-V}_{\text{Li}}$  hole center always present, i.e., room temperature x rays are not required to populate the  $\text{Cu}^{2+}\text{-V}_{\text{Li}}$  hole center. The EPR signal from the  $\text{Cu}^{2+}\text{-V}_{\text{Li}}$  hole center has a significant magnitude without x-ray exposure, and is comparable to the magnitude of the  $\text{Ag}^{2+}$  hole centers in silver-doped LTB after x-ray exposure. An initial goal of this study was to verify the spin Hamiltonian parameters determined by Corradi et al. [71] for the  $\text{Cu}^{2+}\text{-V}_{\text{Li}}$  hole center. However, before data collection began, the LTB crystal was exposed to x rays to further magnify and populate the  $\text{Cu}^{2+}\text{-V}_{\text{Li}}$  hole center and a new effect was observed that changed the scope of this

investigation. Surprisingly, x-ray exposure did not increase the signal intensity of the  $\text{Cu}^{2+}\text{-V}_{\text{Li}}$  hole center, but rather created several new spectra that have not been previously reported in the literature. Thus, this investigation has focused on two new trapped electron centers and two new trapped hole centers. Their identification and characterization are the subject of this chapter. The two electron centers have isotropic EPR spectra. The spectrum from one hole center continuously overlaps the  $\text{Cu}^{2+}\text{-V}_{\text{Li}}$  hole center and a second (low concentration) “hole” center has little angular dependence. This second low concentration hole center was not investigated in depth in this dissertation. After an analysis of the copper-related EPR spectra, this study continued with an investigation of the thermal stability of the copper defects. It is shown that the x-ray-induced electron and hole centers recombine at temperatures that correspond to thermoluminescence glow curve peak positions reported in the literature [68, 70, 72].

## **5.2. X-Ray-Induced Electron Centers in Copper-Doped LTB**

The spectra of the two electron centers partially overlap making identification difficult but not impossible. These electron centers are the result of  $\text{Cu}^+$  interstitial ions trapping an electron during irradiation. The trapped electron converts the interstitial  $\text{Cu}^+$  ( $3d^{10}$ ) ions into  $\text{Cu}^0$  ( $3d^{10}4s^1$ ) atoms. The two x-ray-induced electron centers have large hyperfine parameters. The large hyperfine is due to the interaction between the  $S = 1/2$  unpaired electron and the copper nucleus. Calculations published by Morton and Preston [74-75] predict a large hyperfine constant for copper nuclei. The electron center spectra are described in this section along with support for this defect model.

Prior to x-ray irradiation, the EPR spectrum of copper-doped lithium tetraborate

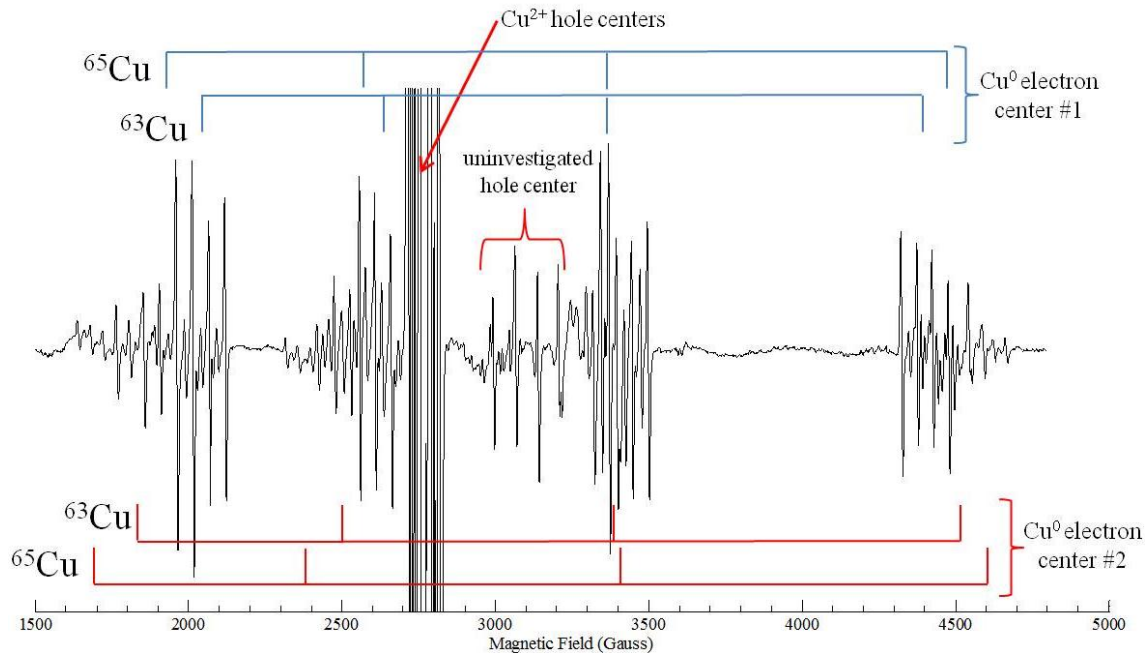


Fig. 5.1. EPR spectrum of x-ray irradiated copper-doped lithium tetraborate. This spectrum was taken at 45 K with the magnetic field along the [001] direction.

consists of a set of EPR transitions in the 2700 to 2850 Gauss range representing the  $\text{Cu}^{2+}\text{-V}_{\text{Li}}$  hole center reported by Corradi et al. [71] After x ray exposure, two new EPR spectra are present. These two spectra consist of four widely separated sets of lines and represent the two electron centers. These spectra with their multiple lines are due to two similar, yet different,  $\text{Cu}^0$  electron centers in the LTB crystal. The spectrum shown in Fig. 5.1 was taken after a one hour exposure to x-ray irradiation produced by a rotating anode x-ray tube. The  $\text{Cu}^{2+}\text{-V}_{\text{Li}}$  hole center and a second hole center, discussed in more detail later in this chapter, extend off-scale in the figure due to the EPR spectrometer settings used to optimize the signal of the electron centers. The two  $\text{Cu}^0$  electron centers are identified and labeled as  $\text{Cu}^0$  electron centers #1 and #2. These two centers, representing two different defects, can be grouped into sets of four transitions because of

the two isotopes of copper. The stick diagrams for each center designate the mid-points of the transition sets for each isotope. Copper has two isotopes,  $^{65}\text{Cu}$  and  $^{63}\text{Cu}$ , that have relative abundances of 30.8% and 69.2%, respectively. They possess similar magnetic moments with a ratio of  $^{65}\text{Cu}$  to  $^{63}\text{Cu}$  being 1.070 and both have a nuclear spin of  $I = 3/2$ . As mentioned earlier, copper atoms with their  $3d^{10}4s^1$  configuration are expected to have very large hyperfine interactions. These properties will be used to explain the spectra resulting from the  $\text{Cu}^0$  electron centers.

The energy level diagrams presented in this dissertation, so far, have been made with the assumption that the electron Zeeman term of the spin Hamiltonian has a much larger contribution than the hyperfine term, or any other term. From this assumption the effective  $g$ , or  $g_{\text{eff}}$ , can be calculated by using the mid-point of a set of EPR transitions. For example, in Chapter Three, a  $g_{\text{eff}}$  could be calculated from the center of the seven peak spectrum presented in Fig. 3.2(a). This is not the case for the  $\text{Cu}^0$  electron centers; their effective  $g$  value corresponds to a lower magnetic field value than the mid-point of the spectrum. The spin Hamiltonian for the copper electron centers are the same as any  $S = 1/2$  electron interacting with an  $I = 3/2$  nucleus, with the exception that the hyperfine parameter,  $A$ , will have a significant contribution to the energy levels. This behavior is described in Appendix C of the book “*Electron Paramagnetic Resonance*” by John Weil and James Bolton. [25] The resulting equations for the energies of a spin Hamiltonian are dependent upon the magnitude of the applied magnetic field. The equations for these energy levels are called the ‘Breit-Rabi’ formulas. A Breit-Rabi energy level diagram of an electron of spin  $S = 1/2$  interacting with a nucleus of spin  $I = 3/2$  is illustrated in Fig.5.2. The Breit-Rabi formulas predict the changes in an EPR spectrum when the

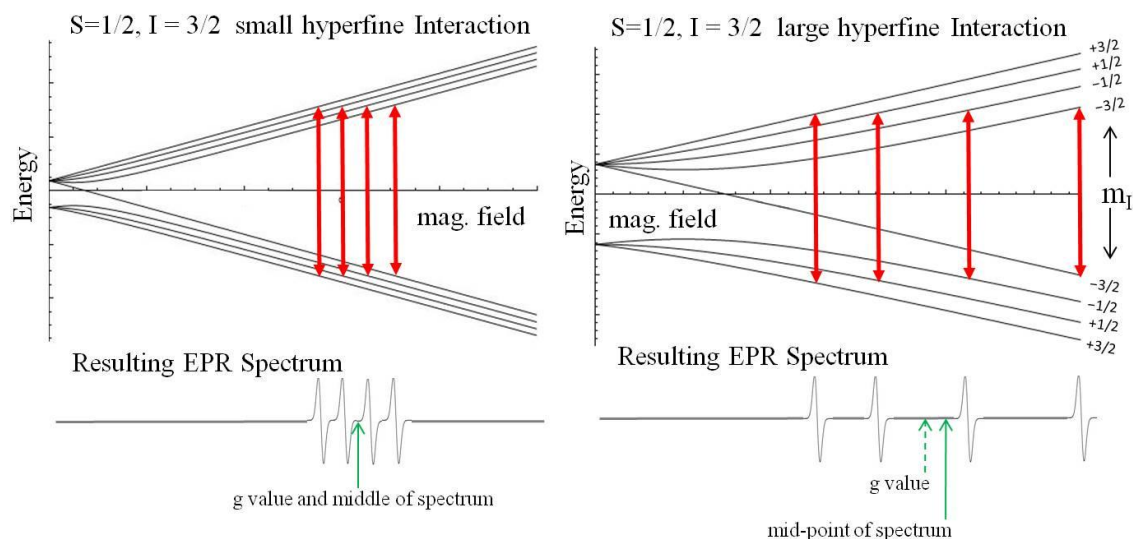


Fig 5.2. Breit-Rabi energy level diagrams illustrating the interaction of an  $S = 1/2$  electron spin interacting with an  $I = 3/2$  nuclear spin. (Left) Energy level diagram demonstrating a small hyperfine interaction. (Right) Energy level diagram demonstrating a large hyperfine interaction.

hyperfine interaction becomes progressively larger. A symmetric EPR spectrum is produced when the electron Zeeman term is considerably larger than the hyperfine term. Conversely, an asymmetric EPR spectrum is produced when the hyperfine term approaches the electron Zeeman term. These effects are shown in Fig. 5.2. The red double headed arrows represent the constant energy ( $\Delta E = h\nu$ ) provided by the microwaves in an EPR experiment. It may be deceptive, but the arrows are all the same length. The left portion of Fig. 5.2 illustrates the positions of EPR transitions, and the resulting EPR spectrum that occurs, when there is only a small contribution from the hyperfine term of the spin Hamiltonian. The right hand portion of Fig. 5.2 illustrates the positions of EPR transitions, and the resulting EPR spectrum that occurs, when there is a large contribution

from the hyperfine term of the spin Hamiltonian. The large hyperfine value of copper and the Breit-Rabi energy level diagram of Fig. 5.2 thus explain the relative spacings of the sets of transitions in the EPR spectrum in Fig. 5.1 for the  $\text{Cu}^0$  electron centers.

The  $\text{Cu}^0$  electron centers are complex and thus difficult to describe. Each center is the result of an unpaired  $s$  shell electron interacting with its copper nucleus of spin  $I = 3/2$ . This causes the spectrum to split into four groups of spectra that have a spacing described by the Breit-Rabi formulas. If there were no other interactions than this, a resulting four peak spectrum would be seen. This is not the case. Each of the four splittings from the copper interaction is further split by an interaction with a boron nucleus. Boron has two isotopes ( $^{10}\text{B}$  and  $^{11}\text{B}$ ) that have different nuclear spins ( $I = 3$  and  $I = 3/2$ , respectively) and different abundances (19.8% and 80.2%, also respectively). Since hyperfine-split signals associated with the  $^{11}\text{B}$  nuclei will be more intense because of the higher abundance of this isotope, these  $^{11}\text{B}$  lines will be used to describe the four groups of EPR spectra of the  $\text{Cu}^0$  electron centers. Each  $\text{Cu}^0$  electron center “group” is split by an adjacent interacting boron ion, which is called a superhyperfine interaction.  $^{11}\text{B}$  (with  $I = 3/2$ ) will cause a Cu EPR transition to separate into four EPR lines. As mentioned earlier, copper has two isotopes with similar magnetic moments.  $^{65}\text{Cu}$  has a larger magnetic moment and thus has four wider spaced  $\text{Cu}^0$  electron center groups than those groups associated with  $^{63}\text{Cu}$ . With their similar magnetic moments, the groups from the two isotopes overlap.

A diagram illustrating the spectral splittings of  $\text{Cu}^0$  electron center #1 that takes both copper isotopes into account is shown in Fig. 5.3. Starting from the top of the figure, an  $S = 1/2$  spin system, is represented interacting with each copper isotope. Each



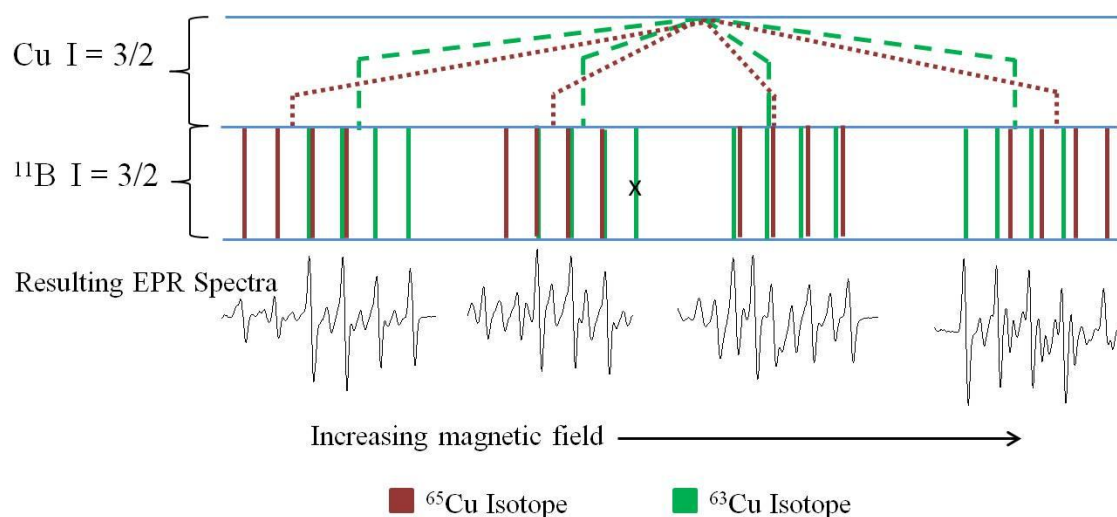


Fig 5.3. Diagram illustrating the spectral splittings of Cu<sup>0</sup> electron center #1 taking both isotopes into account and the superhyperfine splitting from a <sup>11</sup>B nucleus.

isotope (both with  $I = 3/2$ ) splits the transition into four sets (four for each isotope) shown with short brown dashes for <sup>65</sup>Cu and long green dashes for <sup>63</sup>Cu. Each of these sets is shown interacting with a <sup>11</sup>B nucleus that splits each set into four transitions, shown again in solid brown for <sup>65</sup>Cu and solid green for <sup>63</sup>Cu. The four transitions are then spaced appropriately for their magnetic moments. When two transitions are close together, they tend to “add” up to a larger single transition in an actual EPR spectrum. The resulting experimental spectra, shown in the lower portion of the figure, represent the groups of lines associated with Cu<sup>0</sup> electron center #1 and were taken from Fig. 5.1. The transition labeled with an “x” is not shown because it is covered by the spectra from the hole centers. The experimental EPR spectra in Fig. 5.3 have more transitions than the ones described above and labeled in the figure. These additional transitions arise from <sup>10</sup>B interactions as well as the Cu<sup>0</sup> electron center #2.

There are several ways to verify that the correct assignments have been made for

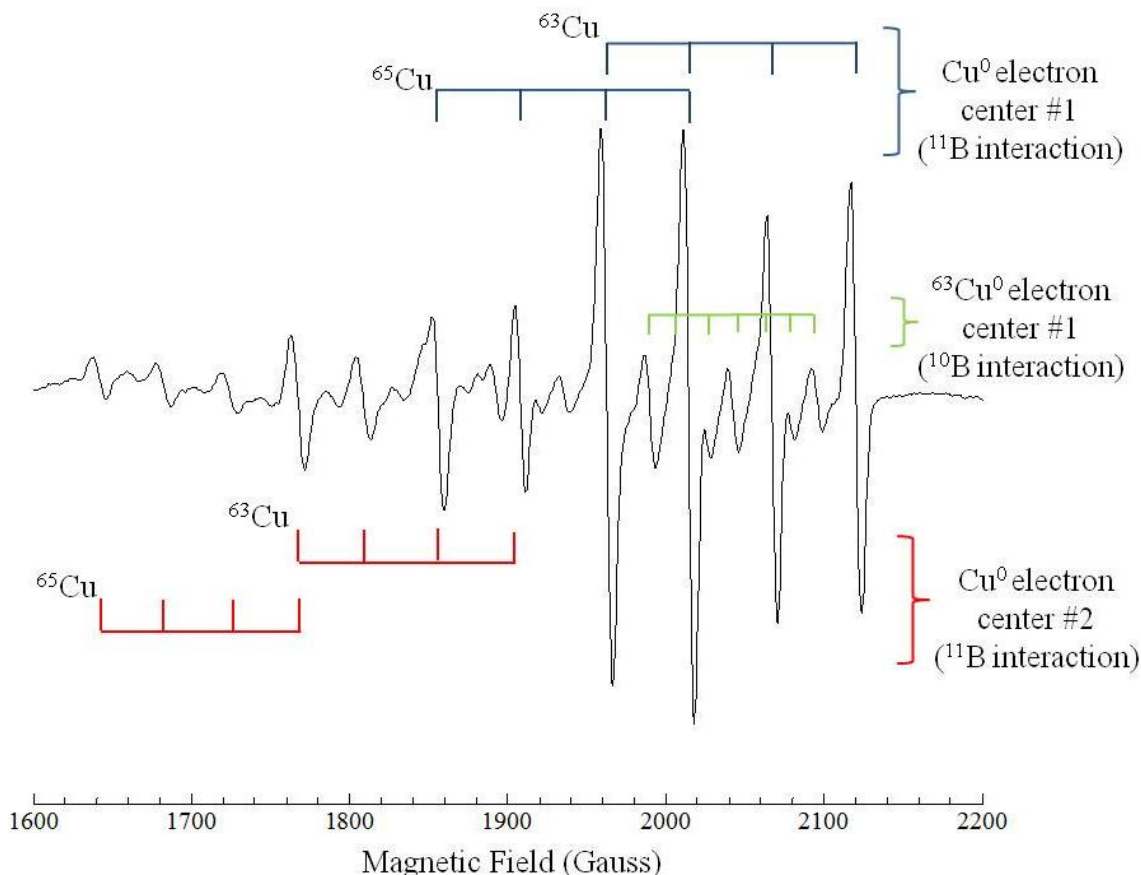


Fig. 5.4. Expanded view of the lowest “group” of lines for the two Cu<sup>0</sup> electron centers. The stick diagrams indicate the four <sup>11</sup>B superhyperfine lines for the two Cu isotopes in each center. A single set of <sup>10</sup>B superhyperfine lines is shown for electron center #1 and its associated <sup>63</sup>Cu isotope.

the Cu<sup>0</sup> electron centers. Again, focus will be given to the lower group of lines in the 1600 to 2200 Gauss magnetic field range for the two Cu<sup>0</sup> electron centers, shown in Fig. 5.4. The two peaks on the far right hand side of the figure at 2096 and 2120 Gauss have intensities (taken from the experimental spectrum) of 2.53 and 17.34 units, respectively, in height. These two peaks represent <sup>10</sup>B and <sup>11</sup>B ion interactions for the <sup>63</sup>Cu isotope. Multiplying 17.34 units by 4 (<sup>11</sup>B with  $I = 3/2$  results in four spectral peaks) equals 69.36

units. This represents the total magnitude of transitions within this set that are due to  $^{11}\text{B}$ . Next, multiplying 2.53 units by 7 ( $^{10}\text{B}$  with  $I = 3$  results in seven spectral peaks) equals 17.71 units and represents the total magnitude of transitions within this set that are due to  $^{10}\text{B}$ . Dividing the  $^{10}\text{B}$  natural abundance (19.8%) by the  $^{11}\text{B}$  natural abundance (80.2%) gives a ratio of 0.2469. Finally, dividing 17.71 units by 69.36 units gives a ratio of 0.2553 and is very close to boron's natural abundance ratio. Carrying out a similar comparison for a single  $^{63}\text{Cu}$  peak intensity to that of a single  $^{65}\text{Cu}$  peak intensity yielded a ratio of 0.4266 that is also in good agreement with the 0.4451 ratio of the two natural abundances for copper.

Recall from Chapter Two that EPR transitions are separated by their hyperfine parameters and that those hyperfine values are also directly proportional to their magnetic moments. This allows for a comparison of the spacing between the seven  $^{10}\text{B}$  transitions and the four  $^{11}\text{B}$  hyperfine transitions associated with the  $^{63}\text{Cu}^0$  portion of electron center #1. The spacing between adjacent lines, or the  $A$  value, for the  $^{11}\text{B}$  interaction is measured to be 52.33 Gauss. Likewise, the spacing between adjacent lines, or the  $A$  value, for the  $^{10}\text{B}$  hyperfine interaction is measured to be 17.67 Gauss. The ratio of  $^{10}\text{B}$  hyperfine (or  $A$  value) to  $^{11}\text{B}$  hyperfine is 0.3376 and is in excellent agreement with the ratio of the two magnetic moments of boron, or 0.3347. Comparing the hyperfine in this manner works as long as the hyperfine parameter does not significantly affect the overall energy of the spin Hamiltonian. The hyperfine of copper has a significant effect on the overall energy of the spin Hamiltonian.

Because the  $\text{Cu}^0$  electron centers are isotropic, data taken with the magnetic field aligned parallel to the  $c$  axis of the crystal was used to determine the  $g$  parameters. A

least-squares fitting routine, similar to those used in earlier chapters of this dissertation, was used to solve for the  $g$  value. Only one set of data (magnetic field values and microwave frequencies) is needed. Since the defect model places the electron in an  $s$  orbital, the experimentally measured  $g$  should be very close to  $g_e$ , the  $g$  value of a free electron. Indeed, this is the case, since both electron centers (#1 and #2) have a  $g$  value of  $2.0023 \pm 0.0005$ , as determined in the least-squares fitting routine. The error was estimated by using the line widths of the EPR spectra.

At the same time, the hyperfine parameters were determined for the electron centers. This is not a straight forward calculation as in earlier chapters due to the uneven spacings of the EPR transitions that are due to the large hyperfine interaction. John Weil has a paper titled “The Analysis of Large Hyperfine Splitting in Paramagnetic Resonance Spectroscopy” [73]. This paper starts with an isotropic spin Hamiltonian and can be used with hyperfine values that are not “too large.” In his derivation, Weil arrives at the following equation:

$$\frac{B_{-m_I} - B_{m_I}}{2 m_I} = \frac{\frac{A_{iso}}{g_{iso}\beta}}{1 - \left(\frac{A_{iso}}{2h\nu}\right)^2} \quad 5.1$$

In the above equation,  $B_{-m_I} - B_{m_I}$ , is the magnetic field position corresponding to a specific nuclear transition ( $m_I$ ). It may help to look back at the four EPR transitions shown for the right side of Fig. 5.2. These four transitions go with specific values of  $m_I$ . Also in Eq. 5.1,  $A_{iso}$  represents the isotropic hyperfine parameter, and  $g_{iso}$  is the isotropic value calculated in the preceding paragraph. Using the magnetic field positions of the midpoints of the sets of transitions for each  $\text{Cu}^0$  center and each isotope of copper,  $A_{iso}$  could be determined for each isotope. For clarity, the magnetic field positions that were

used to solve for the hyperfine values of each isotope are shown in Fig. 5.1 (i.e., the vertical lines in the stick diagrams above and below the spectra for electron centers #1 and #2). The values of the hyperfine parameters for the two electron centers are listed in Table 5.1.

Table 5.1. Isotropic spin-Hamiltonian parameters for  $\text{Cu}^0$  electron centers #1 and #2.

These values were obtained from the EPR spectra in Fig. 5.1. Estimated error limits are  $\pm 0.0005$  for the  $g$  values and  $\pm 15$  MHz for the  $A$  values.

Defect	$g$	$A(^{63}\text{Cu})$	$A(^{65}\text{Cu})$
$\text{Cu}^0$ #1	2.0023	2480 MHz	2663 MHz
$\text{Cu}^0$ #2	2.0023	2178 MHz	2333 MHz

The two defects are very similar and defect models to support the differences in the centers would be difficult to establish. The superhyperfine interaction with boron strongly suggests a model in which these electron centers are interstitial copper atoms. One of these two defects could be the result of an interstitial copper that is isolated from any other defects, while the second defect is the result of an interstitial copper with a nearby defect that “slightly” changes the hyperfine parameter. The  $g$  parameter is the same for both centers because the unpaired spin is in an  $s$  orbital and thus has no orbital angular momentum. There is a table provided by Morton and Preston [74-75] that predicts the isotropic hyperfine constant for each element in the periodic table. Their prediction for  $^{65}\text{Cu}$  is 6410 MHz. The average hyperfine for the two electron centers

containing  $^{65}\text{Cu}$  is 2498 MHz. This means that 39% of the unpaired spin is in a 4s orbital and the remaining spin density resides elsewhere, such as on the neighboring boron nucleus, as illustrated in Fig. 5.1 where the spin of the electron is split by an interacting boron nucleus. This large spin density residing on the boron ion is further evidence to support the model that these two electron centers are interstitial copper atoms. If a copper atom were occupying a lithium site, a smaller interaction with the neighboring substitutional boron would be expected because of the large separation distance of about 2.7 Å from a lithium site to the nearest boron lattice site.

### 5.3. X-Ray-Induced Hole Centers in Copper-Doped LTB

As-grown copper-doped lithium tetraborate crystals contain a large signal due to  $\text{Cu}^{2+}$  ions that has been reported in the literature, labeled  $\text{Cu}^{2+}\text{-V}_{\text{Li}}$ . This was the only EPR signal observed in as-grown crystals. After exposure to x-rays, a radiation-induced  $\text{Cu}^{2+}$  hole center signal is present and its EPR spectrum overlaps the spectrum assigned to the  $\text{Cu}^{2+}\text{-V}_{\text{Li}}$  center. Significant overlap occurs for every orientation of magnetic field. This radiation-induced  $\text{Cu}^{2+}$  hole center, henceforth referred to as the  $\text{Cu}^{2+}$ -active center, is best observed when the magnetic field is oriented parallel to the crystal [110] direction. Recall that the basic  $\text{B}_4\text{O}_9^{6-}$  unit in lithium tetraborate has eight crystallographic orientations in the LTB crystal lattice and a paramagnetic defect would have an equivalent set of eight crystallographic orientations. When the magnetic field is aligned parallel to the  $c$  axis of the crystal all eight defect sites are magnetically equivalent and produce a single EPR spectrum. However, when the magnetic field is aligned parallel to

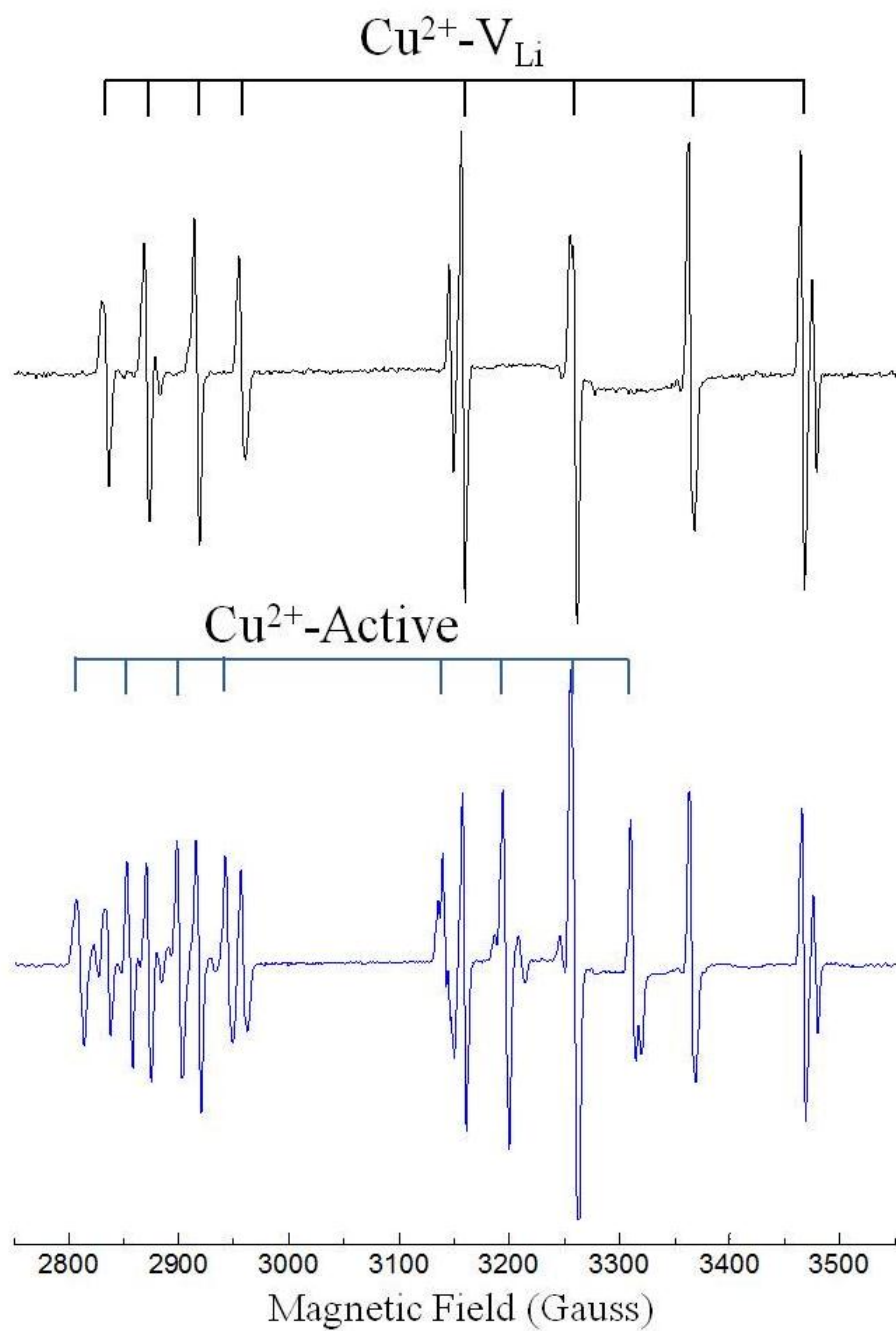


Fig. 5.5. Upper EPR spectrum showing the  $\text{Cu}^{2+}\text{-V}_{\text{Li}}$  characterized by Corradi et al. [71]. Lower EPR spectrum showing both the  $\text{Cu}^{2+}\text{-V}_{\text{Li}}$  center and the radiation induced  $\text{Cu}^{2+}\text{-Active}$  center after irradiation. These spectra were taken at 25 K with the magnetic field parallel to the crystal [110] direction.

the  $a$  axis or the crystal  $[110]$  direction, the eight sites separate into two magnetically inequivalent sets, each with fourfold degeneracy. The two magnetically inequivalent sets are identified and labeled in Fig. 5.5 for both  $\text{Cu}^{2+}\text{-V}_{\text{Li}}$  and  $\text{Cu}^{2+}$ -active centers.

The EPR spectra of the  $\text{Cu}^{2+}$  hole centers, with their sets of four equally spaced lines, are the result of an  $S = 1/2$  spin interacting with a copper ( $I = 3/2$ ) nucleus. This interaction results in a four-peak spectrum that is best seen in the upper portion of Fig. 5.5 for the four peaks between 2800 and 3000 Gauss. Since  $^{65}\text{Cu}$  has a larger magnetic moment than  $^{63}\text{Cu}$ , the outer lines associated with the different isotopes within a set of four lines often do not overlap at higher fields. This is best seen in the upper portion of Fig. 5.5 for the peaks between 3100 and 3500 Gauss. The outer most peaks in this upper set are due solely to  $^{65}\text{Cu}$  and the peaks next to each of these are due solely to  $^{63}\text{Cu}$ . The middle two peaks in this set are overlapping peaks due to the presence of both copper isotopes and this explains their misshapen nature, i.e., there are actually two overlapping lines at each location. In the lower set of peaks between 2800 and 3000 Gauss, the lines due to both isotopes are all overlapping. This overlap results in broadened peaks and the individual isotopes are not resolved. The lower portion of Fig. 5.5 contains the lines of the  $\text{Cu}^{2+}\text{-V}_{\text{Li}}$  center plus additional lines from the  $\text{Cu}^{2+}$ -active center. This “active” center has been given this name because it appears during irradiation and disappears after irradiation when the temperature is increased (when this hole center recombines with the electron centers #1 and #2). The EPR signal intensity (i.e., concentration) of the  $\text{Cu}^{2+}\text{-V}_{\text{Li}}$  center does not change during an annealing process and thus do not “actively” participate in electron-hole recombination. This will be discussed further in the thermal stability section of this chapter.



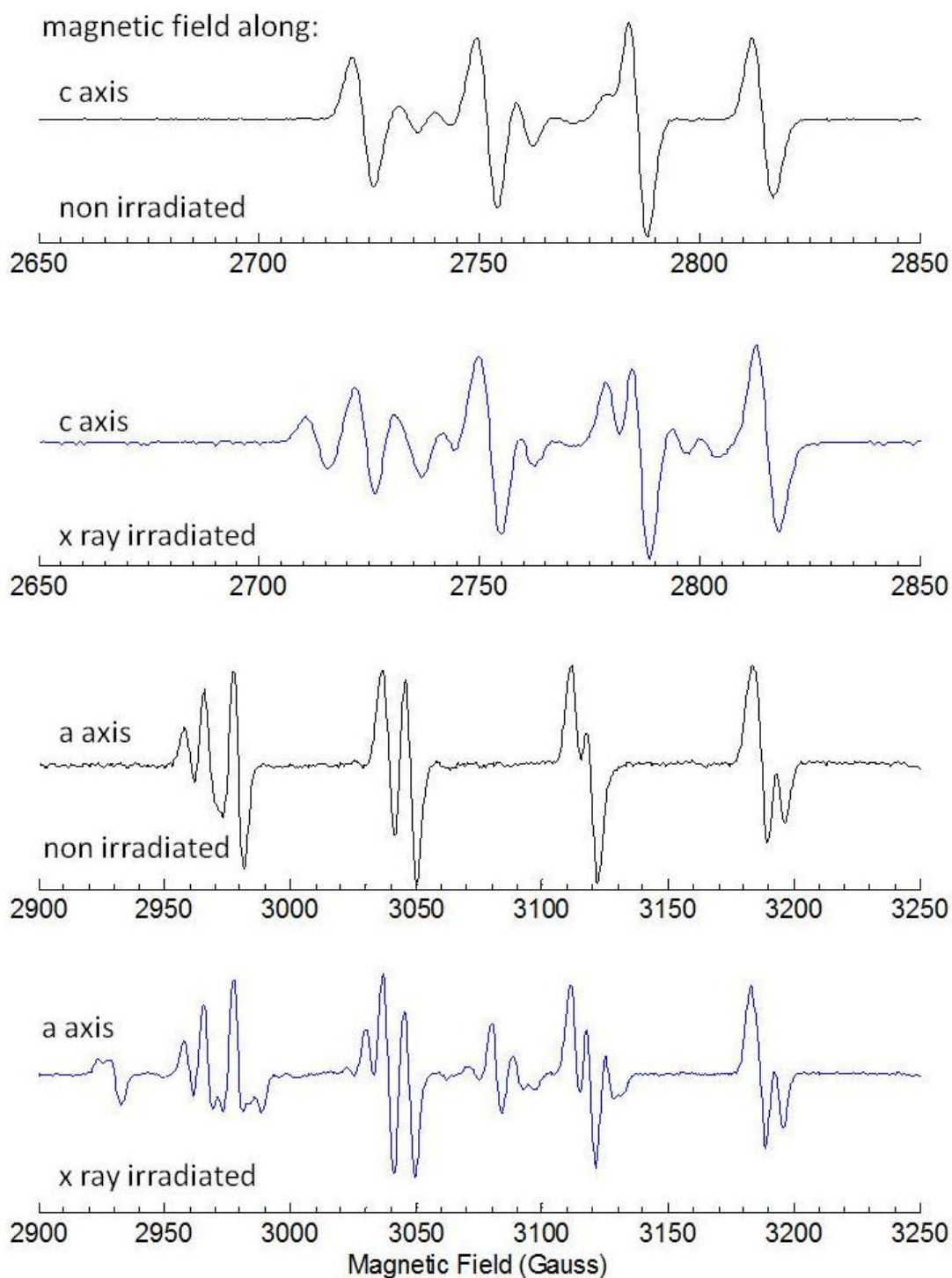


Fig. 5.6. EPR spectra of the  $\text{Cu}^{2+}\text{-V}_{\text{Li}}$  and  $\text{Cu}^{2+}$ -active centers. Spectra taken before and after irradiation are compared. These data were taken at 25 K. The non-irradiated spectra contain the  $\text{Cu}^{2+}\text{-V}_{\text{Li}}$  center alone. The  $\text{Cu}^{2+}$ -active center is present in the irradiated spectra, but difficult to identify.

A set of spin-Hamiltonian parameters describing the  $\text{Cu}^{2+}$ -active center was not obtained in the current study due to the strong overlap with the  $\text{Cu}^{2+}\text{-V}_{\text{Li}}$  center. The EPR spectrum of the “active” center is best observed when the magnetic field is oriented parallel to the crystal [110] direction. The overlap between the two spectra is even more extreme for other high symmetry directions. This overlapping nature is illustrated in Fig. 5.6, where spectra are shown for the magnetic field oriented along the crystal  $a$  and  $c$  directions. In both cases, a full set of  $\text{Cu}^{2+}$ -active center peaks cannot be identified. Though not shown, the spectra were observed at many orientations of magnetic field relative to the crystal, and overlapped in all cases. This leads to the conclusion that this radiation induced  $\text{Cu}^{2+}$ -active center has a set of spin Hamiltonian parameters that are close to those published by Corradi et al. [71] for the  $\text{Cu}^{2+}\text{-V}_{\text{Li}}$  center, and thus is a similar defect. The  $\text{Cu}^{2+}$ -active center is likely a  $\text{Cu}^{2+}$  ion sitting at a  $\text{Li}^+$  substitutional site that does not have a neighboring  $\text{Li}^+$  vacancy stabilizing the hole as put forward for the  $\text{Cu}^{2+}\text{-V}_{\text{Li}}$  center.

There are two additional items concerning hole centers in copper-doped lithium tetraborate that need elaboration. First, as shown in Fig. 5.1, there is a less intense hole center located between 2950 and 3300 Gauss that is produced by x-ray radiation. It is clearly associated with copper as the outer lines show the typical copper  $^{63}\text{Cu}/^{65}\text{Cu}$  splitting. However, its concentration is much less than that of the  $\text{Cu}^{2+}\text{-V}_{\text{Li}}$  and  $\text{Cu}^{2+}$ -active centers and is not investigated in any detail. This “small” Cu-related center did not appear to contribute additional information to the present study. Second, while performing the EPR experiments on copper-doped lithium tetraborate and viewing the spectra along many magnetic field orientations, it was observed that the hyperfine

splittings for the  $\text{Cu}^{2+}\text{-V}_{\text{Li}}$  center reduced to zero for a few orientations of magnetic field. Corradi et al. [71] published hyperfine parameters of  $-16.1$ ,  $-57.5$ , and  $97.6$  MHz for the  $\text{Cu}^{2+}\text{-V}_{\text{Li}}$  center. The observation that the hyperfine decreases to zero at some angles provides evidence that the hyperfine parameters do not all have the same sign. When hyperfine parameters are either all positive or all negative, the hyperfine splitting cannot reduce to zero. This is the case for the hyperfine in silver-doped lithium tetraborate crystals where there is always an observable hyperfine splitting and it has been found that the hyperfine parameters are all positive in sign.

#### **5.4. Thermal Stability of the Radiation-Induced Centers**

After identification of the radiation-induced electron and hole centers, their thermal stabilities were determined. The copper-doped lithium tetraborate crystals were subject to a pulsed isochronal anneal. Crystals were first exposed for one hour with x rays generated by a rotating anode x-ray tube. The subsequent anneal was accomplished by setting an oven to a set temperature, placing the sample in a ceramic boat, and sliding the boat into the center of the oven within a quartz tube that runs through the oven. The sample remained in the center of the oven for two minutes at each temperature. After heating, the sample was quickly removed from the oven. Electron paramagnetic resonance (at 25 K for the hole center and 45 K for the electron centers) was used to determine the defect concentration after each annealing step. The defect concentration was determined by measuring the intensities and line widths of EPR peaks that corresponded to each defect center. The monitored defect centers included the two electron centers, the  $\text{Cu}^{2+}\text{-V}_{\text{Li}}$  center, and the  $\text{Cu}^{2+}$ -active center. The EPR isochronal

pulsed anneal and the thermoluminescence experiments (discussed in the next paragraph) were repeated multiple times to ensure reproducibility.

Thermoluminescence (TL) data were obtained using a Harshaw TLD reader where the resulting glow curves represent total light output versus temperature. The heating rate was 1 °C/s; this is the slowest heating rate available on the instrument. The thermoluminescent glow curve for the copper-doped LTB crystals showed two peaks, one near 100 °C and the other near 200 °C. Thermoluminescent glow curves containing two peaks have been reported for copper-doped lithium tetraborate in the literature [68, 70, 72] and some authors have reported similar two peak TL glow curves for manganese-doped LTB [76-78]. Only one above-room-temperature TL peak has been reported in silver-doped LTB [51].

The results of the EPR isochronal anneal are presented in Fig. 5.7 and are overlaid with the TL glow curve. In the  $\text{Cu}^{2+}$ -active center decay data, two decreasing steps are observed near 100 and 200 °C, respectively. The disappearance of this hole appears to be related to the TL glow peaks. The electron center is different. During the isochronal annealing experiment, the  $\text{Cu}^0$ -electron centers increase in intensity between 25 and 125 °C and then decay entirely between 125 and 225 °C. These data, which were collected on several occasions, suggests that there must be an unidentified electron center that participates in recombination between 25 and 125 °C, at temperatures lower than the decay of the  $\text{Cu}^0$ -electron centers. As this unidentified center releases electrons, some recombine with the  $\text{Cu}^{2+}$ -active center causing its decay and others become trapped at unpopulated  $\text{Cu}^0$ -electron centers thus increasing their signal intensity. In previous work [31], LTB has been shown to have significant concentrations of lithium and oxygen

vacancies. In this earlier work, the oxygen vacancies trapped electrons and could be a possible candidate for the unidentified electron centers.

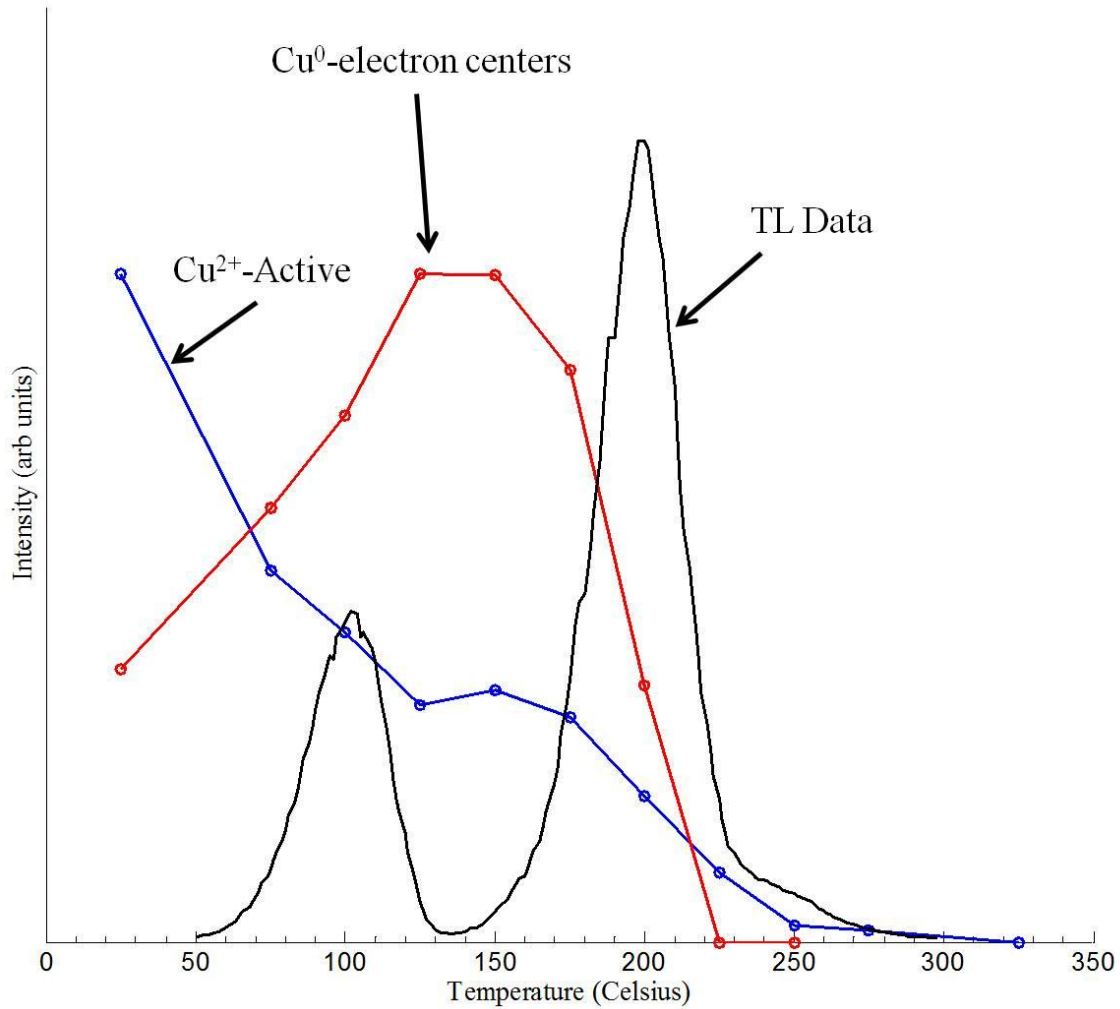


Fig. 5.7. Thermal stabilities of the Cu<sup>2+</sup>-active hole center (blue) and the two Cu<sup>0</sup> electron centers (red), as determined from the magnitudes of their EPR spectra. The data points were obtained by collecting EPR signal intensities at 25 and 45 K, respectively. The effective heating rate during the EPR pulsed anneal experiment was 0.2 °C/s. The thermoluminescence glow curve (black) was obtained by collecting the total light output with a heating rate of 1 °C/s.

## 5.5. Discussion

In the present study, two new trapped electron centers and two new trapped hole centers have been identified after exposing copper-doped lithium tetraborate crystals to x-ray radiation. The electron centers are isotropic and have similar hyperfine parameters. The radiation-induced hole center has  $g$  and hyperfine parameters that are similar to a previously identified hole center [71]. These radiation-induced centers are stable at room temperature and release their trapped electrons and holes as they are warmed above room temperature. The two peaks seen in thermoluminescent glow curves correspond to the two decay steps of the radiation-induced hole center. This research has identified the defects responsible for the TL glow curves and can be beneficial in utilizing copper-doped lithium tetraborate as an x-ray radiation dosimeter. Future work could be done to determine the sensitivity of these crystals to lower magnitude x-ray exposures (i.e., medical x-ray dose levels) furthering their potential in dosimetry applications.

## VI. Optical Properties of Silver-Doped Lithium Tetraborate Crystals

### 6.1. Optical Experiment

Studies concerning the optical properties of lithium tetraborate crystals and glasses can be found in the literature [79-83]. Many of these studies contain absorption, excitation, and emission spectra and offer theoretical explanations. In this chapter, electron paramagnetic resonance (EPR), optical absorption (OA), photoluminescence (PL), and photoluminescence excitation (PLE) data have been collected in an effort to provide a more convincing argument for the optical features observed from silver-doped lithium tetraborate crystals.

Ag-doped LTB crystals are transparent prior to being exposed to x-ray radiation. During exposure, the crystals turn green in color. Crystals will maintain this coloration for about a month, if kept at room temperature. Electron paramagnetic resonance spectra are not present in colorless crystals. This lack of spectra occurs in silver doped crystals because all of the silver impurities are in the form of  $\text{Ag}^+$  ( $3d^{10}$ ) ions in as-grown crystals (including both interstitial and substitutional  $\text{Ag}^+$  ions). In the singly ionized charge state, there is no unpaired spin residing at the silver ion and thus no signal in an EPR spectrum. This behavior has been reported by Brant et al. [51] During exposure to x-ray radiation, the interstitial  $\text{Ag}^+$  ions trap electrons to form  $\text{Ag}^0$  ( $3d^{10}4s^1$ ) atoms and the substitutional  $\text{Ag}^+$  ions trap holes to form  $\text{Ag}^{2+}$  ( $3d^9$ ) ions. Both of these charge states are paramagnetic and results in EPR spectra with very large intensities. EPR spectra identifying the radiation-induced trapped electron and trapped hole centers are shown in Fig. 6.1.

An optical absorption experiment was conducted using a Varian-Cary spectrophotometer. The results, obtained at room temperature, are shown in Fig. 6.2. The red curve shows the absorption spectrum through the visible and near-ultraviolet region for an as-grown LTB crystal.

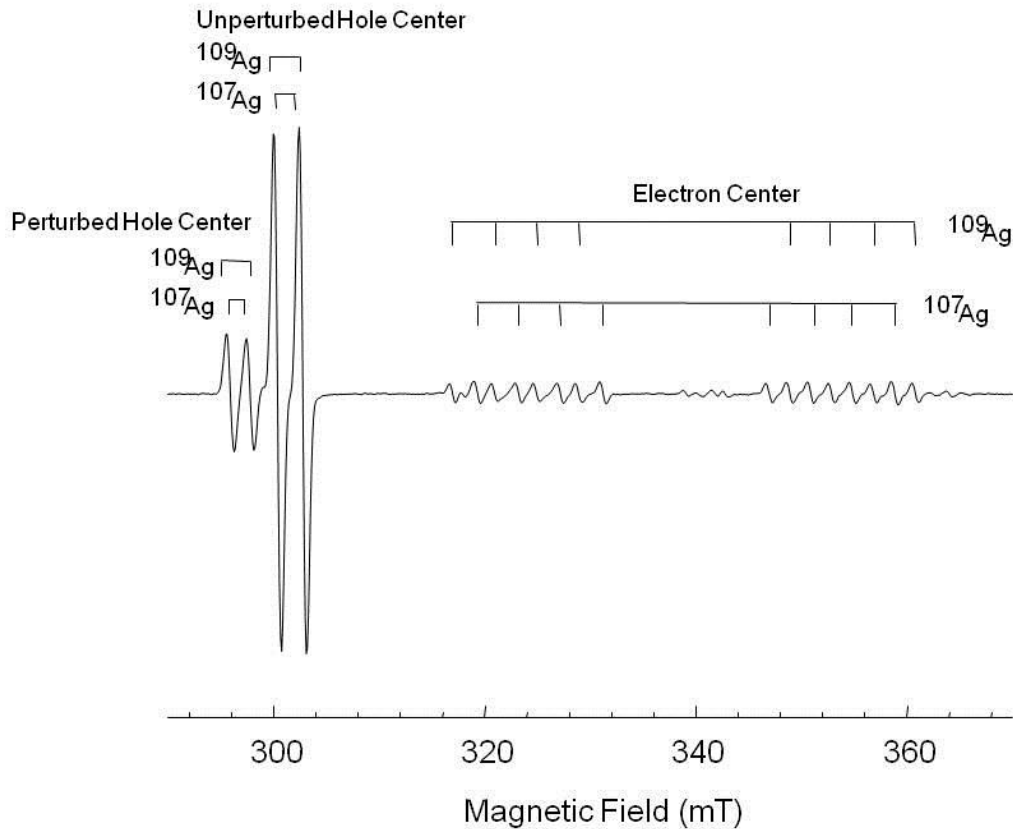


Fig. 6.1. EPR Spectrum illustrating the x-ray radiation induced electron and hole centers.

It contains one band peaking near 205 nm, which has been assigned in the literature to  $\text{Ag}^+$  ions [80]. The black curve in Fig. 6.2 was taken after the crystal was exposed to x rays at room temperature. Several large optical absorption peaks were produced as a result of the x rays. The dominant peak, at 390 nm, has been assigned to  $\text{Ag}^0$  atoms [82-83]. Additional radiation-induced peaks occur at 261, 298, and 650 nm. Interestingly,



the peak at 204 nm decreased in intensity as a result of the x rays. This is in agreement with EPR data where  $\text{Ag}^+$  ions are converted to  $\text{Ag}^0$  and  $\text{Ag}^{2+}$  centers.

Fluorolog experiments (PL and PLE) were conducted on pre- and post- x-ray irradiated Ag-doped LTB crystals. Prior to irradiation, a weak emission peak is observed near 400 nm when using 298 nm light as an excitation source. After irradiation, a much larger (more than 20 times greater) emission peak is observed at 471 nm when using 298 nm light as an excitation source. This latter peak must be due to a defect that was

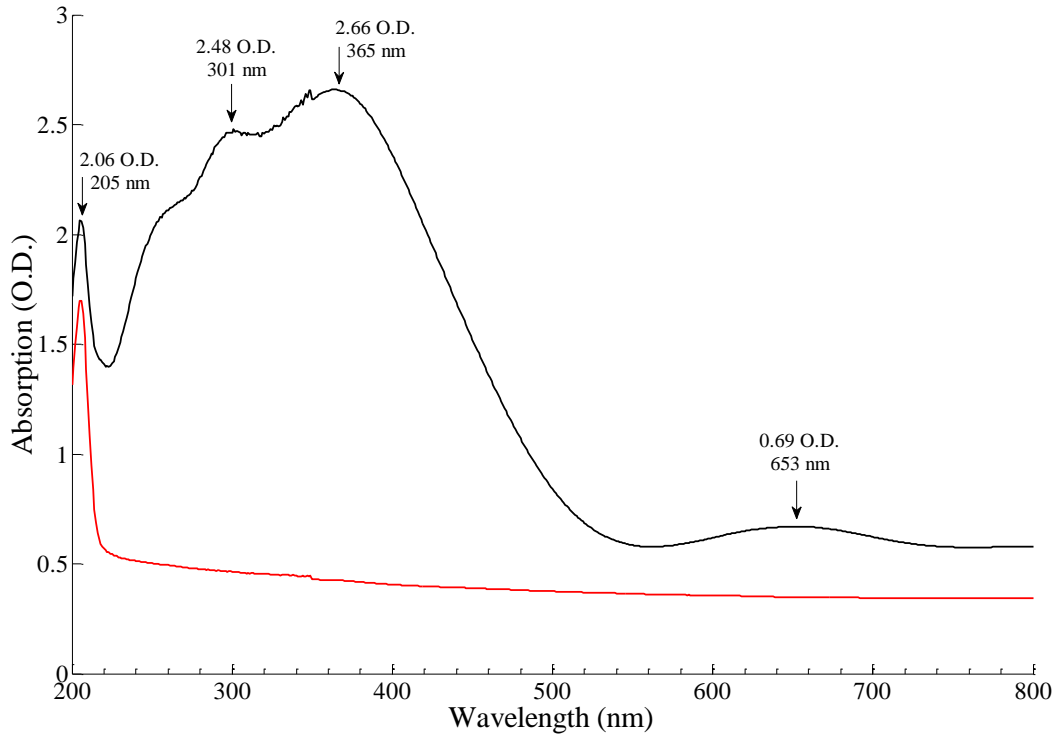


Fig. 6.2. Optical absorption of pre- (red) and post- (black) x-ray irradiated LTB:Ag crystals.

produced by the radiation. The two candidates for this defect are  $\text{Ag}^0$  atoms or  $\text{Ag}^{2+}$  ions (see the EPR spectrum in Fig. 6.1). To determine which defect is responsible for the

intense emission at 471 nm, a photoluminescence excitation experiment was performed. Excitation spectra were collected on pre- and post-x-ray irradiated crystals. Prior to irradiation, there is a small excitation peak near 340 nm when the emission monochromator is set to monitor 471 nm. After the crystals were exposed to x-ray radiation, a very large (more than 20 times greater) excitation peak is observed at 298 nm when the emission monochromator is set to monitor 471 nm. This clearly shows that the 298 nm excitation peak correlates with the 471 nm emission peak. The pre- and post-irradiation emission spectra are shown in Fig. 6.3, and the pre- and post-irradiation excitation spectra are shown in Fig. 6.4. Based on the PLE data, the 471 nm emission peak can now be conclusively assigned to  $\text{Ag}^{2+}$  ions. The  $\text{Ag}^0$  atom is eliminated as a possibility because its broad absorption band at 390 nm does not give rise to the 471 nm emission band. In Fig. 6.5, the optical absorption data from the Varian-Cary spectrophotometer and the PLE data from the Fluorolog are plotted together.

A thermal anneal study was performed for the radiation induced optical absorption spectra. These results are shown in Fig. 6.6. The isochronal annealing procedure was the same as the one used for EPR spectra in Chapter Five. Each step in the anneal consisted of holding the sample at a fixed temperature in the furnace for two minutes. The sample was then cooled and placed in the spectrophotometer. The decrease in the intensity as a function of the annealing temperature correlates with the EPR data previously published by Brant et al. [51]

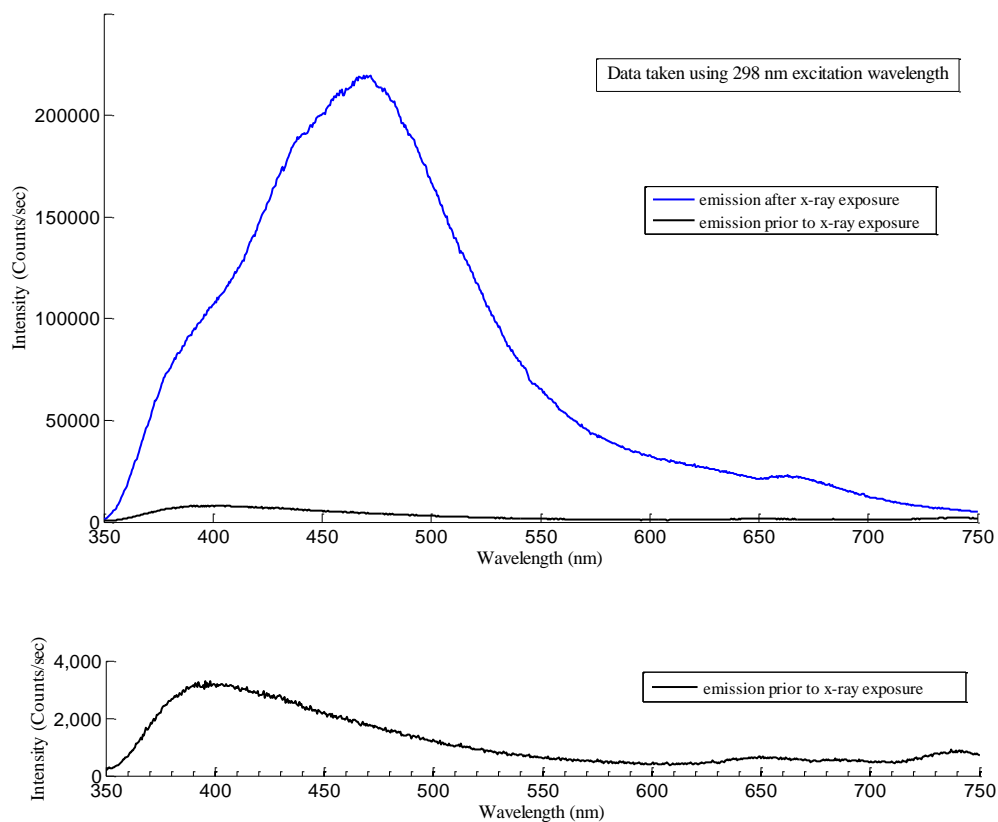


Fig. 6.3. Emission (PL) spectra of pre- and post- x-ray irradiated crystals.

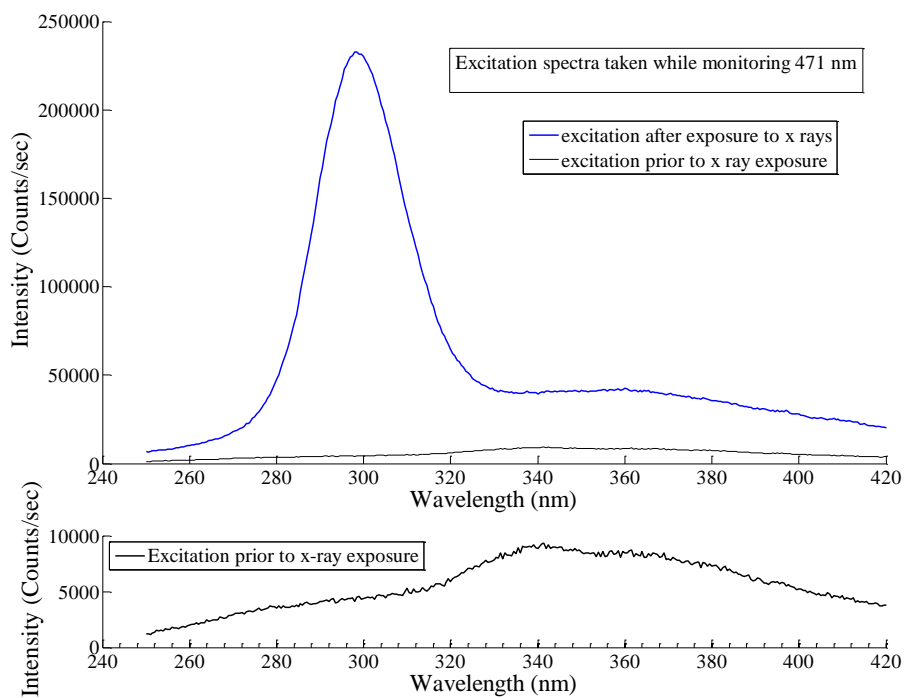


Fig. 6.4. Excitation (PLE) spectra of pre- and post- x-ray irradiated crystals.

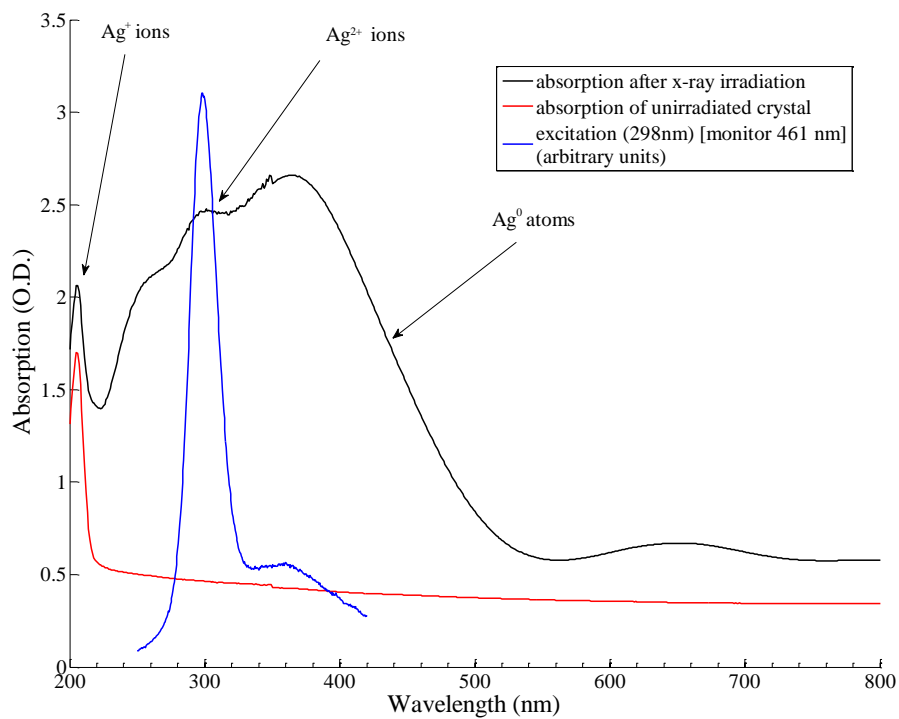


Fig. 6.5. Absorption spectra (black and red) combined with PLE spectra (blue).

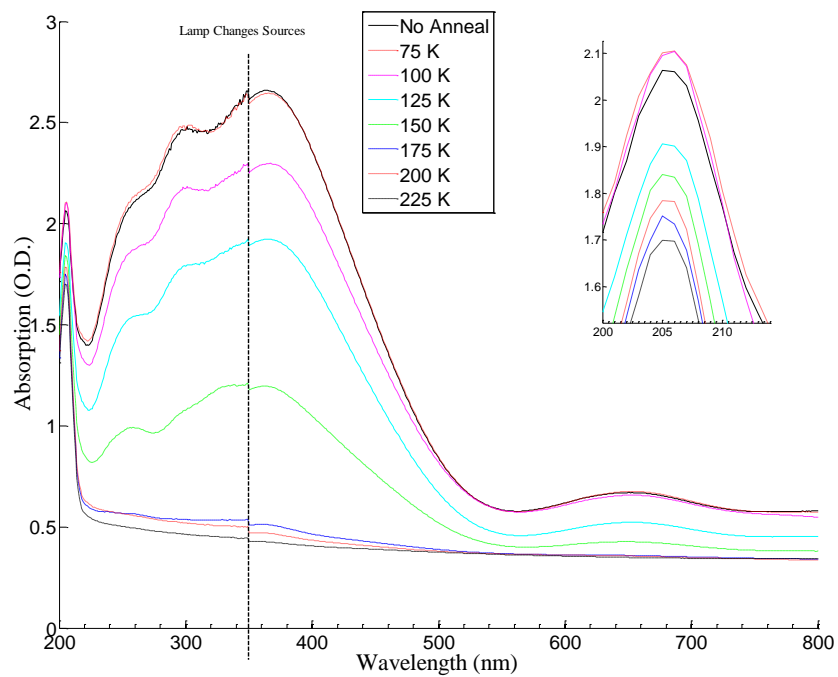


Fig. 6.6. Absorption spectra taken during isochronal annealing experiment. The inset is a magnification of the peaks at 205 nm.

## 6.2. Discussion

The research of this chapter has demonstrated that EPR spectra along with optical absorption and fluorospectroscopy data (i.e., PL and PLE) can be combined to conclusively show that the absorption peak near 298 nm is due to  $\text{Ag}^{2+}$  ions in x-ray irradiated Ag-doped LTB crystals. This study provides insight about the absorption spectrum of Ag-doped LTB as well as further confirmation for the defect models presented in Chapter Four concerning the silver valence states both prior to and after exposure to x-ray radiation. Understanding the photoluminescence and absorption characteristics of LTB are also important in utilizing LTB crystals for dosimetry applications.

Absorption spectra are commonly plotted as energy versus optical density which is a direct conversion using  $E = \frac{hc}{\lambda}$ . A slight correction for wavelength dependence to spectral response is also needed in the emission and excitation data presented. This correction is illustrated in appendix A of Luminescent Materials [84].

## VII. Conclusions

### 7.1. Summary of Findings

Lithium tetraborate ( $\text{Li}_2\text{B}_4\text{O}_7$ ), commonly referred to as LTB, is a versatile insulating crystal with potential use in neutron detection. LTB has been grown using enriched  $^6\text{Li}$  and  $^{10}\text{B}$  to increase its neutron opacity [4]. When doped with an appropriate optically active element, LTB could be used as an effective scintillation material and thus is an important candidate for high-sensitivity thermoluminescence dosimetry applications [52-54]. Radiative processes associated with these dopants are highly efficient in this material, and bright, above-room-temperature thermoluminescence peaks are observed. Lithium tetraborate has been grown pure and doped with many different elements including transition metals, actinides, and rare earth elements. The research in this dissertation addressed undoped lithium tetraborate as well as LTB doped with copper and silver. Specifically, this dissertation has focused on identifying and characterizing point defects in lithium tetraborate crystals as well as explaining their role in electron and hole recombination processes. These electron-hole recombination processes have been shown to explain the thermoluminescent glow curves in both Cu- and Ag-doped LTB crystals.

In Chapter Three, the research has provided insight to the use of lithium tetraborate as a possible neutron detection material. Experiment has shown that there are large numbers of lithium and compensating oxygen vacancies in the as-grown crystals [31]. These vacancies are responsible for trapping electrons and holes. The trapped hole center investigated in this chapter has a very low thermal stability, less than 90 K, and is populated during exposure to ionizing radiation. These trapped holes recombine with trapped electrons and release visible light when the crystal is heated above 90 K. This is

demonstrated with the low temperature thermoluminescent data presented. A full set of spin-Hamiltonian parameters were determined for the low temperature hole center. The hole trapping centers may have different effects on the performance of LTB as a scintillating material. A nuclear event, i.e., neutron capture, in LTB is accompanied by ionizing radiation. This ionizing radiation produces electrons and holes that will then migrate through the crystal lattice. These electrons and holes may recombine at the hole trapping site investigated in Chapter Three and produce visible light that could be collected in a photomultiplier tube. This would be a benefitting defect in neutron detection. However, ionizing radiation unrelated to neutron capture may also produce electron hole pairs that again recombine at the hole trapping site investigated and lead to a “false” count in a neutron detector. This would be a negative effect in determining neutron capture.

Concerning Chapter Four, there are several significant achievements. A full set of spin Hamiltonian parameters were determined for a defect that had been previously reported [31] but not characterized. The method of characterization, i.e., using EPR alone to solve for the  $g$  and hyperfine parameters, was validated by comparing the research of Chapter Four to published results for the unperturbed hole center. This chapter has shown that it is possible to find a good set of  $g$  and hyperfine parameters using EPR alone for a defect that contains two isotopes of similar nuclear magnetic moments that could not otherwise have been characterized. Now, all of the defects have been characterized that participate in electron-hole recombination and contribute to the thermoluminescent glow curve of x-ray exposed Ag-doped LTB. In order for lithium

tetraborate to become a viable candidate for dosimetry and nuclear detection applications [55-56], it is important to characterize all of the defects in the material.

While performing research for Chapter Five, an attempt to increase signal intensity of a previously identified trapped hole center in Cu-doped lithium tetraborate led to the discovery of several new spectra that have not been reported in the literature. Two new similar, yet different, electron centers are identified and characterized. Two new hole centers are also identified. After establishing models for the copper-related EPR spectra, the study continued with an investigation of the thermal stability of the copper defects. It is shown that the x-ray-induced electron and hole centers recombine at temperatures that correspond to thermoluminescence peak temperatures reported in the literature [68, 70, 72]. This research has identified the defects responsible for the TL glow curves and can be beneficial in utilizing copper-doped lithium tetraborate as an x-ray radiation dosimeter.

In Chapter Six, electron paramagnetic resonance (EPR), optical absorption (OA), photoluminescence (PL), and photoluminescence excitation (PLE) data have been collected in an effort to provide a comprehensive description of the optical features observed from silver-doped lithium tetraborate crystals. The results in this chapter show that EPR spectra along with optical absorption and fluorospectroscopy data (i.e., PL and PLE) can be combined to conclusively establish that the absorption peak near 298 nm is due to  $\text{Ag}^{2+}$  ions in x-ray irradiated Ag-doped LTB crystals. This study provides insight about the absorption spectrum of Ag-doped LTB as well as further confirmation for the defect models presented in Chapter Four concerning the silver valence states both prior to and after exposure to x-ray radiation. Understanding the photoluminescence and



absorption characteristics of LTB are also important in utilizing LTB crystals for dosimetry applications.

## **7.2. Future Work**

If LTB is to be incorporated in neutron detectors and sensors, much research remains to be done. This dissertation has characterized the intrinsic hole trap in LTB, but has not addressed the intrinsic electron trap (i.e., the oxygen vacancies). The paramagnetic defects in silver-doped LTB have been investigated at length and the spin-Hamiltonian parameters have been determined for both electron and hole centers. Silver-doped LTB has also been optically characterized. Initial work has been performed to optically characterize copper-doped LTB but work remains and the preliminary results were not included in this dissertation.

Additional investigations should be considered if a wider variety of samples were available that complemented those used in the present work. Due to their light-emitting properties, copper- and silver-doped LTB are strong candidates for scintillation and neutron detection applications. Similar research should be performed on other dopants that are known to be optically active. On the basis of size and charge, aluminum and silicon will substitute for boron in the LTB lattice. Nitrogen may substitute for oxygen. If crystals were grown with these dopants, surprisingly new behaviors may occur and their paramagnetic defect and optical properties should be investigated in a similar manner to those experiments described in this dissertation.

A final interesting potential project relates to the work performed in Chapter Three concerning undoped lithium tetraborate. The work of Chapter Three showed that

the electron and hole traps due to oxygen and lithium vacancies produce luminescence. Vapor phase equilibration is a process that reduces the concentration of defects by heating a crystal in a material that will vaporize and cause ions to enter the crystal where they restore the perfect crystallinity. Undoped LTB crystals could be submerged in a lithium-containing powder in a ceramic boat. The crystal and powder could be heated using a furnace set to a temperature that is below LTB's melting point but high enough that lithium ions from the powder may fill the lithium vacancies in the lattice. If the lithium vacancies are filled, the oxygen vacancies will be eliminated at the same time so as to maintain charge neutrality. This has been demonstrated in both lithium niobate and lithium tantalite crystals. After vapor phase equilibration, LTB could be exposed to x rays at 77 K. The EPR and thermoluminescent experiment outlined in Chapter Three could then be used to determine if any lithium and oxygen vacancies remain. If the vacancies are completely removed and the crystal fails to luminesce, the crystal could then be placed in a thermal neutron environment. If the lithium and boron nuclei in the lattice capture neutrons, defects would be produced in the crystal. Post neutron-irradiation measurements of EPR and thermoluminescence could be performed. Signals produced in these measurements could be assigned to neutron capture thus proving that LTB could be used as a neutron detecting material. These newly detected signals may not match previously identified EPR spectra.

## Appendix A

### Experimental EPR and ENDOR Data

Table A.1 Chapter III: LTB trapped hole center data.

Magnetic Field Direction	EPR Resonance Magnetic Field	ENDOR Transition Frequency (MHz)
[001]	3367.60	12.356
[001]	3367.60	12.460
[001]	3367.60	12.601
[101]	3376.64	9.070
[101]	3376.64	9.516
[101]	3376.64	9.980
[101]	3376.64	13.170
[101]	3376.64	13.460
[101]	3376.64	13.760
[101]	3376.64	11.600
[101]	3376.64	11.650
[101]	3376.64	11.700
[100]	3379.18	11.226
[100]	3379.18	11.351
[100]	3379.18	11.445
[100]	3379.18	12.459
[100]	3379.18	12.662
[100]	3379.18	12.858
[110]	3361.10	10.720
[110]	3361.10	10.920
[110]	3361.10	11.170
[110]	3386.74	12.849
[110]	3386.74	12.973
[110]	3386.74	13.081

Table A.2 Chapter IV: LTB:Ag unperturbed trapped hole center data.

Magnetic Field Direction / Angle (°)	EPR Resonance Magnetic Field
<b>Data for <i>a</i> to <i>a</i> plane</b>	
[001]	3087.55
[001]	3108.098
[001]	3136.258
[001]	3158.562
15	3059.343
15	3079.281
15	3100.412
15	3137.968
15	3162.058
15	3184.938
25	3048.214
25	3099.262
25	3141.506
25	3161.461
25	3175.549
25	3197.849
35	3044.109
35	3061.719
35	3081.046
35	3161.461
35	3180.849
35	3201.985
45	3048.193
45	3068.729
45	3176.141
45	3197.27

Table A.2 (cont'd) Chapter IV:LTB:Ag unperturbed trapped hole center data.

Magnetic Field Direction / Angle (°)	EPR Resonance Magnetic Field	Magnetic Field Direction / Angle (°)	EPR Resonance Magnetic Field
Data for c to a plane		Data for c to a plane (cont'd)	
[001]	2977.315	60	2889.682
[001]	3001.566	60	2912.370
		60	3058.719
10	2919.952	60	3082.192
10	2945.757	60	3137.751
10	2969.622	60	3160.452
10	2995.052	60	3269.977
10	3019.676	60	3285.624
10	3046.700		
10	3070.161	70	2941.180
		70	2963.867
20	2872.812	70	3087.515
20	2897.551	70	3111.756
20	2969.104	70	3149.313
20	2993.309	70	3171.223
20	3021.815	70	3230.675
20	3044.942	70	3247.896
20	3125.644		
20	3148.230	80	3014.719
		80	3035.839
30	2841.827	80	3116.812
30	2867.058	80	3140.197
30	2980.335	80	3147.324
30	3002.628	80	3170.805
30	3053.110	80	3162.000
30	3077.184	80	3179.009
30	3199.845		
30	3219.778	[001]	3087.550
		[001]	3108.098
45	2842.557	[001]	3136.258
45	2866.801	[001]	3158.562
45	3012.331		
45	3035.806		
45	3099.145		
45	3122.617		
45	3267.361		
45	3285.328		

Table A.3 Chapter IV: LTB:Ag perturbed trapped hole center.

Magnetic Field Direction / Angle (°)	EPR Resonance Magnetic Field
<b>Data for <math>a</math> to <math>a</math> plane</b>	
[001]	3042.965
[001]	3058.819
[001]	3294.133
[001]	3304.680
15	3042.308
15	3261.255
15	3272.969
15	3288.831
15	3299.390
25	3110.997
25	3224.281
25	3237.190
25	3266.529
25	3277.682
35	3091.055
35	3105.149
35	3136.245
35	3150.346
35	3193.166
35	3231.323
35	3243.043
45 [110]	3132.114
45 [110]	3146.786
45 [110]	3185.534
45 [110]	3197.270

Table A.3 (cont'd) Chapter IV: LTB:Ag perturbed trapped hole center.

Magnetic Field Direction / Angle (°)	EPR Resonance Magnetic Field	Magnetic Field Direction / Angle (°)	EPR Resonance Magnetic Field
Data for <i>c</i> to <i>a</i> plane		Data for <i>c</i> to <i>a</i> plane	
[001]	2931.543	50	3089.195
[001]	2951.301	50	3105.625
		50	3159.608
10	2889.426	50	3172.122
10	2911.328	50	3186.214
10	2931.281		
10	2981.737	60	3172.171
		60	3231.667
20	2858.818	60	3244.939
20	2945.435		
20	3008.362	70	2932.574
20	3057.329	70	2952.130
		70	3139.145
30	3094.174	70	3215.042
30	3110.016	70	3276.065
		70	3287.795
40	3047.808		
40	3120.576	80	2988.303
40	3134.660	80	3005.893
40	3149.529	80	3093.348
		80	3108.603
[101]	3056.118	80	3267.043
[101]	3073.326	80	3279.369
[101]	3135.903	80	3298.719
[101]	3150.763	80	3309.865
[101]	3163.281		
		[100]	3042.965
		[100]	3058.819
		[100]	3294.133
		[100]	3304.68

## Appendix B

### Sample EPR and ENDOR Computer Routines

```
% EnergyLevels_g_and_A
%
% This subroutine is used in conjunction with Cntr_A_EPR_linepositions to
% calculate the line positions as a function of angle for Center A in LiB3O5.
%
% It calculates the eigenvalues and returns them to the main program.

function EE = EnergyLevels_g_and_A(TG,TH,TQ,HH,P,B,gbn)

W1 = B*HH*(P(1)*TG(1,1)*TG(1,3)+P(2)*TG(2,1)*TG(2,3)+P(3)*TG(3,1)*TG(3,3));
W2 = B*HH*(P(1)*TG(1,2)*TG(1,3)+P(2)*TG(2,2)*TG(2,3)+P(3)*TG(3,2)*TG(3,3));
W3 = B*HH*(P(1)*TG(1,3)*TG(1,3)+P(2)*TG(2,3)*TG(2,3)+P(3)*TG(3,3)*TG(3,3));
W4 = P(7)*TH(1,1)*TH(1,1)+P(8)*TH(2,1)*TH(2,1)+P(9)*TH(3,1)*TH(3,1);
W5 = P(7)*TH(1,2)*TH(1,1)+P(8)*TH(2,2)*TH(2,1)+P(9)*TH(3,2)*TH(3,1);
W6 = P(7)*TH(1,3)*TH(1,1)+P(8)*TH(2,3)*TH(2,1)+P(9)*TH(3,3)*TH(3,1);
W7 = P(7)*TH(1,2)*TH(1,2)+P(8)*TH(2,2)*TH(2,2)+P(9)*TH(3,2)*TH(3,2);
W8 = P(7)*TH(1,3)*TH(1,2)+P(8)*TH(2,3)*TH(2,2)+P(9)*TH(3,3)*TH(3,2);
W9 = P(7)*TH(1,3)*TH(1,3)+P(8)*TH(2,3)*TH(2,3)+P(9)*TH(3,3)*TH(3,3);
QZZ = -(P(13)+P(14));
W10 = P(13)*TQ(1,1)*TQ(1,1)+P(14)*TQ(2,1)*TQ(2,1)+QZZ*TQ(3,1)*TQ(3,1);
W11 = P(13)*TQ(1,2)*TQ(1,1)+P(14)*TQ(2,2)*TQ(2,1)+QZZ*TQ(3,2)*TQ(3,1);
W12 = P(13)*TQ(1,3)*TQ(1,1)+P(14)*TQ(2,3)*TQ(2,1)+QZZ*TQ(3,3)*TQ(3,1);
W13 = P(13)*TQ(1,2)*TQ(1,2)+P(14)*TQ(2,2)*TQ(2,2)+QZZ*TQ(3,2)*TQ(3,2);
W14 = P(13)*TQ(1,3)*TQ(1,2)+P(14)*TQ(2,3)*TQ(2,2)+QZZ*TQ(3,3)*TQ(3,2);
W15 = P(13)*TQ(1,3)*TQ(1,3)+P(14)*TQ(2,3)*TQ(2,3)+QZZ*TQ(3,3)*TQ(3,3);

Q1 = 0.5*(W1+i*W2);
Q2 = 0.25*(W4-W7)+0.5*i*W5;
Q3 = 0.25*(W4+W7);
Q4 = 0.5*(W6+i*W8);
Q5 = 0.25*(W10-W13)+0.5*i*W11;
Q6 = 0.25*(W10+W13);
Q7 = 0.5*(W12+i*W14);

% HAM is the matrix representing the spin-Hamiltonian

Ham = zeros(8);
Ham(1,1) = 0.5*W3 + 0.75*W9 + 2.25*W15 - 1.5*gbn*HH + 3*Q6;
Ham(2,2) = 0.5*W3 + 0.25*W9 + 0.25*W15 - 0.5*gbn*HH + 7*Q6;
Ham(3,3) = 0.5*W3 - 0.25*W9 + 0.25*W15 + 0.5*gbn*HH + 7*Q6;
Ham(4,4) = 0.5*W3 - 0.75*W9 + 2.25*W15 + 1.5*gbn*HH + 3*Q6;
Ham(5,5) = -0.5*W3 - 0.75*W9 + 2.25*W15 - 1.5*gbn*HH + 3*Q6;
Ham(6,6) = -0.5*W3 - 0.25*W9 + 0.25*W15 - 0.5*gbn*HH + 7*Q6;
Ham(7,7) = -0.5*W3 + 0.25*W9 + 0.25*W15 + 0.5*gbn*HH + 7*Q6;
Ham(8,8) = -0.5*W3 + 0.75*W9 + 2.25*W15 + 1.5*gbn*HH + 3*Q6;
Ham(2,1) = 0.5*sqrt(3)*Q4 + 2*sqrt(3)*Q7;
Ham(3,1) = 2*sqrt(3)*Q5;
Ham(3,2) = Q4;
Ham(4,2) = 2*sqrt(3)*Q5;
Ham(4,3) = 0.5*sqrt(3)*Q4 - 2*sqrt(3)*Q7;
Ham(5,1) = Q1 + 1.5*Q4;
Ham(5,2) = sqrt(3)*Q3;
Ham(6,1) = sqrt(3)*Q2;
Ham(6,2) = Q1 + 0.5*Q4;
Ham(6,3) = 2*Q3;
Ham(6,5) = -0.5*sqrt(3)*Q4 + 2*sqrt(3)*Q7;
Ham(7,2) = 2*Q2;
Ham(7,3) = Q1 - 0.5*Q4;
Ham(7,4) = sqrt(3)*Q3;
Ham(7,5) = 2*sqrt(3)*Q5;
Ham(7,6) = -Q4;
Ham(8,3) = sqrt(3)*Q2;
Ham(8,4) = Q1 - 1.5*Q4;
```



```

Ham(8,6) = 2*sqrt(3)*Q5;
Ham(8,7) = -0.5*sqrt(3)*Q4 -2*sqrt(3)*Q7;
Ham(1,2) = conj(Ham(2,1));
Ham(1,3) = conj(Ham(3,1));
Ham(2,3) = conj(Ham(3,2));
Ham(2,4) = conj(Ham(4,2));
Ham(3,4) = conj(Ham(4,3));
Ham(1,5) = conj(Ham(5,1));
Ham(2,5) = conj(Ham(5,2));
Ham(1,6) = conj(Ham(6,1));
Ham(2,6) = conj(Ham(6,2));
Ham(3,6) = conj(Ham(6,3));
Ham(5,6) = conj(Ham(6,5));
Ham(2,7) = conj(Ham(7,2));
Ham(3,7) = conj(Ham(7,3));
Ham(4,7) = conj(Ham(7,4));
Ham(5,7) = conj(Ham(7,5));
Ham(6,7) = conj(Ham(7,6));
Ham(3,8) = conj(Ham(8,3));
Ham(4,8) = conj(Ham(8,4));
Ham(6,8) = conj(Ham(8,6));
Ham(7,8) = conj(Ham(8,7));

EE = sort(real(eig(Ham)));

%           Lithium Tetraborate: Subroutine for hyperfine and
%           quadrupole parameters fitting.
%
% This subroutine is used in conjunction with Li_vacancy_ENDOR_fitting
% to determine the best set of 11B hyperfine parameters for the
% Li+ vacancy hole center in Li2B4O7.

% It calculates a sum of the frequency differences squared and
% returns the value to the main program. The input data are the
% measured magnetic fields and ENDOR frequencies.

function summ = Li_vacancy_ENDOR_fitting_sub(PP,P,B,gbn)

CTR = pi/180;

% G is the 3x3 rotation matrix which takes the principal
% axes of the g matrix into the crystal coordinate system.

% H is the 3x3 rotation matrix which takes the principal
% axes of the A matrix into the crystal coordinate system.

% Q is the 3x3 rotation matrix which takes the principal
% axes of the Q matrix into the crystal coordinate system.

% R is the 3x3 rotation matrix which takes the crystal coordinate
% system into the magnetic field coordinate system.

G(1,1) = cos(PP(6))*cos(PP(5)) - cos(PP(4))*sin(PP(5))*sin(PP(6));
G(1,2) = cos(PP(6))*sin(PP(5)) + cos(PP(4))*cos(PP(5))*sin(PP(6));
G(1,3) = sin(PP(6))*sin(PP(4));
G(2,1) = -sin(PP(6))*cos(PP(5)) - cos(PP(4))*sin(PP(5))*cos(PP(6));
G(2,2) = -sin(PP(6))*sin(PP(5)) + cos(PP(4))*cos(PP(5))*cos(PP(6));
G(2,3) = cos(PP(6))*sin(PP(4));
G(3,1) = sin(PP(4))*sin(PP(5));
G(3,2) = -sin(PP(4))*cos(PP(5));
G(3,3) = cos(PP(4));

H(1,1) = cos(P(6))*cos(P(5)) - cos(P(4))*sin(P(5))*sin(P(6));
H(1,2) = cos(P(6))*sin(P(5)) + cos(P(4))*cos(P(5))*sin(P(6));
H(1,3) = sin(P(6))*sin(P(4));
H(2,1) = -sin(P(6))*cos(P(5)) - cos(P(4))*sin(P(5))*cos(P(6));
H(2,2) = -sin(P(6))*sin(P(5)) + cos(P(4))*cos(P(5))*cos(P(6));
H(2,3) = cos(P(6))*sin(P(4));

```

```
H(3,1) = sin(P(4))*sin(P(5));
H(3,2) = -sin(P(4))*cos(P(5));
H(3,3) = cos(P(4));
```

```
Q(1,1) = cos(P(11))*cos(P(10)) - cos(P(9))*sin(P(10))*sin(P(11));
Q(1,2) = cos(P(11))*sin(P(10)) + cos(P(9))*cos(P(10))*sin(P(11));
Q(1,3) = sin(P(11))*sin(P(9));
Q(2,1) = -sin(P(11))*cos(P(10)) - cos(P(9))*sin(P(10))*cos(P(11));
Q(2,2) = -sin(P(11))*sin(P(10)) + cos(P(9))*cos(P(10))*cos(P(11));
Q(2,3) = cos(P(11))*sin(P(9));
Q(3,1) = sin(P(9))*sin(P(10));
Q(3,2) = -sin(P(9))*cos(P(10));
Q(3,3) = cos(P(9));
```

```
% Data for [001]
```

```
h(1)=3367.6;FRQ(1)=12.356;Line(1)=3;Alpha(1)=0*CTR;Beta(1)=0*CTR;
h(2)=3367.6;FRQ(2)=12.46;Line(2)=2;Alpha(2)=0*CTR;Beta(2)=0*CTR;
h(3)=3367.6;FRQ(3)=12.601;Line(3)=1;Alpha(3)=0*CTR;Beta(3)=0*CTR;
```

```
% Data for [101]
```

```
h(4)=3376.64;FRQ(4)=9.07;Line(4)=1;Alpha(4)=45*CTR;Beta(4)=0*CTR;
h(5)=3376.64;FRQ(5)=9.516;Line(5)=2;Alpha(5)=45*CTR;Beta(5)=0*CTR;
h(6)=3376.64;FRQ(6)=9.98;Line(6)=3;Alpha(6)=45*CTR;Beta(6)=0*CTR;
h(7)=3376.64;FRQ(7)=13.17;Line(7)=3;Alpha(7)=45*CTR;Beta(7)=90*CTR;
h(8)=3376.64;FRQ(8)=13.46;Line(8)=2;Alpha(8)=45*CTR;Beta(8)=90*CTR;
h(9)=3376.64;FRQ(9)=13.76;Line(9)=1;Alpha(9)=45*CTR;Beta(9)=90*CTR;
h(10)=3376.64;FRQ(10)=11.6;Line(10)=3;Alpha(10)=45*CTR;Beta(10)=270*CTR;
h(11)=3376.64;FRQ(11)=11.65;Line(11)=2;Alpha(11)=45*CTR;Beta(11)=270*CTR;
h(12)=3376.64;FRQ(12)=11.7;Line(12)=1;Alpha(12)=45*CTR;Beta(12)=270*CTR;
```

```
% Data for [100]
```

```
h(13)=3379.18;FRQ(13)=11.226;Line(13)=3;Alpha(13)=90*CTR;Beta(13)=0*CTR;
h(14)=3379.18;FRQ(14)=11.351;Line(14)=2;Alpha(14)=90*CTR;Beta(14)=0*CTR;
h(15)=3379.18;FRQ(15)=11.445;Line(15)=1;Alpha(15)=90*CTR;Beta(15)=0*CTR;
h(16)=3379.18;FRQ(16)=12.459;Line(16)=3;Alpha(16)=90*CTR;Beta(16)=90*CTR;
h(17)=3379.18;FRQ(17)=12.662;Line(17)=2;Alpha(17)=90*CTR;Beta(17)=90*CTR;
h(18)=3379.18;FRQ(18)=12.858;Line(18)=1;Alpha(18)=90*CTR;Beta(18)=90*CTR;
```

```
% Data for [110]
```

```
h(19)=3361.10;FRQ(19)=10.72;Line(19)=3;Alpha(19)=90*CTR;Beta(19)=45*CTR;
h(20)=3361.10;FRQ(20)=10.92;Line(20)=2;Alpha(20)=90*CTR;Beta(20)=45*CTR;
h(21)=3361.10;FRQ(21)=11.17;Line(21)=1;Alpha(21)=90*CTR;Beta(21)=45*CTR;
h(22)=3386.74;FRQ(22)=12.849;Line(22)=3;Alpha(22)=90*CTR;Beta(22)=135*CTR;
h(23)=3386.74;FRQ(23)=12.973;Line(23)=2;Alpha(23)=90*CTR;Beta(23)=135*CTR;
h(24)=3386.74;FRQ(24)=13.081;Line(24)=1;Alpha(24)=90*CTR;Beta(24)=135*CTR;
```

```
%Data for [100+10]
```

```
%h(25)=3373.0;FRQ(25)=10.88;Line(25)=3;Alpha(25)=90*CTR;Beta(25)=10*CTR;
%h(26)=3373.0;FRQ(26)=11.02;Line(26)=2;Alpha(26)=90*CTR;Beta(26)=10*CTR;
%h(27)=3373.0;FRQ(27)=11.17;Line(27)=1;Alpha(27)=90*CTR;Beta(27)=10*CTR;
%h(28)=3373.0;FRQ(28)=12.79;Line(28)=3;Alpha(28)=90*CTR;Beta(28)=100*CTR;
%h(29)=3373.0;FRQ(29)=12.99;Line(29)=2;Alpha(29)=90*CTR;Beta(29)=100*CTR;
%h(30)=3373.0;FRQ(30)=13.15;Line(30)=1;Alpha(30)=90*CTR;Beta(30)=100*CTR;
```

```
datapoints = length(h);
```

```
for nn=1:datapoints
```

```
    HH = h(nn);
    line = Line(nn);
    alpha = Alpha(nn);
    beta = Beta(nn);
```

```
    R(1,1) = cos(alpha)*cos(beta);
    R(1,2) = -sin(beta);
    R(1,3) = sin(alpha)*cos(beta);
    R(2,1) = cos(alpha)*sin(beta);
    R(2,2) = cos(beta);
    R(2,3) = sin(alpha)*sin(beta);
    R(3,1) = -sin(alpha);
```

```

R(3,2) = 0;
R(3,3) = cos(alpha);

TG = G * R;
TH = H * R;
TQ = Q * R;

W1 = B*HH*(PP(1)*TG(1,1)*TG(1,3)+PP(2)*TG(2,1)*TG(2,3)+PP(3)*TG(3,1)*TG(3,3));
W2 = B*HH*(PP(1)*TG(1,2)*TG(1,3)+PP(2)*TG(2,2)*TG(2,3)+PP(3)*TG(3,2)*TG(3,3));
W3 = B*HH*(PP(1)*TG(1,3)*TG(1,3)+PP(2)*TG(2,3)*TG(2,3)+PP(3)*TG(3,3)*TG(3,3));
W4 = P(1)*TH(1,1)*TH(1,1)+P(2)*TH(2,1)*TH(2,1)+P(3)*TH(3,1)*TH(3,1);
W5 = P(1)*TH(1,1)*TH(1,2)+P(2)*TH(2,1)*TH(2,2)+P(3)*TH(3,1)*TH(3,2);
W6 = P(1)*TH(1,1)*TH(1,3)+P(2)*TH(2,1)*TH(2,3)+P(3)*TH(3,1)*TH(3,3);
W7 = P(1)*TH(1,2)*TH(1,2)+P(2)*TH(2,2)*TH(2,2)+P(3)*TH(3,2)*TH(3,2);
W8 = P(1)*TH(1,2)*TH(1,3)+P(2)*TH(2,2)*TH(2,3)+P(3)*TH(3,2)*TH(3,3);
W9 = P(1)*TH(1,3)*TH(1,3)+P(2)*TH(2,3)*TH(2,3)+P(3)*TH(3,3)*TH(3,3);
QZZ = -(P(7)+P(8));
W10 = P(7)*TQ(1,1)*TQ(1,1)+P(8)*TQ(2,1)*TQ(2,1)+QZZ*TQ(3,1)*TQ(3,1);
W11 = P(7)*TQ(1,2)*TQ(1,1)+P(8)*TQ(2,2)*TQ(2,1)+QZZ*TQ(3,2)*TQ(3,1);
W12 = P(7)*TQ(1,3)*TQ(1,1)+P(8)*TQ(2,3)*TQ(2,1)+QZZ*TQ(3,3)*TQ(3,1);
W13 = P(7)*TQ(1,2)*TQ(1,2)+P(8)*TQ(2,2)*TQ(2,2)+QZZ*TQ(3,2)*TQ(3,2);
W14 = P(7)*TQ(1,3)*TQ(1,2)+P(8)*TQ(2,3)*TQ(2,2)+QZZ*TQ(3,3)*TQ(3,2);
W15 = P(7)*TQ(1,3)*TQ(1,3)+P(8)*TQ(2,3)*TQ(2,3)+QZZ*TQ(3,3)*TQ(3,3);

Q1 = 0.5*(W1+i*W2);
Q2 = 0.25*(W4-W7)+0.5*i*W5;
Q3 = 0.25*(W4+W7);
Q4 = 0.5*(W6+i*W8);
Q5 = 0.25*(W10-W13)+0.5*i*W11;
Q6 = 0.25*(W10+W13);
Q7 = 0.5*(W12+i*W14);

% Ham is the matrix representing the spin-Hamiltonian:

Ham = zeros(8);
Ham(1,1) = 0.5*W3 + 0.75*W9 + 2.25*W15 - 1.5*gbn*HH + 3*Q6;
Ham(2,2) = 0.5*W3 + 0.25*W9 + 0.25*W15 - 0.5*gbn*HH + 7*Q6;
Ham(3,3) = 0.5*W3 - 0.25*W9 + 0.25*W15 + 0.5*gbn*HH + 7*Q6;
Ham(4,4) = 0.5*W3 - 0.75*W9 + 2.25*W15 + 1.5*gbn*HH + 3*Q6;
Ham(5,5) = -0.5*W3 - 0.75*W9 + 2.25*W15 - 1.5*gbn*HH + 3*Q6;
Ham(6,6) = -0.5*W3 - 0.25*W9 + 0.25*W15 - 0.5*gbn*HH + 7*Q6;
Ham(7,7) = -0.5*W3 + 0.25*W9 + 0.25*W15 + 0.5*gbn*HH + 7*Q6;
Ham(8,8) = -0.5*W3 + 0.75*W9 + 2.25*W15 + 1.5*gbn*HH + 3*Q6;
Ham(2,1) = 0.5*sqrt(3)*Q4 + 2*sqrt(3)*Q7;
Ham(3,1) = 2*sqrt(3)*Q5;
Ham(3,2) = Q4;
Ham(4,2) = 2*sqrt(3)*Q5;
Ham(4,3) = 0.5*sqrt(3)*Q4 - 2*sqrt(3)*Q7;
Ham(5,1) = Q1 + 1.5*Q4;
Ham(5,2) = sqrt(3)*Q3;
Ham(6,1) = sqrt(3)*Q2;
Ham(6,2) = Q1 + 0.5*Q4;
Ham(6,3) = 2*Q3;
Ham(6,5) = -0.5*sqrt(3)*Q4 + 2*sqrt(3)*Q7;
Ham(7,2) = 2*Q2;
Ham(7,3) = Q1 - 0.5*Q4;
Ham(7,4) = sqrt(3)*Q3;
Ham(7,5) = 2*sqrt(3)*Q5;
Ham(7,6) = -Q4;
Ham(8,3) = sqrt(3)*Q2;
Ham(8,4) = Q1 - 1.5*Q4;
Ham(8,6) = 2*sqrt(3)*Q5;
Ham(8,7) = -0.5*sqrt(3)*Q4 - 2*sqrt(3)*Q7;
Ham(1,2) = conj(Ham(2,1));
Ham(1,3) = conj(Ham(3,1));
Ham(2,3) = conj(Ham(3,2));
Ham(2,4) = conj(Ham(4,2));
Ham(3,4) = conj(Ham(4,3));
Ham(1,5) = conj(Ham(5,1));
Ham(2,5) = conj(Ham(5,2));

```

```

Ham(1,6) = conj(Ham(6,1));
Ham(2,6) = conj(Ham(6,2));
Ham(3,6) = conj(Ham(6,3));
Ham(5,6) = conj(Ham(6,5));
Ham(2,7) = conj(Ham(7,2));
Ham(3,7) = conj(Ham(7,3));
Ham(4,7) = conj(Ham(7,4));
Ham(5,7) = conj(Ham(7,5));
Ham(6,7) = conj(Ham(7,6));
Ham(3,8) = conj(Ham(8,3));
Ham(4,8) = conj(Ham(8,4));
Ham(6,8) = conj(Ham(8,6));
Ham(7,8) = conj(Ham(8,7));

EE = sort(real(eig(Ham)));
if line == 1
    Freq(nn) = abs(EE(2) - EE(1));
elseif line == 2
    Freq(nn) = abs(EE(3) - EE(2));
elseif line == 3
    Freq(nn) = abs(EE(4) - EE(3));
elseif line == 4
    Freq(nn) = abs(EE(6) - EE(5));
elseif line == 5
    Freq(nn) = abs(EE(7) - EE(6));
elseif line == 6
    Freq(nn) = abs(EE(8) - EE(7));
end
end
summ=0;

for ii=1:datapoints
    summ = summ + (FRQ(ii)-Freq(ii))^2;
end
end

%           EPR_fitting_gandA_P

% This program determines the "best" set of g and A parameters for the
% perturbed Ag2+ hole center in Li2B4O7. Because lines from the two
% isotopes of Ag (107 and 109) are not resolved in the EPR spectra, an
% "averaged" A matrix representing the two isotopes together is used in
% this fitting program.

% Input data consists of 74 EPR magnetic field values and their corresponding
% microwave frequencies. The output is 12 parameters (three principal values
% and three Euler angles for both g and A).

% This program uses a subroutine named SUMM_EPR_fitting_gandA_P.

clear all

% Constants:

h = 6.626069;      % Planck's constant
B = 9.274009/h;    % Bohr magneton divided by Planck's constant
gbn = -0.00018637; % averaged value of gn*bn for 107Ag and 109Ag
CTR = pi/180;      % Conversion constant, degrees to radians

% Initial values of the spin-Hamiltonian parameters:
% Six for the g matrix (three principal values and three angles).
% Six for the A matrix (three principal values and three angles).

P(1) = 2.0329;
P(2) = 2.1215;
P(3) = 2.3607;
P(4) = 35.7*CTR;
P(5) = 9.7*CTR;
P(6) = -9.9*CTR;

```

```

P(7) = 27.31;
P(8) = 34.13;
P(9) = 66.04;
P(10) = 33.4*CTR;
P(11) = 26.0*CTR;
P(12) = -40.6*CTR;

% Step sizes for the parameters:

gg = 0.0001;      % step size for the g principal values
aa = 0.01;        % step size for the A principal values
delta = 0.1*CTR;  % step size for the angles

step(1) = gg;
step(2) = gg;
step(3) = gg;
step(4) = delta;
step(5) = delta;
step(6) = delta;
step(7) = aa;
step(8) = aa;
step(9) = aa;
step(10) = delta;
step(11) = delta;
step(12) = delta;

sum2 = 0;
sum1 = SUMM_EPR_fitting_gandA_P(P,B,gbn);

while sum2<sum1
    for n = 1:12
        summ = SUMM_EPR_fitting_gandA_P(P,B,gbn);
        sum2 = summ;
        if n==1;
            sum1 = summ;
        end
        P(n) = P(n) + step(n);
        summ = SUMM_EPR_fitting_gandA_P(P,B,gbn);
        if summ >= sum2;
            P(n) = P(n) - 2*step(n);
            summ = SUMM_EPR_fitting_gandA_P(P,B,gbn);
            if summ >= sum2;
                P(n) = P(n) + step(n);
            end
        end
    end
    if summ<sum2;
        sum2 = summ;
    end
end
sum2

P(4) = P(4)/CTR;
P(5) = P(5)/CTR;
P(6) = P(6)/CTR;
P(10) = P(10)/CTR;
P(11) = P(11)/CTR;
P(12) = P(12)/CTR;

P          % Display final set of parameters.
sum2       % Display final value of sum2.

% End of program.

```

```

%          SUMM_EPR_fitting_gandA_P

% This subroutine is used in conjunction with EPR_fitting_gandA to
% determine the best set of g and "averaged" A hyperfine parameters
% for the perturbed Ag2+ trapped hole center in Li2B4O7.

% It calculates a sum of the frequency differences squared and
% returns the value to the main program. The input data are the
% measured magnetic fields and microwave frequencies.

function summ = SUMM_EPR_fitting_gandA_P(P,B,gbn)

CTR = pi/180;

% G is the 3x3 rotation matrix which takes the principal
% axes of the g matrix into the crystal coordinate system.
% Taken from "Classical Mechanics, 2nd ed." by Goldstein, pp. 146-147.

% H is the 3x3 rotation matrix which takes the principal
% axes of the A matrix into the crystal coordinate system.

% R1 is the 3x3 rotation matrix which takes sites 1 through 8
% into the crystal coordinate system.

% R is the 3x3 rotation matrix which takes the crystal coordinate
% system into the magnetic field coordinate system.

G(1,1) = cos(P(6))*cos(P(5)) - cos(P(4))*sin(P(5))*sin(P(6));
G(1,2) = cos(P(6))*sin(P(5)) + cos(P(4))*cos(P(5))*sin(P(6));
G(1,3) = sin(P(6))*sin(P(4));
G(2,1) = -sin(P(6))*cos(P(5)) - cos(P(4))*sin(P(5))*cos(P(6));
G(2,2) = -sin(P(6))*sin(P(5)) + cos(P(4))*cos(P(5))*cos(P(6));
G(2,3) = cos(P(6))*sin(P(4));
G(3,1) = sin(P(4))*sin(P(5));
G(3,2) = -sin(P(4))*cos(P(5));
G(3,3) = cos(P(4));

H(1,1) = cos(P(12))*cos(P(11)) - cos(P(10))*sin(P(11))*sin(P(12));
H(1,2) = cos(P(12))*sin(P(11)) + cos(P(10))*cos(P(11))*sin(P(12));
H(1,3) = sin(P(12))*sin(P(10));
H(2,1) = -sin(P(12))*cos(P(11)) - cos(P(10))*sin(P(11))*cos(P(12));
H(2,2) = -sin(P(12))*sin(P(11)) + cos(P(10))*cos(P(11))*cos(P(12));
H(2,3) = cos(P(12))*sin(P(10));
H(3,1) = sin(P(10))*sin(P(11));
H(3,2) = -sin(P(10))*cos(P(11));
H(3,3) = cos(P(10));

% Rotation from [001] to [100]. These data were taken on July 24 and 25, 2012.

h(1)=2931.543;FRQ(1)=9399.820;Alpha(1)=0*CTR;Beta(1)=0*CTR;K(1)=1;IC(1)=1;
h(2)=2951.301;FRQ(2)=9399.820;Alpha(2)=0*CTR;Beta(2)=0*CTR;K(2)=1;IC(2)=2;

h(3)=2889.426;FRQ(3)=9399.298;Alpha(3)=10*CTR;Beta(3)=0*CTR;K(3)=2;IC(3)=1;
h(4)=2911.328;FRQ(4)=9399.298;Alpha(4)=10*CTR;Beta(4)=0*CTR;K(4)=2;IC(4)=2;
h(5)=2931.281;FRQ(5)=9399.298;Alpha(5)=10*CTR;Beta(5)=0*CTR;K(5)=1;IC(5)=1;
h(6)=2981.737;FRQ(6)=9399.298;Alpha(6)=10*CTR;Beta(6)=0*CTR;K(6)=4;IC(6)=1;

h(7)=2858.818;FRQ(7)=9399.706;Alpha(7)=20*CTR;Beta(7)=0*CTR;K(7)=2;IC(7)=1;
h(8)=2945.435;FRQ(8)=9399.706;Alpha(8)=20*CTR;Beta(8)=0*CTR;K(8)=1;IC(8)=1;
h(9)=3008.362;FRQ(9)=9399.706;Alpha(9)=20*CTR;Beta(9)=0*CTR;K(9)=3;IC(9)=1;
h(10)=3057.329;FRQ(10)=9399.706;Alpha(10)=20*CTR;Beta(10)=0*CTR;K(10)=4;IC(10)=2;

h(11)=3094.174;FRQ(11)=9400.099;Alpha(11)=30*CTR;Beta(11)=0*CTR;K(11)=4;IC(11)=1;
h(12)=3110.016;FRQ(12)=9400.099;Alpha(12)=30*CTR;Beta(12)=0*CTR;K(12)=4;IC(12)=2;

h(13)=3047.808;FRQ(13)=9400.255;Alpha(13)=40*CTR;Beta(13)=0*CTR;K(13)=1;IC(13)=2;
h(14)=3120.576;FRQ(14)=9400.255;Alpha(14)=40*CTR;Beta(14)=0*CTR;K(14)=3;IC(14)=2;
h(15)=3134.660;FRQ(15)=9400.255;Alpha(15)=40*CTR;Beta(15)=0*CTR;K(15)=4;IC(15)=1;
h(16)=3149.529;FRQ(16)=9400.255;Alpha(16)=40*CTR;Beta(16)=0*CTR;K(16)=4;IC(16)=2;

```

h(17)=3056.118;FRQ(17)=9400.192;Alpha(17)=45\*CTR;Beta(17)=0\*CTR;K(17)=1;IC(17)=1;  
h(18)=3073.326;FRQ(18)=9400.192;Alpha(18)=45\*CTR;Beta(18)=0\*CTR;K(18)=1;IC(18)=2;  
h(19)=3135.903;FRQ(19)=9400.192;Alpha(19)=45\*CTR;Beta(19)=0\*CTR;K(19)=3;IC(19)=1;  
h(20)=3150.763;FRQ(20)=9400.192;Alpha(20)=45\*CTR;Beta(20)=0\*CTR;K(20)=3;IC(20)=2;  
h(21)=3150.763;FRQ(21)=9400.192;Alpha(21)=45\*CTR;Beta(21)=0\*CTR;K(21)=4;IC(21)=1;  
h(22)=3163.281;FRQ(22)=9400.192;Alpha(22)=45\*CTR;Beta(22)=0\*CTR;K(22)=4;IC(22)=2;

h(23)=3089.195;FRQ(23)=9400.445;Alpha(23)=50\*CTR;Beta(23)=0\*CTR;K(23)=1;IC(23)=1;  
h(24)=3105.625;FRQ(24)=9400.445;Alpha(24)=50\*CTR;Beta(24)=0\*CTR;K(24)=1;IC(24)=2;  
h(25)=3159.608;FRQ(25)=9400.445;Alpha(25)=50\*CTR;Beta(25)=0\*CTR;K(25)=4;IC(25)=1;  
h(26)=3172.122;FRQ(26)=9400.445;Alpha(26)=50\*CTR;Beta(26)=0\*CTR;K(26)=4;IC(26)=2;  
h(27)=3172.122;FRQ(27)=9400.445;Alpha(27)=50\*CTR;Beta(27)=0\*CTR;K(27)=3;IC(27)=1;  
h(28)=3186.214;FRQ(28)=9400.445;Alpha(28)=50\*CTR;Beta(28)=0\*CTR;K(28)=3;IC(28)=2;

h(29)=3172.171;FRQ(29)=9400.521;Alpha(29)=60\*CTR;Beta(29)=0\*CTR;K(29)=1;IC(29)=2;  
h(30)=3231.667;FRQ(30)=9400.521;Alpha(30)=60\*CTR;Beta(30)=0\*CTR;K(30)=3;IC(30)=1;  
h(31)=3244.939;FRQ(31)=9400.521;Alpha(31)=60\*CTR;Beta(31)=0\*CTR;K(31)=3;IC(31)=2;

h(32)=2932.574;FRQ(32)=9400.614;Alpha(32)=70\*CTR;Beta(32)=0\*CTR;K(32)=2;IC(32)=1;  
h(33)=2952.130;FRQ(33)=9400.614;Alpha(33)=70\*CTR;Beta(33)=0\*CTR;K(33)=2;IC(33)=2;  
h(34)=3139.145;FRQ(34)=9400.614;Alpha(34)=70\*CTR;Beta(34)=0\*CTR;K(34)=4;IC(34)=1;  
h(35)=3215.042;FRQ(35)=9400.614;Alpha(35)=70\*CTR;Beta(35)=0\*CTR;K(35)=1;IC(35)=1;  
h(36)=3276.065;FRQ(36)=9400.614;Alpha(36)=70\*CTR;Beta(36)=0\*CTR;K(36)=3;IC(36)=1;  
h(37)=3287.795;FRQ(37)=9400.614;Alpha(37)=70\*CTR;Beta(37)=0\*CTR;K(37)=3;IC(37)=2;

h(38)=2988.303;FRQ(38)=9400.569;Alpha(38)=80\*CTR;Beta(38)=0\*CTR;K(38)=2;IC(38)=1;  
h(39)=3005.893;FRQ(39)=9400.569;Alpha(39)=80\*CTR;Beta(39)=0\*CTR;K(39)=2;IC(39)=2;  
h(40)=3093.348;FRQ(40)=9400.569;Alpha(40)=80\*CTR;Beta(40)=0\*CTR;K(40)=4;IC(40)=1;  
h(41)=3108.603;FRQ(41)=9400.569;Alpha(41)=80\*CTR;Beta(41)=0\*CTR;K(41)=4;IC(41)=2;  
h(42)=3267.043;FRQ(42)=9400.569;Alpha(42)=80\*CTR;Beta(42)=0\*CTR;K(42)=1;IC(42)=1;  
h(43)=3279.369;FRQ(43)=9400.569;Alpha(43)=80\*CTR;Beta(43)=0\*CTR;K(43)=1;IC(43)=2;  
h(44)=3298.719;FRQ(44)=9400.569;Alpha(44)=80\*CTR;Beta(44)=0\*CTR;K(44)=3;IC(44)=1;  
h(45)=3309.865;FRQ(45)=9400.569;Alpha(45)=80\*CTR;Beta(45)=0\*CTR;K(45)=3;IC(45)=2;

h(46)=3042.965;FRQ(46)=9400.045;Alpha(46)=90\*CTR;Beta(46)=0\*CTR;K(46)=2;IC(46)=1;  
h(47)=3058.819;FRQ(47)=9400.045;Alpha(47)=90\*CTR;Beta(47)=0\*CTR;K(47)=2;IC(47)=2;  
h(48)=3294.133;FRQ(48)=9400.045;Alpha(48)=90\*CTR;Beta(48)=0\*CTR;K(48)=1;IC(48)=1;  
h(49)=3304.680;FRQ(49)=9400.045;Alpha(49)=90\*CTR;Beta(49)=0\*CTR;K(49)=1;IC(49)=2;

% Rotation from [100] to [110]. These data were taken on July 24 and 25, 2012.

h(50)=3042.965;FRQ(50)=9400.045;Alpha(50)=90\*CTR;Beta(50)=0\*CTR;K(50)=2;IC(50)=1;  
h(51)=3058.819;FRQ(51)=9400.045;Alpha(51)=90\*CTR;Beta(51)=0\*CTR;K(51)=2;IC(51)=2;  
h(52)=3294.133;FRQ(52)=9400.045;Alpha(52)=90\*CTR;Beta(52)=0\*CTR;K(52)=1;IC(52)=1;  
h(53)=3304.680;FRQ(53)=9400.045;Alpha(53)=90\*CTR;Beta(53)=0\*CTR;K(53)=1;IC(53)=2;

h(54)=3042.308;FRQ(54)=9398.754;Alpha(54)=90\*CTR;Beta(54)=15\*CTR;K(54)=2;IC(54)=1;  
h(55)=3261.255;FRQ(55)=9398.754;Alpha(55)=90\*CTR;Beta(55)=15\*CTR;K(55)=5;IC(55)=1;  
h(56)=3272.969;FRQ(56)=9398.754;Alpha(56)=90\*CTR;Beta(56)=15\*CTR;K(56)=5;IC(56)=2;  
h(57)=3288.831;FRQ(57)=9398.754;Alpha(57)=90\*CTR;Beta(57)=15\*CTR;K(57)=1;IC(57)=1;  
h(58)=3299.390;FRQ(58)=9398.754;Alpha(58)=90\*CTR;Beta(58)=15\*CTR;K(58)=1;IC(58)=2;

h(59)=3110.997;FRQ(59)=9398.742;Alpha(59)=90\*CTR;Beta(59)=25\*CTR;K(59)=6;IC(59)=2;  
h(60)=3224.281;FRQ(60)=9398.742;Alpha(60)=90\*CTR;Beta(60)=25\*CTR;K(60)=5;IC(60)=1;  
h(61)=3237.190;FRQ(61)=9398.742;Alpha(61)=90\*CTR;Beta(61)=25\*CTR;K(61)=5;IC(61)=2;  
h(62)=3266.529;FRQ(62)=9398.742;Alpha(62)=90\*CTR;Beta(62)=25\*CTR;K(62)=1;IC(62)=1;  
h(63)=3277.682;FRQ(63)=9398.742;Alpha(63)=90\*CTR;Beta(63)=25\*CTR;K(63)=1;IC(63)=2;

h(64)=3091.055;FRQ(64)=9398.832;Alpha(64)=90\*CTR;Beta(64)=35\*CTR;K(64)=2;IC(64)=1;  
h(65)=3105.149;FRQ(65)=9398.832;Alpha(65)=90\*CTR;Beta(65)=35\*CTR;K(65)=2;IC(65)=2;  
h(66)=3136.245;FRQ(66)=9398.832;Alpha(66)=90\*CTR;Beta(66)=35\*CTR;K(66)=6;IC(66)=1;  
h(67)=3150.346;FRQ(67)=9398.832;Alpha(67)=90\*CTR;Beta(67)=35\*CTR;K(67)=6;IC(67)=2;  
h(68)=3193.166;FRQ(68)=9398.832;Alpha(68)=90\*CTR;Beta(68)=35\*CTR;K(68)=5;IC(68)=2;  
h(69)=3231.323;FRQ(69)=9398.832;Alpha(69)=90\*CTR;Beta(69)=35\*CTR;K(69)=1;IC(69)=1;  
h(70)=3243.043;FRQ(70)=9398.832;Alpha(70)=90\*CTR;Beta(70)=35\*CTR;K(70)=1;IC(70)=2;

h(71)=3132.114;FRQ(71)=9399.142;Alpha(71)=90\*CTR;Beta(71)=45\*CTR;K(71)=2;IC(71)=1;  
h(72)=3146.786;FRQ(72)=9399.142;Alpha(72)=90\*CTR;Beta(72)=45\*CTR;K(72)=2;IC(72)=2;  
h(73)=3185.534;FRQ(73)=9399.142;Alpha(73)=90\*CTR;Beta(73)=45\*CTR;K(73)=1;IC(73)=1;

```
h(74)=3197.270;FRQ(74)=9399.142;Alpha(74)=90*CTR;Beta(74)=45*CTR;K(74)=1;IC(74)=2;
```

```
datapoints = length(h);
```

```
for nn=1:datapoints
```

```
    HH = h(nn);
```

```
    alpha = Alpha(nn);
```

```
    beta = Beta(nn);
```

```
    k = K(nn);
```

```
    ic = IC(nn);
```

```
    R(1,1) = cos(alpha)*cos(beta);
```

```
    R(1,2) = -sin(beta);
```

```
    R(1,3) = sin(alpha)*cos(beta);
```

```
    R(2,1) = cos(alpha)*sin(beta);
```

```
    R(2,2) = cos(beta);
```

```
    R(2,3) = sin(alpha)*sin(beta);
```

```
    R(3,1) = -sin(alpha);
```

```
    R(3,2) = 0;
```

```
    R(3,3) = cos(alpha);
```

```
    if k==1
```

```
        R1(1,1) = 1;R1(1,2) = 0;R1(1,3) = 0;
```

```
        R1(2,1) = 0;R1(2,2) = 1;R1(2,3) = 0;
```

```
        R1(3,1) = 0;R1(3,2) = 0;R1(3,3) = 1;
```

```
    elseif k==2
```

```
        R1(1,1) = 0;R1(1,2) = 1;R1(1,3) = 0;
```

```
        R1(2,1) = -1;R1(2,2) = 0;R1(2,3) = 0;
```

```
        R1(3,1) = 0;R1(3,2) = 0;R1(3,3) = 1;
```

```
    elseif k==3
```

```
        R1(1,1) = -1;R1(1,2) = 0;R1(1,3) = 0;
```

```
        R1(2,1) = 0;R1(2,2) = -1;R1(2,3) = 0;
```

```
        R1(3,1) = 0;R1(3,2) = 0;R1(3,3) = 1;
```

```
    elseif k==4
```

```
        R1(1,1) = 0;R1(1,2) = -1;R1(1,3) = 0;
```

```
        R1(2,1) = 1;R1(2,2) = 0;R1(2,3) = 0;
```

```
        R1(3,1) = 0;R1(3,2) = 0;R1(3,3) = 1;
```

```
    elseif k==5
```

```
        R1(1,1) = 1;R1(1,2) = 0;R1(1,3) = 0;
```

```
        R1(2,1) = 0;R1(2,2) = -1;R1(2,3) = 0;
```

```
        R1(3,1) = 0;R1(3,2) = 0;R1(3,3) = -1;
```

```
    elseif k==6
```

```
        R1(1,1) = 0;R1(1,2) = 1;R1(1,3) = 0;
```

```
        R1(2,1) = 1;R1(2,2) = 0;R1(2,3) = 0;
```

```
        R1(3,1) = 0;R1(3,2) = 0;R1(3,3) = -1;
```

```
    elseif k==7
```

```
        R1(1,1) = -1;R1(1,2) = 0;R1(1,3) = 0;
```

```
        R1(2,1) = 0;R1(2,2) = 1;R1(2,3) = 0;
```

```
        R1(3,1) = 0;R1(3,2) = 0;R1(3,3) = -1;
```

```
    elseif k==8
```

```
        R1(1,1) = 0;R1(1,2) = -1;R1(1,3) = 0;
```

```
        R1(2,1) = -1;R1(2,2) = 0;R1(2,3) = 0;
```

```
        R1(3,1) = 0;R1(3,2) = 0;R1(3,3) = -1;
```

```
end
```



```

RT = R1 * R;
TG = G * RT;
TH = H * RT;

W1=B*HH*(P(1)*TG(1,1)*TG(1,3)+P(2)*TG(2,1)*TG(2,3)+P(3)*TG(3,1)*TG(3,3));
W2=B*HH*(P(1)*TG(1,2)*TG(1,3)+P(2)*TG(2,2)*TG(2,3)+P(3)*TG(3,2)*TG(3,3));
W3=B*HH*(P(1)*TG(1,3)*TG(1,3)+P(2)*TG(2,3)*TG(2,3)+P(3)*TG(3,3)*TG(3,3));
W4=P(7)*TH(1,1)*TH(1,1)+P(8)*TH(2,1)*TH(2,1)+P(9)*TH(3,1)*TH(3,1);
W5=P(7)*TH(1,1)*TH(1,2)+P(8)*TH(2,1)*TH(2,2)+P(9)*TH(3,1)*TH(3,2);
W6=P(7)*TH(1,1)*TH(1,3)+P(8)*TH(2,1)*TH(2,3)+P(9)*TH(3,1)*TH(3,3);
W7=P(7)*TH(1,2)*TH(1,2)+P(8)*TH(2,2)*TH(2,2)+P(9)*TH(3,2)*TH(3,2);
W8=P(7)*TH(1,2)*TH(1,3)+P(8)*TH(2,2)*TH(2,3)+P(9)*TH(3,2)*TH(3,3);
W9=P(7)*TH(1,3)*TH(1,3)+P(8)*TH(2,3)*TH(2,3)+P(9)*TH(3,3)*TH(3,3);

Q1 = 0.5*(W1+i*W2);
Q2 = 0.25*(W4-W7)+0.5*i*W5;
Q3 = 0.25*(W4+W7);
Q4 = 0.5*(W6+i*W8);

% Ham is the matrix representing the spin-Hamiltonian:

Ham = zeros(4);
Ham(1,1) = 0.5*W3 + 0.25*W9 - 0.5*gbn*HH;
Ham(2,2) = 0.5*W3 - 0.25*W9 + 0.5*gbn*HH;
Ham(3,3) = -0.5*W3 - 0.25*W9 - 0.5*gbn*HH;
Ham(4,4) = -0.5*W3 + 0.25*W9 + 0.5*gbn*HH;
Ham(2,1) = 0.5*Q4;
Ham(3,1) = Q1 + 0.5*Q4;
Ham(3,2) = Q3;
Ham(4,1) = Q2;
Ham(4,2) = Q1 - 0.5*Q4;
Ham(4,3) = -0.5*Q4;

Ham(1,2) = conj(Ham(2,1));
Ham(1,3) = conj(Ham(3,1));
Ham(1,4) = conj(Ham(4,1));
Ham(2,3) = conj(Ham(3,2));
Ham(2,4) = conj(Ham(4,2));
Ham(3,4) = conj(Ham(4,3));

EE = sort(real(eig(Ham)));

if ic==1
    freq(nn) = abs(EE(4)-EE(1));

elseif ic==2
    freq(nn) = abs(EE(3)-EE(2));
end
end
summ=0;
for ii=1:datapoints
    summ = summ + (FRQ(ii)-freq(ii))^2;
end

% EPR_linepositions_gandA_P
%
% Calculation of EPR linepositions for perturbed Ag2+ hole center in Li2B4O7
% (This program is titled EPR_linepositions_gandA_P.m)

% This program calculates the EPR line positions as a function of angle
% for the x-ray-induced perturbed Ag2+ hole center in LTB. It uses
% a subroutine entitled AgEnergyLevels_P. Both the g matrix and A matrix
% are included (i.e., a 4x4 spin-Hamiltonian matrix is diagonalized).

clear all

% Constants:

```

```

h = 6.626069;      % Planck's constant
B = 9.274009/h;    % Bohr magneton divided by Planck's constant
CTR = pi/180;      % Conversion constant, degrees to radians
FREQQ = 9400;      % Measured microwave frequency (in MHz)
InitialHH = 3300;  % Initial guess for line positions (in gauss)

gbn = -0.00018637; % averaged value of gn*bn for 107Ag and 109Ag

% Spin-Hamiltonian parameters
% Six for the g matrix (three principal values and three angles).
% Six for the A matrix (three principal values and three angles).

P(1) = 2.0319;
P(2) = 2.1212;
P(3) = 2.3604;
P(4) = 35.5*CTR;
P(5) = 9.7*CTR;
P(6) = -9.6*CTR;
P(7) = 28.18;
P(8) = 35.81;
P(9) = 65.12;
P(10) = 35.2*CTR;
P(11) = 25.9*CTR;
P(12) = -38.7*CTR;

% G is the 3x3 rotation matrix which takes the principal
% axes of the g matrix into the crystal coordinate system.
% Taken from "Classical Mechanics, 2nd ed." by Goldstein, pp. 146-147.

% H is the 3x3 rotation matrix which takes the principal
% axes of the A matrix into the crystal coordinate system.

% R1 is the 3x3 rotation matrix which takes sites 1 through 8
% into the crystal coordinate system.

% R is the 3x3 rotation matrix which takes the crystal coordinate
% system into the magnetic field coordinate system.

G(1,1) = cos(P(6))*cos(P(5)) - cos(P(4))*sin(P(5))*sin(P(6));
G(1,2) = cos(P(6))*sin(P(5)) + cos(P(4))*cos(P(5))*sin(P(6));
G(1,3) = sin(P(6))*sin(P(4));
G(2,1) = -sin(P(6))*cos(P(5)) - cos(P(4))*sin(P(5))*cos(P(6));
G(2,2) = -sin(P(6))*sin(P(5)) + cos(P(4))*cos(P(5))*cos(P(6));
G(2,3) = cos(P(6))*sin(P(4));
G(3,1) = sin(P(4))*sin(P(5));
G(3,2) = -sin(P(4))*cos(P(5));
G(3,3) = cos(P(4));

H(1,1) = cos(P(12))*cos(P(11)) - cos(P(10))*sin(P(11))*sin(P(12));
H(1,2) = cos(P(12))*sin(P(11)) + cos(P(10))*cos(P(11))*sin(P(12));
H(1,3) = sin(P(12))*sin(P(10));
H(2,1) = -sin(P(12))*cos(P(11)) - cos(P(10))*sin(P(11))*cos(P(12));
H(2,2) = -sin(P(12))*sin(P(11)) + cos(P(10))*cos(P(11))*cos(P(12));
H(2,3) = cos(P(12))*sin(P(10));
H(3,1) = sin(P(10))*sin(P(11));
H(3,2) = -sin(P(10))*cos(P(11));
H(3,3) = cos(P(10));

% Select a plane of rotation before running the program.

% Plane = 1 corresponds to rotation from a to a.
% Plane = 2 corresponds to rotation from c to a.
% Plane = 3 corresponds to rotation from c to [110].

% Enter the number below for the plane to be used.

for Plane=1      % Rotation from a to a.

for n=1:91      % Rotation increment is one degree.
    Alpha = 90*CTR;

```

```

Beta = (n-1)*CTR;
N(n) = n-1;

R(1,1) = cos(Alpha)*cos(Beta);
R(1,2) = -sin(Beta);
R(1,3) = sin(Alpha)*cos(Beta);
R(2,1) = cos(Alpha)*sin(Beta);
R(2,2) = cos(Beta);
R(2,3) = sin(Alpha)*sin(Beta);
R(3,1) = -sin(Alpha);
R(3,2) = 0;
R(3,3) = cos(Alpha);

for k=1:8

if k==1

    R1(1,1) = 1;R1(1,2) = 0;R1(1,3) = 0;
    R1(2,1) = 0;R1(2,2) = 1;R1(2,3) = 0;
    R1(3,1) = 0;R1(3,2) = 0;R1(3,3) = 1;

elseif k==2
    R1(1,1) = 0;R1(1,2) = 1;R1(1,3) = 0;
    R1(2,1) = -1;R1(2,2) = 0;R1(2,3) = 0;
    R1(3,1) = 0;R1(3,2) = 0;R1(3,3) = 1;
elseif k==3
    R1(1,1) = -1;R1(1,2) = 0;R1(1,3) = 0;
    R1(2,1) = 0;R1(2,2) = -1;R1(2,3) = 0;
    R1(3,1) = 0;R1(3,2) = 0;R1(3,3) = 1;
elseif k==4
    R1(1,1) = 0;R1(1,2) = -1;R1(1,3) = 0;
    R1(2,1) = 1;R1(2,2) = 0;R1(2,3) = 0;
    R1(3,1) = 0;R1(3,2) = 0;R1(3,3) = 1;
elseif k==5
    R1(1,1) = 1;R1(1,2) = 0;R1(1,3) = 0;
    R1(2,1) = 0;R1(2,2) = -1;R1(2,3) = 0;
    R1(3,1) = 0;R1(3,2) = 0;R1(3,3) = -1;

elseif k==6
    R1(1,1) = 0;R1(1,2) = 1;R1(1,3) = 0;
    R1(2,1) = 1;R1(2,2) = 0;R1(2,3) = 0;
    R1(3,1) = 0;R1(3,2) = 0;R1(3,3) = -1;
elseif k==7
    R1(1,1) = -1;R1(1,2) = 0;R1(1,3) = 0;
    R1(2,1) = 0;R1(2,2) = 1;R1(2,3) = 0;
    R1(3,1) = 0;R1(3,2) = 0;R1(3,3) = -1;

elseif k==8
    R1(1,1) = 0;R1(1,2) = -1;R1(1,3) = 0;
    R1(2,1) = -1;R1(2,2) = 0;R1(2,3) = 0;
    R1(3,1) = 0;R1(3,2) = 0;R1(3,3) = -1;

end

RT = R1 * R;
TG = G * RT;
TH = H * RT;

for ic=1:2      % Specifies the particular EPR transition.

if ic==1
    HH = InitialHH;
    EE = AgEnergyLevels_P(TG,TH,HH,P,B,gbn);
    FREQ = EE(4)-EE(1);
    while abs(FREQQ-FREQ)>1;
        HH = HH * (FREQQ/FREQ);
        EE = AgEnergyLevels_P(TG,TH,HH,P,B,gbn);
        FREQ = EE(4)-EE(1);
    end
    MagneticField(n,k) = HH;

```

```

elseif ic==2
    HH = InitialHH;
    EE = AgEnergyLevels_P(TG,TH,HH,P,B,gbn);
    FREQ = EE(3)-EE(2);
    while abs(FREQQ-FREQ)>1;
        HH = HH * (FREQQ/FREQ);
        EE = AgEnergyLevels_P(TG,TH,HH,P,B,gbn);
        FREQ = EE(3)-EE(2);
    end
    MagneticField(n,k+8) = HH;

end
end
end
end

for Plane=2      % Rotation from c to a.

for n=1:91      % Rotation increment is one degree.
    Alpha = (n-1)*CTR;
    Beta = 0*CTR;
    N(n) = n-1;

    R(1,1) = cos(Alpha)*cos(Beta);
    R(1,2) = -sin(Beta);
    R(1,3) = sin(Alpha)*cos(Beta);
    R(2,1) = cos(Alpha)*sin(Beta);
    R(2,2) = cos(Beta);
    R(2,3) = sin(Alpha)*sin(Beta);
    R(3,1) = -sin(Alpha);
    R(3,2) = 0;
    R(3,3) = cos(Alpha);

    for k=1:8

        if k==1
            R1(1,1) = 1;R1(1,2) = 0;R1(1,3) = 0;
            R1(2,1) = 0;R1(2,2) = 1;R1(2,3) = 0;
            R1(3,1) = 0;R1(3,2) = 0;R1(3,3) = 1;
        elseif k==2
            R1(1,1) = 0;R1(1,2) = 1;R1(1,3) = 0;
            R1(2,1) = -1;R1(2,2) = 0;R1(2,3) = 0;
            R1(3,1) = 0;R1(3,2) = 0;R1(3,3) = 1;
        elseif k==3
            R1(1,1) = -1;R1(1,2) = 0;R1(1,3) = 0;
            R1(2,1) = 0;R1(2,2) = -1;R1(2,3) = 0;
            R1(3,1) = 0;R1(3,2) = 0;R1(3,3) = 1;
        elseif k==4
            R1(1,1) = 0;R1(1,2) = -1;R1(1,3) = 0;
            R1(2,1) = 1;R1(2,2) = 0;R1(2,3) = 0;
            R1(3,1) = 0;R1(3,2) = 0;R1(3,3) = 1;
        elseif k==5
            R1(1,1) = 1;R1(1,2) = 0;R1(1,3) = 0;
            R1(2,1) = 0;R1(2,2) = -1;R1(2,3) = 0;
            R1(3,1) = 0;R1(3,2) = 0;R1(3,3) = -1;
        elseif k==6
            R1(1,1) = 0;R1(1,2) = 1;R1(1,3) = 0;
            R1(2,1) = 1;R1(2,2) = 0;R1(2,3) = 0;
            R1(3,1) = 0;R1(3,2) = 0;R1(3,3) = -1;
        elseif k==7
            R1(1,1) = -1;R1(1,2) = 0;R1(1,3) = 0;
            R1(2,1) = 0;R1(2,2) = 1;R1(2,3) = 0;
            R1(3,1) = 0;R1(3,2) = 0;R1(3,3) = -1;
        elseif k==8
            R1(1,1) = 0;R1(1,2) = -1;R1(1,3) = 0;
            R1(2,1) = -1;R1(2,2) = 0;R1(2,3) = 0;
            R1(3,1) = 0;R1(3,2) = 0;R1(3,3) = -1;
        end
    end
end
end
end

```

```

end

RT = R1 * R;
TG = G * RT;
TH = H * RT;

for ic=1:2      % Specifies the particular EPR transition.

    if ic==1
        HH = InitialHH;
        EE = AgEnergyLevels_P(TG,TH,HH,P,B,gbn);
        FREQ = EE(4)-EE(1);
        while abs(FREQQ-FREQ)>1;
            HH = HH * (FREQQ/FREQ);
            EE = AgEnergyLevels_P(TG,TH,HH,P,B,gbn);
            FREQ = EE(4)-EE(1);
        end
        MagneticField2(n,k) = HH;

    elseif ic==2
        HH = InitialHH;
        EE = AgEnergyLevels_P(TG,TH,HH,P,B,gbn);
        FREQ = EE(3)-EE(2);
        while abs(FREQQ-FREQ)>1;
            HH = HH * (FREQQ/FREQ);
            EE = AgEnergyLevels_P(TG,TH,HH,P,B,gbn);
            FREQ = EE(3)-EE(2);
        end
        MagneticField2(n,k+8) = HH;

    end
end
end
end
end

for Plane=1

h(1)=3042.965;Beta(1)=0;
h(2)=3058.819;Beta(2)=0;
h(3)=3294.133;Beta(3)=0;
h(4)=3304.680;Beta(4)=0;

h(5)=3042.308;Beta(5)=15;
h(6)=3261.255;Beta(6)=15;
h(7)=3272.969;Beta(7)=15;
h(8)=3288.831;Beta(8)=15;
h(9)=3299.390;Beta(9)=15;

h(10)=3110.997;Beta(10)=25;
h(11)=3224.281;Beta(11)=25;
h(12)=3237.190;Beta(12)=25;
h(13)=3266.529;Beta(13)=25;
h(14)=3277.682;Beta(14)=25;

h(15)=3091.055;Beta(15)=35;
h(16)=3105.149;Beta(16)=35;
h(17)=3136.245;Beta(17)=35;
h(18)=3150.346;Beta(18)=35;
h(19)=3193.166;Beta(19)=35;
h(20)=3231.323;Beta(20)=35;
h(21)=3243.043;Beta(21)=35;

h(22)=3132.114;Beta(22)=45;
h(23)=3146.786;Beta(23)=45;
h(24)=3185.534;Beta(24)=45;
h(25)=3197.270;Beta(25)=45;

```

```

h(26)=3042.965;Beta(26)=90;
h(27)=3058.819;Beta(27)=90;
h(28)=3294.133;Beta(28)=90;
h(29)=3304.680;Beta(29)=90;

h(30)=3042.308;Beta(30)=75;
h(31)=3261.255;Beta(31)=75;
h(32)=3272.969;Beta(32)=75;
h(33)=3288.831;Beta(33)=75;
h(34)=3299.390;Beta(34)=75;

h(35)=3110.997;Beta(35)=65;
h(36)=3224.281;Beta(36)=65;
h(37)=3237.190;Beta(37)=65;
h(38)=3266.529;Beta(38)=65;
h(39)=3277.682;Beta(39)=65;

h(40)=3091.055;Beta(40)=55;
h(41)=3105.149;Beta(41)=55;
h(42)=3136.245;Beta(42)=55;
h(43)=3150.346;Beta(43)=55;
h(44)=3193.166;Beta(44)=55;
h(45)=3231.323;Beta(45)=55;
h(46)=3243.043;Beta(46)=55;

plot(N+90,MagneticField,'-',Beta+90,h,'o','color','b')
ylabel('Magnetic Field (gauss)')
xlabel('Angle (degrees)')
end

for Plane=2

h(1)=2931.543;Alpha(1)=0;
h(2)=2951.301;Alpha(2)=0;

h(3)=2889.426;Alpha(3)=10;
h(4)=2911.328;Alpha(4)=10;
h(5)=2931.281;Alpha(5)=10;
h(6)=2981.737;Alpha(6)=10;

h(7)=2858.818;Alpha(7)=20;
h(8)=2945.435;Alpha(8)=20;
h(9)=3008.362;Alpha(9)=20;
h(10)=3057.329;Alpha(10)=20;

h(11)=3094.174;Alpha(11)=30;
h(12)=3110.016;Alpha(12)=30;

h(13)=3047.808;Alpha(13)=40;
h(14)=3120.576;Alpha(14)=40;
h(15)=3134.660;Alpha(15)=40;
h(16)=3149.529;Alpha(16)=40;

h(17)=3056.118;Alpha(17)=45;
h(18)=3073.326;Alpha(18)=45;
h(19)=3135.903;Alpha(19)=45;
h(20)=3150.763;Alpha(20)=45;
h(21)=3150.763;Alpha(21)=45;
h(22)=3163.281;Alpha(22)=45;

h(23)=3089.195;Alpha(23)=50;
h(24)=3105.625;Alpha(24)=50;
h(25)=3159.608;Alpha(25)=50;
h(26)=3172.122;Alpha(26)=50;
h(27)=3172.122;Alpha(27)=50;
h(28)=3186.214;Alpha(28)=50;

h(29)=3172.171;Alpha(29)=60;
h(30)=3231.667;Alpha(30)=60;
h(31)=3244.939;Alpha(31)=60;

```

```

h(32)=2932.574;Alpha(32)=70;
h(33)=2952.130;Alpha(33)=70;
h(34)=3139.145;Alpha(34)=70;
h(35)=3215.042;Alpha(35)=70;
h(36)=3276.065;Alpha(36)=70;
h(37)=3287.795;Alpha(37)=70;

```

```

h(38)=2988.303;Alpha(38)=80;
h(39)=3005.893;Alpha(39)=80;
h(40)=3093.348;Alpha(40)=80;
h(41)=3108.603;Alpha(41)=80;
h(42)=3267.043;Alpha(42)=80;
h(43)=3279.369;Alpha(43)=80;
h(44)=3298.719;Alpha(44)=80;
h(45)=3309.865;Alpha(45)=80;

```

```

h(46)=3042.965;Alpha(46)=90;
h(47)=3058.819;Alpha(47)=90;
h(48)=3294.133;Alpha(48)=90;
h(49)=3304.680;Alpha(49)=90;

```

```

X(1)=30;
Y(1)=2841;
X(2)=30;
Y(2)=2867;
X(3)=40;
Y(3)=2838;
X(4)=40;
Y(4)=2863;
X(5)=45;
Y(5)=2841;
X(6)=45;
Y(6)=2867;
X(7)=50;
Y(7)=2856;
X(8)=50;
Y(8)=2882;
X(9)=60;
Y(9)=2903;
X(10)=60;
Y(10)=2924;

```

```

hold on
plot(N,MagneticField2,'-',Alpha,h,'o','color','b')
hold on
plot(X,Y,'rs','MarkerSize',5,'color','k')
ylabel('Magnetic Field (gauss)')
xlabel('Angle (degrees)')
end
end

```

## Bibliography

- [1] B. D. Milbrath, A. J. Peurrung, M. Bliss, and W. J. Weber, "Radiation Detector Materials: An Overview", *J. Mater. Res.* **23**, 2561 (2008).
- [2] G. Knoll, "Fast Neutron Detection and Spectroscopy", *Radiation Detection and Measurement*, (John Wiley & Sons, Inc., 2000).
- [3] "Table of Nuclides: neutron cross sections of selected elements"  
<http://atom.kaeri.re.kr>, (2009).
- [4] Ya. V. Burak, V. T. Adamiv, I. M. Teslyuk, and V. M. Shevel, "Optical absorption of isotropically enriched  $\text{Li}_2\text{B}_4\text{O}_7$  single crystals irradiated by thermal neutrons", *Radiation Measurements* **38**, 681-684 (2004).
- [5] J. P. Chaminade, O. Viraphong, F. Guillen, C. Fouassier, and B. Czirr, "Crystal growth and optical properties of new neutron detectors  $\text{Ce}^{3+}:\text{}^6\text{LiR}(\text{Bo}_3)_3$  (R=Gd, Y)", *IEEE Trans. Nucl. Sci.* **48**, 1158 (2001).
- [6] Sangeeta, K. Chennakesavulu, D. G. Desai, S. C. Sabharwal, M. Alex, M. D. Ghodgaonkar, "Neutron flux measurements with a  $\text{Li}_2\text{B}_4\text{O}_7$  crystal", *Nuclear Instruments and Methods in Physics Research Section A: Accelerators, Spectrometers, Detectors and Associated Equipment*, **571**, 699-703 (2007).
- [7] Y. V. Burak, B. V. Padlyak, V. M. Shevel, "Radiation-induced centers in the  $\text{Li}_2\text{B}_4\text{O}_7$  single crystals", *Nuclear Instruments and Methods in Physics Research Section B: Beam Interactions with Materials and Atoms*, **191**, 633-637 (2002).
- [8] A. Gurga, T. Juliano, Y. Gogotsi, S. N. Dub, N. V. Stus, D. A. Stratiichuk, V. V. Lisnyak, "The mechanical properties of lithium tetraborate (100), (011), and (112) faces", *Materials Letters*, **61**, 770-773 (2007).
- [9] K. Uchida, K. Noda, T. Tanifuji, S. Nasu, V. Kiriara, and A. Kikuchi, "Optical absorption spectra of neutron-irradiated  $\text{Li}_2\text{O}$ ", *Physica Status Solidi (a)* **58**, 557-566 (1980).
- [10] Y. V. Burak, B. V. Padlyak, and V. M. Shevel, "Neutron-Induced Defects in the Lithium Tetraborate Single Crystals," *Radiation Effects & Defects in Solids* **157**, 1101-1109 (2002).



- [11] A. Ballato, J. Kosinski, and T. Lukaszek, "Lithium Tetraborate Transducers", *Trans on Ultrasonics, Ferroelectrics and Frequency Control, IEEE*, **38**, 62-66, (1991).
- [12] J. Krogh-Moe, *Acta Crystallogr.* **15**, 190 (1962).
- [13] J. Krogh-Moe, *Acta Crystallogr., Sect. B: Struct. Crystallogr. Cryst. Chem.*, **24**, 179 (1968).
- [14] S. F. Radaev, L. A. Muradyan, L. F. Malakhova, Y. V. Burak, and V. I. Simonov, *Kristallografiya* **34**, 1400 (1989).
- [15] N. Sennova, R. S. Bubnova, G. Cordier, B. Albert, S. K. Filatov, and L. Z. Isaenko, *Anorg. Allg. Chem.* **634**, 2601 (2008).
- [16] V. T. Adamiv, Y. V. Burak, I. M. Teslyuk, *J. Alloys Compd.* **475**, 869 (2009).
- [17] J. M. Spaeth, H. Overhof, "*Point Defects in Semiconductors and Insulators: Determination of Atomic and Electronic Structure from Paramagnetic Hyperfine Interactions*," (Springer, 2003).
- [18] M. M. Chirila, N. Y. Garces, L. E. Halliburton, D. R. Evans, R. K. Route, and M. M. Fejer, "Thermally stimulated luminescence from vapor-transport-equilibrated LiTaO<sub>3</sub> crystals," *Journal of Applied Physics* , **94**, 301-306 (2003).
- [19] C. Cohen-Tannoudji, B. Diu, and F. Laloe, "Quantum Mechanics" (Wiley, 2006).
- [20] B. Odom, D. Hanneke, B. d'Urso, and G. Gabrielse, "New measurement of the electron magnetic moment using a one-electron quantum cyclotron," *Physical Review Letters*, **97** (3): 030801 (2006).
- [21] [http://en.wikipedia.org/wiki/Electron\\_paramagnetic\\_resonance](http://en.wikipedia.org/wiki/Electron_paramagnetic_resonance) (2012).
- [22] S. M. Evans, "Identification and Characterization of Point Defects in Aluminum Nitride and Zinc Oxide Crystals", *West Virginia Dissertation*, pp 27-28 (2008).
- [23] "*EMX Series User's Manual*", Bruker BioSpin Corp. (2009).
- [24] C. P. Schlichter, "*Principles of Magnetic Resonance*", (Springer-Verlag, Berlin, 1978).

- [25] J. A. Weil, J. R. Bolton, and J. E. Wertz, “*Electron Paramagnetic Resonance*,” (John Wiley & Sons Inc., 1994).
- [26] B. Henderson, and G. F. Imbusch, “Optical Spectroscopy of Inorganic Solids,” p 199 (Oxford Science Publications, 1989).
- [27] D. M. Hofmann, A. Hofstaetter, F. Leiter, and B. Meyer, “Hydrogen: A Relevant Shallow Donor in Zinc Oxide”, *Physical Review Letters*, **88** (4), (2002).
- [28] L. S. Vlasenko, G. D. Watkins, “Optical detection of electron paramagnetic resonance in room-temperature electron-irradiated ZnO,” *Physical Review B*, **71** (2005).
- [29] K. L. Sweeney, L. E. Halliburton, D. A. Bryan, R. R. Rice, R. Gerson, and H. E. Tomaschke, “Point defects in Mg-doped lithium niobate,” *Journal of Applied Physics*, **57** (4), 1036-1044 (1985).
- [30] I.N. Ogorodnikov, L.I. Isaenko, A.V. Kruzhalov, A.V. Porotnikov, “Thermally stimulated luminescence and lattice defects in crystals of alkali metal borate LiB<sub>3</sub>O<sub>5</sub> (LBO),” *Radiation Measurements*, **33** (5), 577-581 (2001).
- [31] Swinney, M.W., McClory, J.W., Petrosky, J.C., Yang, S., Brant, A.T., *et al.*, “Identification of electron and hole traps in lithium tetraborate (Li<sub>2</sub>B<sub>4</sub>O<sub>7</sub>) crystals: oxygen vacancies and lithium vacancies,” *J. Appl. Phys.*, **107** (11), 113715 (2010).
- [32] Y. Kutomi, N. Takeuchi, “Thermoluminescence in lithium tetraborate doped with activators,” *Journal of Materials Science Letters*, **5**, p51-53 (1986).
- [33] A.C. Fernandes, M. Osvay, J.P. Santos, V. Holovey, M. Ignatovych, “TL properties of newly developed lithium tetraborate single crystals,” *Radiation Measurements*, **43**, 476-479 (2008).
- [34] M. Ishii, Y. Kuwano, S. Asaba, T. Asai, M. Kawamura, N. Senguttuvan, T. Hayashi, M. Koboyashi, M. Nikl, S. Hosoya, K. Sakai, T. Adachi, T. Oku, H.M. Shimizu, “Luminescence of doped lithium tetraborate single crystals and glass,” *Radiation Measurements*, **38**, 571-574 (2004).
- [35] Y. Chen and M. M. Abraham, *J. Phys. Chem. Solids*, **51**, 747 (1990).

- [36] O. F. Schirmer, *J. Phys. Chem. Solids*, **29**, 1407 (1968).
- [37] R. H. D. Nuttall and J. A. Weil, *Can. J. Phys.*, **59**, 1696 (1981).
- [38] C. J. Walsby, N. S. Lees, W. C. Tennant, and R. F. C. Claridge, *J. Phys.: Condens. Matter*, **12**, 1441 (2000).
- [39] W. Hong, “EPR and ENDOR Studies of Point Defects in  $\text{LiB}_3\text{O}_5$  and  $\beta\text{-BaB}_2\text{O}_4$ ,” *West Virginia University Dissertation*, (2003).
- [40] W. Hong, M. M. Chirila, N. Y. Garces, and L. E. Halliburton, “Electron paramagnetic resonance and electron-nuclear double resonance study of trapped-hole centers in  $\text{LiB}_3\text{O}_5$  crystals,” *Phys. Rev. B*, **68** (9), 094111 (2003).
- [41] J.L. Ketchum, K.L. Sweeney, L.E. Halliburton, and A.F. Armington, “Vacuum annealing effects in lithium niobate,” *Physics Letters A*, **94** (9), 450-453 (1983).
- [42] A. S. Bhalla, L. E. Cross, and R. W. Whatmore, *Jpn. J. Appl. Phys.*, Suppl. 2, **24**, 727 (1985).
- [43] I. Ketsman, D. Wooten, J. Xiao, Y. B. Losovyj, Y. V. Burak, V. T. adamiv, A. Sokolov, J. Petrosky, J. McClory, and P. A. Dowben, *Phys. Lett. A*, **374**, 891 (2010).
- [44] T. Shiosaki, M. Adachi, H. Kobayashi, K. Araki, and A. Kawabata, *Jpn. J. Appl. Phys.*, Suppl. 1 **24**, 25 (1985).
- [45] A. Ballato, J. Kosinski, and T. Lukaszek, *IEEE Trans. Ultrason. Ferro-electr. Freq. Control*, **38**, 62 (1991).
- [46] M. Maeda, H. Tachi, K. Honda, and I. Suzuki, *Jpn. J. Appl. Phys.*, Part. 1 **33**, 1965 (1994).
- [47] Z. Xiong, Q. Tang, X. Xiong, D. Luo, and P. Ding, “The roles of Ag, in and P in the thermoluminescence emission of  $\text{Li}_2\text{B}_4\text{O}_7$  phosphors,” *Radiat. Meas.*, **46**, 323 (2011).
- [48] B. T. Huy, V. X. Quang, and H. T. B. Chau, *J. Lumin.*, **128**, 1601 (2008).
- [49] A. (Türkler) Ege, E. Ekdal, T. Karali, and N. Can, *Radiat. Meas.*, **42**, 1280 (2007).

- [50] V. T. Adamiv, O. T. Antonyak, Ya. V. Burak, M. S. Pidzyrailo, and I. M. Teslyuk, “Model of TSL—centers in  $\text{Li}_2\text{B}_4\text{O}_7$ : A (A= Cu, Ag) single crystals”, *Funct. Mater.*, **12**, 278 (2005).
- [51] A. T. Brant, B. E. Kananan, M. K. Murari, J. W. McClory, J. C. Petrosky, V. T. Adamiv, Ya. V. Burak, P. A. Dowben, and L. E. Halliburton, “Electron and hole traps in Ag-doped lithium tetraborate crystals”, *J. Appl. Phys.*, **110**, 093719 (2011).
- [52] M. Martini, F. Meinardi, L. Kovacs, and K. Polgar, “Spectrally Resolved Thermoluminescence of  $\text{Li}_2\text{B}_4\text{O}_7$ :Cu Single Crystals”, *Radiat. Prot. Dosim.*, **65**, 343 (1996).
- [53] M. Prokic, “Dosimetric Characteristics of  $\text{Li}_2\text{B}_4\text{O}_7$ :Cu,Ag,P Solid TL Detectors,” *Radiat. Prot. Dosim.* **100**, 265 (2002).
- [54] N. Can, T. Karali, P. D. Townsend, and F. Yildiz, “TL and EPR studies of Cu, Ag and P doped  $\text{Li}_2\text{B}_4\text{O}_7$  phosphor,” *J. Phys. D*, **39**, 2038 (2006).
- [55] M. Ignatovych, V. Holovey, T. Vidoczy, P. Baranyai, A. Kelemen, V. Laguta, and O. Chuiko, “Spectroscopy of Cu- and Ag- doped single crystal and glassy lithium tetraborate: luminescence, optical absorption and ESR study,” *Funct. Mater.*, **12** (2), 313 (2005).
- [56] F. P. Doty, I. Zwieback, W. Ruderman, “Solid State Neutron Detector and Method for Use,” *United States Patent*, US 6,388,260 B1 (2002).
- [57] W. L. Li, X. M. Li, W. L. Feng, W. J. Yang, and C. Y. Tao, “Theoretical investigation for the EPR  $g$ -factors of the mixed ground state in  $\text{NaCl}:\text{Ag}^{2+}$  crystals,” *Spectrochim. Acta A* **79**, 1308 (2011).
- [58] W. Hong, D. Perlov, and L. E. Halliburton, “Electron paramagnetic resonance study of  $\text{Ag}^0$  atoms and  $\text{Ag}^{2+}$  ions in  $\beta\text{-BaB}_2\text{O}_4$  nonlinear optical crystals,” *J. Phys. D: Appl. Phys.* **36**, 2605 (2003).
- [59] K. Chandrasekharan and V. S. Murty, “ESR study of  $\text{Ag}^{2+}$  ions in  $\text{KNO}_3$ ,” *Physica B* **205**, 349 (1995).

- [60] M. Ignatovych, V. Holovey, A. Watterich, T. Vidóczy, P. Baranyai, A. Kelemen, and O. Chuiko, “Luminescence characteristics of Cu- and Eu-doped  $\text{Li}_2\text{B}_4\text{O}_7$ ,” *Radiation Measurements*, **38**, (2004).
- [61] S.M Kaczmarek, “ $\text{Li}_2\text{B}_4\text{O}_7$  glasses doped with Cr, Co, Eu and Dy,” *Optical Materials*, **19** (1), 189-194 (2002).
- [62] Y. Kutomi, A. Tomita, and N. Takeuchi, “TL and TSEE in Crystallised  $\text{Li}_2\text{B}_4\text{O}_7\text{:Cu}$  Glass,” *Radiat Prot Dosimetry*, **17** (1-4), 499-502 (1986).
- [63] G. D. Patra, M. Tyagi, D. G. Desai, B. Tiwari, S. Sen, and S. C. Gahdkari, “Photo-luminescence properties of Cu and Ag doped  $\text{Li}_2\text{B}_4\text{O}_7$  single crystals at low temperatures,” *J. Luminescence* **132**, 1101 (2012).
- [64] M. Ignatovych, V. Holovey, T. Vidoczy, P. Baranyai, and A. Keleman, “Spectral study on manganese- and silver-doped lithium tetraborate phosphors,” *Rad. Phys. Chem.* **76**, 1527 (2007).
- [65] N. Senguttuvan, M. Ishii, M. Shimoyama, M. Kobayashi, N. Tsutsui, M. Nikl, M. Dusek, H. M. Shimizu, T. Oku, T. Adachi, K. Sakai, and J. Suzuki, *Nuc. Inst. Meth. Phys. Res. A* **486**, 264 (2002).
- [66] Kang-Soo Park, J.K. Ahn, D.J. Kim, H.K. Kim, Y.H. Hwang, D.S. Kim, M.H. Park, Yumi Park, Jin-Joo Yoon, Jae-Young Leem, “Growth and properties of  $\text{Li}_2\text{B}_4\text{O}_7$  single crystals doped with Cu, Mn and Mg,” *Journal of Crystal Growth*, **249**, 483-486 (2003).
- [67] V. M. Holovey, K. P. Popovich, D. B. Goyer, V. M. Krasyllynets, A. V. Gomonnai, “Spectral dependences of thermally stimulated luminescence and X-ray luminescence of single-crystalline and glassy  $\text{Li}_2\text{B}_4\text{O}_7\text{:Mn}$ ,” *Radiation Effects and Defects in Solids*, **166**, (2011).
- [68] V.M. Holovey, V.I. Sidey, V.I. Lyamayev, P.P. Puga, “Influence of reducing annealing on the luminescent properties of  $\text{Li}_2\text{B}_4\text{O}_7\text{:Cu}$  single crystals,” *Journal of Luminescence*, **126** (2), 408-412 (2007).
- [69] Babita Tiwari, N.S. Rawat, D.G. Desai, S.G. Singh, M. Tyagi, P. Ratna, S.C. Gadhari, M.S. Kulkarni, “Thermoluminescence studies on Cu-doped  $\text{Li}_2\text{B}_4\text{O}_7$  single crystals,” *J. Luminescence*, **130** (11), 2076-2083 (2010).

- [70] G. D. Patra, A. K. Singh, S. G. Singh, M. Tyagi, S. Sen, B. Tiwari, and S. C. Gadkari, "Comparison of optical properties of pure and doped lithium tetraborate single crystals and glasses," *AIP Conf. Proc.* **1447**, 1335 (2012).
- [71] C. Corradi, V. Nagirnyi, A. Kotlov, A. Watterich, M. Kirm, K. Polgar, A. Hofstaetter, and M. Meyer, "Investigation of Cu-doped  $\text{Li}_2\text{B}_4\text{O}_7$  single crystals by electron paramagnetic resonance and time-resolved optical spectroscopy," *J. Phys.: Condens. Matter*, **20**, 025216 (2008).
- [72] M. Takenaga, O. Yamamoto, and T. Yamashita, "Preparation and characteristics of  $\text{Li}_2\text{B}_4\text{O}_7$  : Cu phosphor," *Nuclear Instruments and Methods*, **175**, 77-78 (1980).
- [73] J A Weil, "The analysis of large hyperfine splitting in paramagnetic resonance spectroscopy," *Journal of Mag. Res.*, **4**, 394-399 (1971).
- [74] J.R Morton, K.F Preston, "Atomic parameters for paramagnetic resonance data," *Journal of Mag. Res.*, **30**, 577-582 (1969).
- [75] James A. J. Fitzpatrick, Frederick R. Manby, and Colin M. Western, "The interpretation of molecular magnetic hyperfine interactions," *J. Chem. Phys.*, **122**, 084312 (2005).
- [76] E. J. West, A. E. Nash, F. H. Attix, R. D. Kirk, and J. H. Schulman, *Report of NRL Progress*, (1967).
- [77] S. W. S. McKeever, "Thermoluminescence of Solids," (Cambridge University Press, 1985).
- [78] V. M. Holovey, V. I. Lyamayev, M. M. Birov, P. P. Puga, and A. M. Soloman, "Dopant concentration dependence of thermostimulated luminescence in :Mn single crystals," *Functional Materials*, **12** (2), 318 (2005).
- [79] N.S. Rawat, M.S. Kulkarni, M. Tyagi, P. Ratna, D.R. Mishra, S.G. Singh, B. Tiwari, A. Soni, S.C. Gadkari, S.K. Gupta, "TL and OSL studies on lithium borate single crystals doped with Cu and Ag," *Journal of Luminescence*, **132** (8) 1969-1975 (2012).
- [80] A. Kelemen, M. Ignatovych, V. Holovey, T Vidoczy, and P. Baranyai, "Effect of irradiation on photoluminescence and optical absorption spectra of  $\text{Li}_2\text{B}_4\text{O}_7$ :Mn and  $\text{Li}_2\text{B}_4\text{O}_7$ :Ag single crystals," *Radiation Physics and Chemistry*, **76** (8), 1531-1534 (2007).

- [81] V.T. Adamiv, Ya.V. Burak, I.V. Kityk, J. Kasperczyk, R. Smok, M. Czerwiński, Nonlinear optical properties of  $\text{Li}_2\text{B}_4\text{O}_7$  single crystals doped with potassium and silver, *Optical Materials*, **8**(3), 207-213 (1997)
- [82] B. G. Ershov, E. Janata, A. Henglein, and A. Fojtik, "Silver Atoms and Clusters in Aqueous Solution: Absorption Spectra and the Particle Growth in the Absence of Stabilizing  $\text{Ag}^+$  Ions," *J. Phys. Chem.*, **97**, 4589-4594 (1993)
- [83] E. Janata, A. Henglein, and B. G. Ershov, "First Clusters of  $\text{Ag}^+$  Ion Reduction in Aqueous Solution," *J. Phys. Chem.*, **98**, 10888 (1994)
- [84] G. Blasse and B. Grabmaier, "Luminescent Materials," (*Springer-Verlag Publishing*, 1994)

<b>REPORT DOCUMENTATION PAGE</b>			Form Approved OMB No. 0704-0188		
The public reporting burden for this collection of information is estimated to average 1 hour per response, including the time for reviewing instructions, searching existing data sources, gathering and maintaining the data needed, and completing and reviewing the collection of information. Send comments regarding this burden estimate or any other aspect of this collection of information, including suggestions for reducing this burden to Department of Defense, Washington Headquarters Services, Directorate for Information Operations and Reports (0704-0188), 1215 Jefferson Davis Highway, Suite 1204, Arlington, VA 22202-4302. Respondents should be aware that notwithstanding any other provision of law, no person shall be subject to any penalty for failing to comply with a collection of information if it does not display a currently valid OMB control number. PLEASE DO NOT RETURN YOUR FORM TO THE ABOVE ADDRESS.					
1. REPORT DATE (DD-MM-YYYY) 14-12-2012		2. REPORT TYPE PhD Dissertation		3. DATES COVERED (From — To) 17-08-2009 to 14-12-2012	
4. TITLE AND SUBTITLE EPR and ENDOR Studies of Point Defects in Lithium Tetraborate Crystals			5a. CONTRACT NUMBER		
			5b. GRANT NUMBER		
			5c. PROGRAM ELEMENT NUMBER		
6. AUTHOR(S) Douglas A. Buchanan			5d. PROJECT NUMBER		
			5e. TASK NUMBER		
			5f. WORK UNIT NUMBER		
7. PERFORMING ORGANIZATION NAME(S) AND ADDRESS(ES) Air Force Institute of Technology Graduate School of Engineering and Management (AFIT/ENY) 2950 Hobson Way WPAFB OH 45433-7765			8. PERFORMING ORGANIZATION REPORT NUMBER  AFIT-ENP-DS-12-D-01		
9. SPONSORING / MONITORING AGENCY NAME(S) AND ADDRESS(ES) Col Rex R. Kiziah HQ USAFA/DFP 2354 Fairchild Dr, Suite 2A31 USAF Academy, CO 80840-6254			10. SPONSOR/MONITOR'S ACRONYM(S) US Air Force Academy		
			11. SPONSOR/MONITOR'S REPORT NUMBER(S)		
12. DISTRIBUTION / AVAILABILITY STATEMENT APPROVED FOR PUBLIC RELEASE; DISTRIBUTION UNLIMITED					
13. SUPPLEMENTARY NOTES This material is declared a work of the U.S. Government and is not subject to copyright protection in the United States.					
14. ABSTRACT Lithium tetraborate ( $\text{Li}_2\text{B}_4\text{O}_7$ or LTB) is a promising material for both radiation dosimetry and neutron detection applications. LTB crystals can be grown pure or doped with different impurities including transition-metal and rare-earth ions. Research in this dissertation focuses on undoped LTB crystals and LTB crystals doped with copper and silver. Electron paramagnetic resonance (EPR) and electron-nuclear double resonance (ENDOR) are used to characterize point defects in the lithium tetraborate crystals. Thermoluminescence (TL), photoluminescence (PL), photoluminescence excitation (PLE), and optical absorption (OA) are also used. An intrinsic hole trap associated with lithium vacancies is characterized with EPR and ENDOR and its thermal stability is determined using thermoluminescence. A "perturbed" hole trap due to $\text{Ag}^{2+}$ ions is characterized in doped crystals using EPR data alone. This method is tested on a previously studied hole center where both EPR and ENDOR were used. New x-ray induced centers are identified in copper-doped crystals. These include two $\text{Cu}^{2+}$ hole centers and two $\text{Cu}^0$ electron centers. These centers are characterized with EPR and their thermal stability explains TL peaks in glow curves. Finally, a comprehensive study utilizing EPR, OA, PL, and PLE data provide convincing explanations for the absorption and emission features of silver-doped crystals.					
15. SUBJECT TERMS EPR, ENDOR, optical characterization, lithium tetraborate, point defects					
16. SECURITY CLASSIFICATION OF:			17. LIMITATION OF ABSTRACT  UU	18. NUMBER OF PAGES  160	19a. NAME OF RESPONSIBLE PERSON Dr. John W. McClory
a. REPORT  U	b. ABSTRACT  U	c. THIS PAGE  U			19b. TELEPHONE NUMBER (Include Area Code) (937)255-3636, ext 7308

Standard Form 298 (Rev. 8-98)  
Prescribed by ANSI Std. Z39.18